HIGH RESOLUTION CMR T1 MAPPING FOR IMAGING RIGHT VENTRICULAR MYOCARDIAL FIBROSIS

A Dissertation

Presented to the Faculty of

The School of Engineering and Applied Science

University of Virginia

In Partial Fulfillment

Of the Requirements for the Degree of

Doctor of Philosophy in Biomedical Engineering

BHAIRAV BIPIN MEHTA

MAY, 2015

APPROVAL SHEET

The dissertation

Is submitted in partial fulfillment of the requirements

For the degree of

Doctor of Philosophy

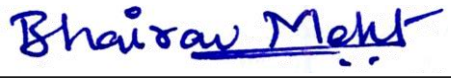

Author

The dissertation has been read and approved by the examining committee:

Frederick H. Epstein, Ph.D.

Advisor

Michael Salerno, M.D., Ph.D.

Kenneth C. Bilchick, M.D.

Craig H. Meyer, Ph.D.

Jeffrey W. Holmes, M.D., Ph.D.

Accepted for the School of Engineering and Applied Science

Dean, School of Engineering and Applied Science

May 2015

Abstract

Gadolinium-enhanced T1 mapping MRI is becoming increasingly important for the diagnosis of left ventricular (LV) myocardial fibrosis. Modified Look-Locker inversion recovery (MOLLI) and shortened MOLLI (ShMOLLI) are the current widely-used T1 mapping techniques for the heart but have limited spatial resolution due to physiological motion during image acquisition. These techniques typically have in-plane spatial resolutions in the range of 2.0–2.4 mm^2, and they are well-suited for T1 mapping of thick structures such as LV wall. Because of this, the application of T1 mapping has generally been confined to the LV. However, T1 mapping might also be valuable in thinner structures such as the right ventricle (RV) and left atrial wall to assess fibrosis in disorders such as pulmonary arterial hypertension, arrhythmogenic right ventricular cardiomyopathy, congenital heart disease, and atrial fibrillation. For imaging structures with complex geometry such as the RV wall, both high in-plane resolution and high through-plane resolution are crucial. Furthermore, several applications such as the quantitative assessment of the peri-infarct region require continuous 3D coverage of the myocardial structure. Therefore, the overall goal of this dissertation is to develop and apply noninvasive high-resolution T1 mapping MRI to assess myocardial fibrosis in thin structures such as the RV wall.

For this dissertation, Specific Aim 1 is to develop a novel high spatial resolution 2D cardiac T1 mapping technique to image the thin wall of the RV. Specific Aim 2 is to assess right ventricular fibrosis in patients with pulmonary arterial hypertension using

the T1 mapping technique developed in Aim 1. Specific Aim 3 is to extend the T1 mapping method developed in Aim #1 to perform high-resolution, three-dimensional T1 mapping of the heart within a clinically acceptable scan time.

Acknowledgements

First of all, I would like to express my deepest appreciation to my advisor Prof. Frederick H. Epstein for his support and guidance in both avenues of academic and personal growth. I am grateful for his valuable direction pointers and inspiration throughout the course of this program. I could not have accomplished this work without his expert advice and contributions. I would also like to express my sincere appreciation to Dr. Michael Salerno for his strong support, invaluable insights and help in all the projects. He has practically been my co-mentor throughout my program. I am grateful to Dr. Kenneth C. Bilchick for his support and guidance in the project pertaining to second aim. It would have been impossible to finish that project without his help and expertise. I would like to thank Prof. Craig H. Meyer for being chair of my advisory committee, for teaching me various valuable aspects of MRI and signal processing, and also for helping me with sequence and image reconstruction programming. I would also like to sincerely thank Dr. Jeffrey W. Holmes for teaching me physiology from an engineer's perspective and for guiding me to become a better scientist.

I also want to appreciate Dr. Jorge A. Gonzalez for his help in the analysis of patient data pertaining to second aim. I would like to thank Claire Stump for her help in evaluation of inter-observer and intra-observer variability of ANGIE T1 estimates. I am grateful to Dr. Patrick F. Ankowiak for his help in improving my presentation and technical writing skills. I enjoyed the usual technical discussions with my colleagues Dr. Kun Qing, Dr. Xiao Chen, Dr. Nivedita K. Naresh, Dr. Li Zhao, Yang Yang, Dr. Xiaodong Zhong, Dr. Daniel C. Auger, and Dr. Xue Feng, and I would also like to express my

sincere appreciation for their help on this dissertation work. All of them have made my graduation student experience most enjoyable and unforgettable.

Finally, and most importantly, I am grateful to my wonderful family: my father Bipin Mehta, my mother Usha Mehta and my elder sister Ami Mehta. They have been my sentinels against dark forces and luminaries for the positive forces. I believe only they can mold and nurture a below par person like me into a person capable of reaching this far. I owe everything to them. Last but not the least; I would like to acknowledge my younger sister Kunjan Mehta for her pure and innocent love and affection which motivates me to work hard for the right cause.

Table of Contents

List of Figures

List of Abbreviations and Symbols

“”	Phrases in quotation marks were directly taken from the cited literature references
NMR	Nuclear magnetic resonance
MRI	Magnetic resonance imaging
CT	Computed tomography
PET	Positron emission tomography
SPECT	Single photon emission computed tomography
BOLD	Blood oxygen level dependent
$\mathbf{I}$	Nuclear spin angular momentum
$\boldsymbol{\mu}$	Magnetic dipole moment
$\mathbf{B_0}$	External static magnetic field
H	Potential energy
$\boldsymbol{\omega_L}$	Larmor frequency
$\boldsymbol{\gamma}$	Gyromagnetic ratio
$\mathbf{M}$	Net magnetization vector

RF	Radio frequency.
$\mathbf{B_1}$	Oscillating RF magnetic field
$\boldsymbol{\omega_0}$	Angular frequency of oscillation
$\boldsymbol{t}$	Time
$\propto$	Flip angle
FID	Free induction decay
G_z	Magnetic field gradient perpendicular to the imaging plane
G_x	Magnetic field gradient along frequency encoding direction
G_y	Magnetic field gradient along phase encoding direction
1D	One-dimensional
2D	Two-dimensional
3D	Three-dimensional
k-space	2D spatial frequency space
T1	Spin-lattice relaxation time constant
ECM	Extracellular matrix
ECV	Extracellular volume fraction
λ_A	Myocardial partition coefficient for an extracellular agent A

C_t	Concentration of an agent in the tissue
C_b	Concentration of an agent in the blood
C_e	Concentration of an agent in the extravascular and extracellular space
C_p	Concentration of an agent in the plasma
Hct	Blood hematocrit
V_e	Volume fraction of the extravascular and extracellular space
V_p	Volume fraction of the plasma space
Gd	Gadolinium
6MWT	6-minute walk test
ABGs	Arterial blood gases
ANA	Antinuclear antibody serology
CHD	Congenital heart disease
CPET	Cardiopulmonary exercise test
CTD	Connective tissue disease
CXR	Chest X-ray
HIV	Human immunodeficiency virus screening
Htn	Hypertension

LFT	Liver function test
PE	Pulmonary embolism
PFT	Pulmonary function test
PH	Pulmonary hypertension
RA	Rheumatoid arthritis
RAE	Right atrial enlargement
RH Cath	Right heart catheterization
RHC	Right heart catheterization
RVE	Right ventricular enlargement;
SLE	Systemic lupus erythematosus
TEE	Transesophageal echocardiography
VHD	Valvular heart disease
VQ Scan	Ventilation-perfusion scintigram.
LV	Left ventricle
MOLLI	Modified Look-Locker inversion recovery
ShMOLLI	shortened MOLLI
RV	Right ventricular

SNR	Signal to noise ratio
PAH	Pulmonary arterial hypertension
LGE	Late gadolinium enhancement
CS	Compressed sensing
k-t	k-space and time
ANGIE	Accelerated and Navigator-Gated look-locker Imaging for cardiac T1 Estimation
PSF	Point spread function
TPSF	Transform point spread function
TSPR	Transform side lobe-to-peak ratio
CRLB	Cramer Rao lower bound
TI	Inversion time
ECG	Electrocardiogram
$\mathcal{N}(0,\sigma^2)$	Gaussian distribution with zero mean and standard deviation as σ
F	Fisher information matrix
TD	Trigger delay
SSFP	Steady state free precession

k_y-t	k_y and time
PDF	Probability density function
SENSE	Sensitivity encoding
$\mathcal{F}_u$	2D Fourier transform combined with undersampling mask
$\| \ \|_*$	Nuclear norm
$\| \ \|_2$	L2 norm
MSE	Mean squared error
SSIM	Structure similarity
bpm	Beats per minute
T	Tesla
TR	Repetition time
TE	Echo time
FOV	Field of view
NS	Not significant
Accel. Rate	Acceleration rate
CMR	Cardiac magnetic resonance imaging
GFR	Glomerular filtration rate

Gd-DTPA	Gadolinium diethylenetriaminepentacetate
λ_{Gd}	Myocardial partition coefficient for Gd-DTPA
RVSP	Right ventricular systolic pressure
RA	Right atrial
LHF	Left ventricular systolic heart failure
RVEF	RV ejection fraction
RVESV	RV end-systolic volume
MI	Myocardial infarction
ARVC	Arrhythmogenic right ventricular cardiomyopathy
$\sum_{\mathrm{b}}$	Summation over all the blocks
POCS	Projection onto convex sets
PDS	Poisson-disc based sampling
RMSE	Root mean squared error

Chapter 1

Introduction

1.1 MAGNETIC RESONANCE IMAGING (MRI)

Nuclear magnetic resonance (NMR) is a well-known phenomenon whose principles have been employed for decades to determine the structure and chemical composition of a variety of molecules and systems. Magnetic resonance imaging (MRI) is a powerful imaging modality invented in the 1970s based on the principles of NMR. Clinically, it is widely used for applications including cardiovascular, neurological and musculoskeletal imaging.

Compared to other clinical imaging modalities such as X-ray, computed tomography (CT), positron emission tomography (PET) and single photon emission computed tomography (SPECT), MRI has the advantages of utilizing non-ionizing radiation, flexible imaging plane orientation, and excellent soft tissue contrast. It can provide detailed images of the anatomical structures within the body as well as functional information about those structures. To measure structure, function, and various physiological processes, MRI often employs a wide range of exogenous and endogenous contrast mechanisms. Furthermore, MRI can selectively probe or sensitize various physical or physiological properties. For example, arterial spin labeling (ASL) uses the magnetic moment of the inflowing blood as an endogenous contrast agent to

compute the tissue perfusion, while diffusion weighted imaging sensitizes the received signal to the amount of diffusion occurring within a voxel. The ability to probe various structural and functional facets of physiology by changing the timing and/or amplitude of the set of hardware events – termed a pulse sequence – makes MRI a versatile imaging modality.

Since its inception in the 1970s, the field of MRI research has expanded significantly, and new imaging techniques continue to be developed at an astonishing rate. With the emergence of personalized medicine and patient-specific management, the application of medical imaging has grown beyond the realm of simple diagnosis. In particular, the field of MRI research has generally undergone a paradigm shift towards quantitative imaging, in which a particular tissue magnetic property or biomarker is calculated.

1.1.1 Principles of MRI

An atom is made up of protons, electrons, and neutrons which all exhibit independent quantum mechanical behavior from each other. Each possesses a spin angular momentum, also known simply as “spin”. The nuclear spin angular momentum, $\mathbf{I}$, is the combined effect of the spins of the constituent nucleons. Atoms that possess an even number of protons and neutrons have no overall spin. However, atoms that have an odd number of protons and/or an odd number of neutrons possess a net nuclear spin, and they are detectable using the magnetic resonance phenomenon, which will be detailed in the following section.

The nuclear spin results in a magnetic dipole moment, $\boldsymbol{\mu}$, which can be conceptualized as a tiny bar magnet. In the absence of external magnetic field, the magnetic dipole moments of nuclei are typically randomly oriented due to thermal energy. When these nuclei are exposed to a strong external magnetic field, the random orientation disappears. Based on quantum mechanical principles, the nuclear magnetic moment of a nucleus with spin $\mathbf{I}$ can align with an externally-applied magnetic field of strength $\mathbf{B_0}$ in only $2\mathbf{I}$ +1 possible orientations, or energy states. The potential energy of these orientation states is given by

$$\mathrm{H} = -\boldsymbol{\mu} \cdot \mathbf{B_0} \qquad [1.1]$$

Due to quantum mechanical restrictions, the nuclear magnetic moments are not completely aligned with the $\mathbf{B_0}$ magnetic field, causing the nuclear magnetic moment to precess around the axis of the $\mathbf{B_0}$ field. The frequency with which the nuclear magnetic moment precesses around the $\mathbf{B_0}$ magnetic field is known as the Larmor frequency, $\boldsymbol{\omega_L}$, and is given by

$$\boldsymbol{\omega_L} = \boldsymbol{\gamma} \mathbf{B_0} \qquad [1.2]$$

where $\boldsymbol{\gamma}$ is the gyromagnetic ratio for the nucleus of interest. For example, hydrogen protons (^{1}H) have a $\boldsymbol{\gamma}$ of approximately 42.58 MHz / Tesla, corresponding to a $\boldsymbol{\omega_L}$ of 63.86 MHz at 1.5 Tesla, a common clinical $\mathbf{B_0}$field strength.

For a nucleus with spin $\mathbf{I}$ =1/2, such as ^{1}H, there are two possible orientation states: a low energy state aligned parallel to the external magnetic field (called spin up) and a higher energy state aligned antiparallel to the external magnetic field (called spin

down). Based on the energy difference between the two states and thermal energy, there are slightly more nuclei in the spin up state than the spin down state. The small mismatch between the two energy states along with the precession of the nuclear magnetic moment gives rise to a net magnetization, $\mathbf{M}$, which is a vector aligned parallel to the direction of the $\mathbf{B_0}$ magnetic field. The direction of aligment is called the longitudinal direction and is considered the z-direction in the Cartesian frame of reference often used in MRI. This net magnetization, representing the combined sum of all the nuclear magnetic moments, contributes to the MRI signal.

The strength of external magnetic field is much higher than the strength of the net magnetization of the imaging object, such that the net magnetization cannot be measured without additional manipulation. An oscillating radio frequency (RF) magnetic field $\mathbf{B_1}$, applied perpendicularly to $\mathbf{B_0}$ at the Larmor frequency, is used to perturb the net magnetization away from the longitudinal direction. The $\mathbf{B_1}$field is defined as

$$\mathbf{B_1(t) = B_1 e^{-i\omega_0 t}} \qquad [1.3]$$

where $\boldsymbol{\omega_0}$ is generally the Larmor frequency. Conventionally, the *real* term represents the component of the $\mathbf{B_1}$ field along the X-direction, and the *imaginary* term represents the component of the $\mathbf{B_1}$ field along the Y-direction. The equation of motion for the net magnetization due to the external magnetic field is given by

$$\boldsymbol{dM(t)/dt = M(t) \times \gamma B(t)} \qquad [1.4]$$

where $\boldsymbol{B(t)}$ represents the effective (vector sum) magnetic field from the $\mathbf{B_0}$ and $\mathbf{B_1}$ fields. This equation of motion neglects the effects due to relaxation of the

magnetization, which will be discussed in section 1.1.3. The application of an RF pulse at the resonant frequency ($\boldsymbol{\omega_0 = \omega_L}$) causes the net magnetization to move in two separate, simultaneous ways. First, the net magnetization rotates about the longitudinal axis at the Larmor frequency due to the $\mathbf{B_0}$field. Second, the net magnetization tips from the longitudinal ($\boldsymbol{M_z}$) direction to the transverse ($\boldsymbol{M_{xy}}$) direction at a rate dependent on the instantaneous magnitude of the $\mathbf{B_1}$ field, rotating the magnetization through a flip angle $\propto$ determined by the waveform of the applied $\mathbf{B_1}$field as follows:

$$\propto = \boldsymbol{\gamma} \int \mathbf{B_1(t)dt} \qquad [1.5]$$

After application of a $\mathbf{B_1}$ field with a flip angle $\propto$, the resultant components of the magnetization vector after the RF pulse with the initial conditions at the equilibrium state of $\boldsymbol{M_z}(0) = M_0, \boldsymbol{M_{xy}}(0) = 0$ are:

$$\boldsymbol{M_{xy}} = M_0 \boldsymbol{sin}(\propto) \mathbf{e^{-i\omega_L t}} \qquad [1.6]$$

$$\boldsymbol{M_z} = M_0 \boldsymbol{cos}(\propto) \qquad [1.7]$$

The net magnetization has both longitudinal and transverse components. From a quantum mechanical perspective, the application of the RF pulse provides the energy required for spins to switch from the low energy state to the high energy state. Also, note the difference in the energy between two consecutive nuclear magnetic moment states is equal to the energy of a photon of an RF pulse exactly at the Larmor frequency.

The ability of a weaker RF field -- even in the presence of a much stronger $\mathbf{B_0}$ field -- applied exactly at the Larmor frequency to tip the magnetization away from the

longitudinal direction is referred as the *magnetic resonance phenomenon*. The stored energy is released and the magnetization returns to its equilibrium state after the RF pulse is removed. The net magnetization, having been excited into the transverse plane, recovers back to its equilibrium state, creating a decaying signal that is known as a Free Induction Decay (FID) (Figure 1.1) that can be detected by the scanner hardware through the principles of electromagnetic induction.

1.1.2 Image formation

Of the many atoms which possess nuclear spin and may be imaged using MRI, hydrogen remains by far the most commonly-imaged due to its abundance in the human body and its high gyromagnetic ratio, which provides high sensitivity. In general, the overall process of magnetic resonance image formation can be separated into four

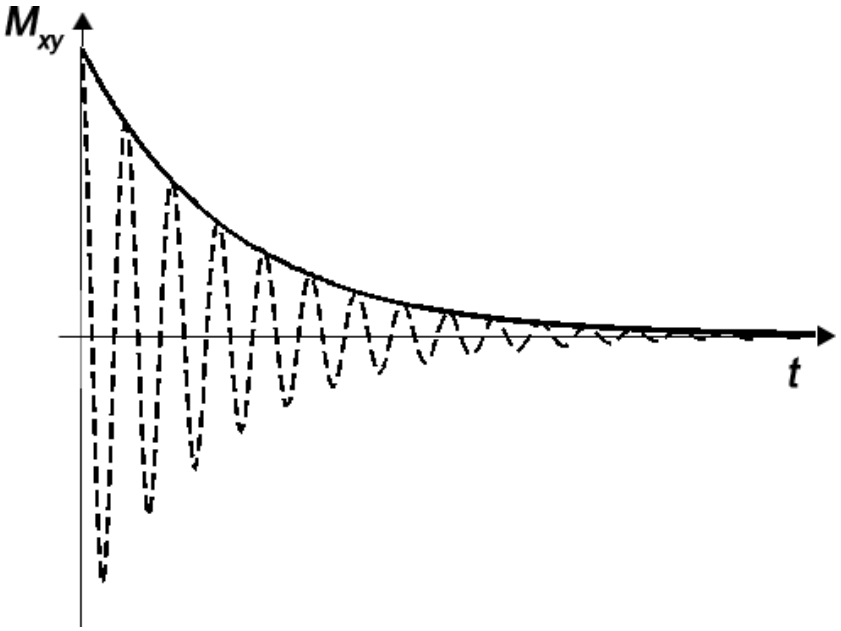

Figure 1.1: *Free Induction Decay (FID). An oscillating and decaying transverse component of the net magnetization detected by a receiver RF coil using principles of electromagnetic induction. Image reprinted with permission from Antkowiak et al(4).*

major steps:

1) signal generation using static $\mathbf{B_0}$ field,

2) manipulation of the signal to a detectable form using the $\mathbf{B_1}$ field to excite the nuclei,

3) the application of magnetic field gradients to encode spatial position information into the received magnetic resonance signal, and

4) signal detection using a receiver RF coil, which is also known as data acquisition or readout.

Importantly, the signal detected by the receiver coil measures the net magnetization of all the hydrogen nuclei, mostly water protons but also fat protons, present in the region sensed by the receiver coil. The first two steps of magnetic resonance image formation were discussed in the above sections; in the following section, the magnetic field gradients will be discussed.

Magnetic field gradient coils cause the magnetic field strength to vary linearly in space, and they are used to spatially distinguish the received signal by exploiting the dependence of the Larmor frequency upon the magnetic field strength. Typically, a slice is selected by applying a magnetic field gradient G_z perpendicular to the imaging plane simultaneously with an RF pulse. The application of the G_z gradient causes protons to have a linearly-varying Larmor frequency along the z-direction. The RF pulse excites protons solely from a specific slice of tissue because only those protons precessing at the frequencies within the applied RF pulse's bandwidth satisfy the resonance condition.

The gradient G_z strength and the bandwidth of the RF pulse determine the slice thickness, while the center frequency of the RF pulse determines the slice position.

To further distinguish the signal from different locations within the imaging plane, a gradient G_x is played along the in-plane x-direction while the signal is recorded. The application of G_x causes the frequency of the received signal to vary as a function of x-position, thereby encoding the x-position information in the frequency of the signal. This step is termed as *frequency encoding* and the x-direction is described as the *frequency encoding direction*. The final spatial dimension, the y-direction, is distinguished using a so-called *phase encoding* gradient G_y, which is played prior to the readout but after the excitation RF pulse. The linear variation in spin frequency for a regulated amount of time leads to the encoding of y-position information in the phase of the spins. For an image whose pixels form an M x N (X by Y) matrix, the phase encoding step is repeated N times in order to uniquely distinguish the phase pattern of every pixel in the y-direction. Each row corresponds to a repetition of the sequence for a different phase encoding gradient. The recorded magnetic resonance signal corresponds to data in 2D spatial frequency space, also known as k-space. Since the measured signal represents the object's spatial frequency content, a 2D Fourier transform can be applied to the k-space data to reconstruct the object in image space.

1.1.3 T1 mapping

After application of an RF pulse, the net magnetization gradually recovers to its thermodynamic equilibrium state and aligns with the external field $\mathbf{B_0}$. Two processes are involved in this return of magnetization to the equilibrium state. One is the gradual

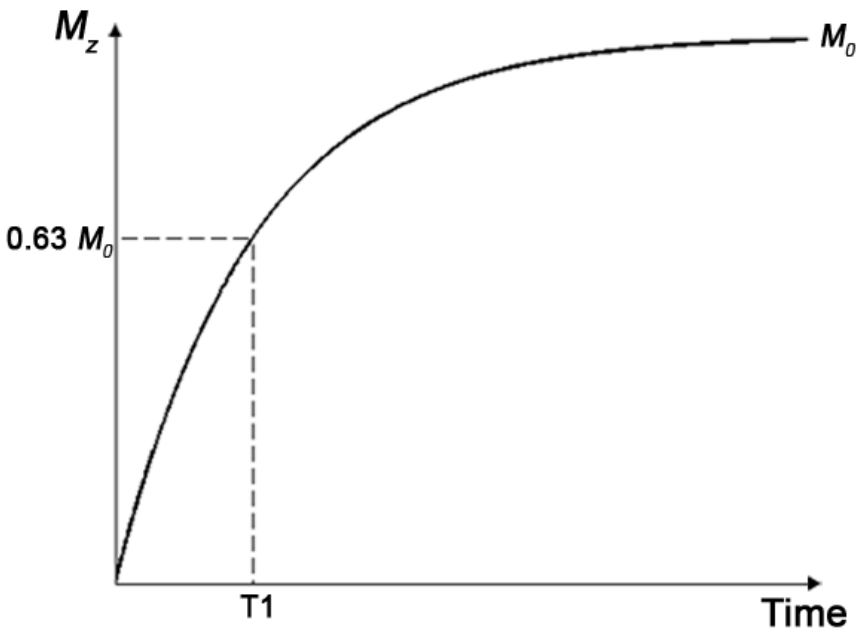

Figure 1.2: *Recovery of the longitudinal component of magnetization from zero illustrating the T1 or spin-lattice relaxation process. Image reprinted with permission from Antkowiak et al(4).*

re-growth of the longitudinal magnetization; the other is the gradual reduction of the transverse magnetization. The former, termed “T1 relaxation” or “spin-lattice relaxation”, is a process in which the longitudinal component of the magnetization vector recovers towards its thermodynamic equilibrium. T1 relaxation is the process in which stored energy in excited spins is transferred back to the surrounding lattice or tissue, causing the excited spins to lose energy and move to the lower-energy, equilibrium state aligned with the main magnetic field. T1 relaxation is modeled as an exponential recovery process, and the time constant governing this exponential recovery process is called the T1 relaxation time or just “T1”.

The T1 value, typically reported in seconds or milliseconds, is the amount of time that it takes for the longitudinal component of magnetization to recover from 0 to 63% of

its equilibrium value (Figure 1.2). The T1 value is tissue-dependent and can be altered using exogenous contrast agents. To accurately measure the T1 value within an object, an image acquisition method called *T1 mapping* is used. In T1 mapping, T1 values are calculated for each spatial position, pixel-by-pixel, within the entire field of view (FOV).

1.2 MYOCARDIAL FIBROSIS

Myocardial tissue is primarily comprised of myocytes, fibroblasts, endothelial cells and an interstitium which is formed by a unique and adaptable extracellular matrix (ECM). The ECM provides a surrounding in which the myocytes, fibroblasts, and endothelial cells communicate and function(5). The ECM of the heart is primarily comprised of fibrillar collagen and matricellular proteins that modulate the interactions between myocytes and ECM(5). The fibrillar collagen network plays a critical role in the maintenance of the ventricular shape, size, and function under physiological conditions(1). Myocardial fibrosis, defined by a significant increase in the collagen volume fraction of the myocardial tissue, is one of the most common histological features of the failing heart(1). It is ubiquitously present in diseases affecting the cardiovascular system. Recent studies have also shown that myocardial fibrosis is a major independent predictor of adverse cardiovascular outcome(6-8). It is associated with the worsening of ventricular systolic function, abnormal cardiac remodeling, and increased ventricular stiffness(9-11).

Various pathophysiological mechanisms lead to myocardial fibrosis. Some are acute, while others are progressive and potentially reversible. Based on the underlying

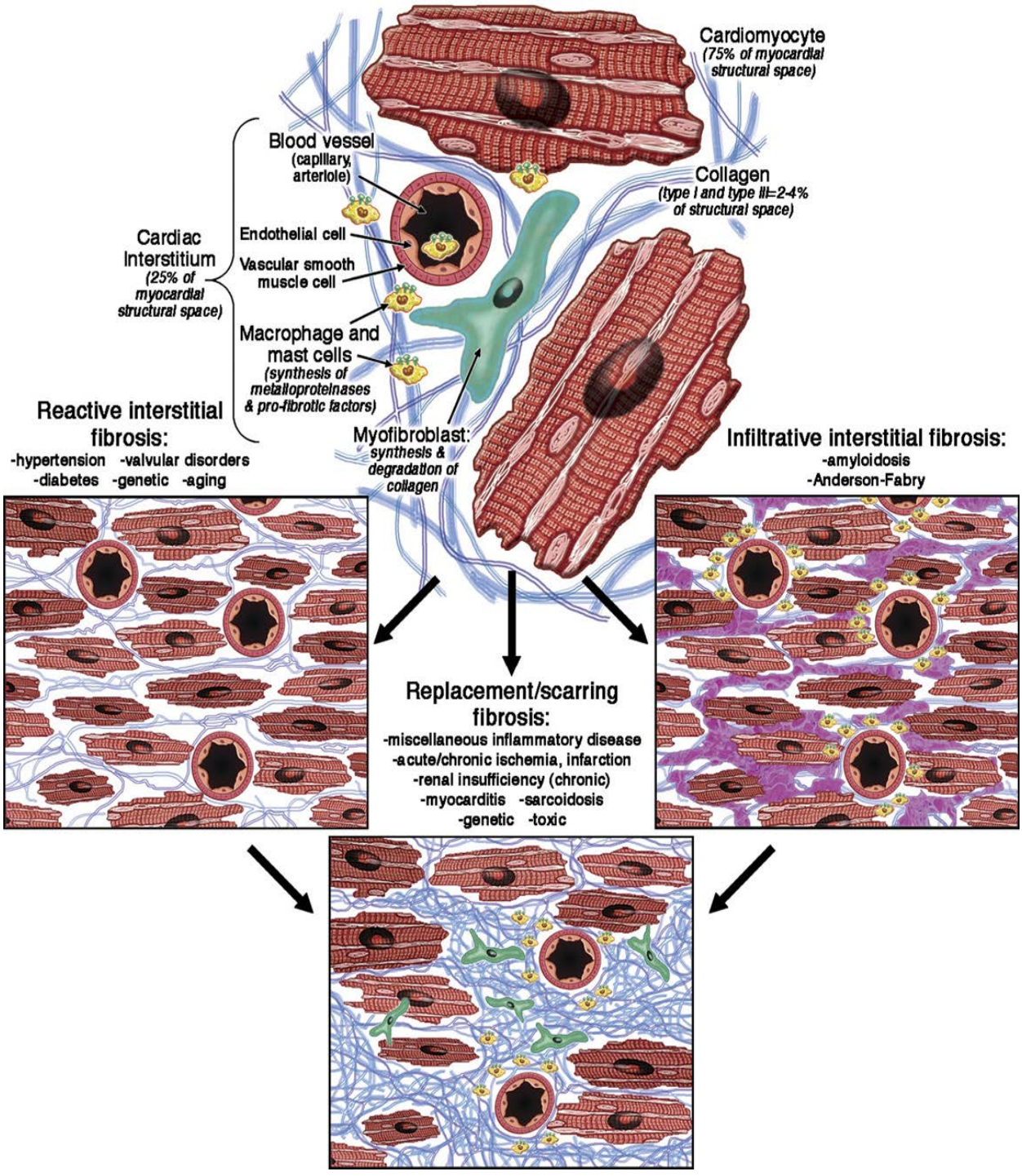

Figure 1.3: *Myocardial fibrosis. A cartoon illustrating different components of myocardial tissue under healthy and different types of fibrotic conditions. Image reprinted with permission from Mewton et al(1).*

cardiomyopathic process, three different types of myocardial fibrosis have been reported (Figure 1.3).

1.2.1 Reactive interstitial fibrosis

Reactive interstitial fibrosis has been described in the heart in hypertension, diabetes mellitus, idiopathic dilated cardiomyopathy, left ventricular pressure-overload and volume-overload states induced by valvular disease, in remote myocardium after infarction, and in the ageing heart(12-17). Its onset is progressive and follows the increase in collagen synthesis due to different stimuli to myofibroblasts, such as the activation of the rennin-angiotensin aldosterone system and the beta-adrenergic system and metabolic disturbances induced by hyperglycemia(12,15-17). Reactive interstitial fibrosis has a diffuse distribution within the interstitium, although it can also be specifically perivascular(17). Importantly, reactive interstitial fibrosis is reversible with therapy(1,18-20).

1.2.2 Infiltrative interstitial fibrosis

Infiltrative interstitial myocardial fibrosis has been described in patients with infiltrative diseases such as cardiac amyloidosis and Anderson-Fabry disease(21,22). For optimal therapeutic management, the early detection of cardiac involvement in these infiltrative diseases is extremely important(1). This subtype of interstitial cardiac fibrosis is induced by progressive deposition of insoluble proteins such as amyloid or glycosphingolipids, and its pathophysiological patterns are similar to reactive interstitial fibrosis(1).

1.2.3 Replacement fibrosis

Replacement, or scarring, fibrosis has been shown to develop in patients with ischemic cardiomyopathy, myocarditis, hypertrophic cardiomyopathy, sarcoidosis, chronic renal insufficiency, toxic cardiomyopathies and miscellaneous inflammatory disease(23-25). Replacement fibrosis is irreversible(16,26). Reactive fibrosis and infiltrative fibrosis ultimately progress to replacement fibrosis in later stages of the disease, often indicating the terminal stages of the heart failure(1). Replacement fibrosis occurs when myocyte integrity is affected by cell damage or necrosis, leading to the replacement of myocytes by plexiform fibrosis. Replacement fibrosis can have a localized distribution or a diffuse distribution depending on the underlying etiology(1).

1.2.4 Assessment of fibrosis using T1 mapping

1.2.4.a Estimation of the extracellular volume fraction using an exogenous, extracellular contrast agent

As mentioned earlier, myocardial fibrosis causes a substantial increase in the collagen volume fraction of the myocardial tissue. Since the ECM is primarily comprised of fibrillar collagen, an increase in collagen volume fraction leads to a proportional increase in the extracellular volume fraction (ECV) of the myocardial tissue. Thus, expansion of the myocardial ECV may be used as a surrogate marker of myocardial fibrosis.

Suppose that an exogenous contrast agent ‘A,’ with an extracellular distribution volume (which importantly includes the collagen volume fraction), is introduced into the myocardium. The myocardial partition coefficient for this extracellular agent, λ_A, is

defined as the ratio of the concentration of the agent in tissue (C_t) to the concentration of the agent in blood (C_b).

$$\lambda_A = \frac{C_t}{C_b} \quad [1.8]$$

At an equilibrium state, the concentration of the contrast agent in the extravascular and extracellular space (C_e) is equal to the plasma concentration (C_p):

$$C_p = \frac{C_b}{(1 - Hct)} = C_e \quad [1.9]$$

where Hct represents the blood hematocrit: the blood pool volume that is accessible to the contrast agent. Let V_e and V_p denote the volume fraction of the extravascular and extracellular and plasma spaces, respectively. The tissue concentration of the agent can be expressed as the weighted average of the concentrations in the component spaces, with the respective volume fractions as the weighting factors:

$$C_t = V_e C_e + V_p C_p \quad [1.10]$$

Combining the above equations and considering the equilibrium state assumption ($C_p = C_e$), the equation for ECV can be expressed in terms of blood hematocrit and concentrations of agent A in blood and myocardial tissue(27):

$$ECV = V_e + V_p = (1 - Hct) \cdot \lambda_A = (1 - Hct) \cdot \left(\frac{C_t}{C_b}\right) \quad [1.11]$$

From these equations, it can be seen that the myocardial ECV, which may be a surrogate biomarker of fibrosis in pathology, can be estimated if the hematocrit, blood

concentration, and myocardial concentration of the extracellular contrast agent are known[A].

1.2.4.b Measuring the concentration of a contrast agent using T1 mapping

As mentioned earlier, T1 relaxation is a process in which the stored energy in the excited spins (and in particular for our purposes, protons) is transferred back to the surrounding lattice or tissue, causing the longitudinal component of the magnetization to return to its equilibrium state. The T1 value of the protons is dependent on their local chemical environment.

All elements with unpaired electrons possess nuclear spin and a corresponding magnetic moment. However, this magnetic field is not static: it oscillates due to the motion of the unpaired electrons. If this oscillation is at or near the Larmor frequency of protons, then the exchange of the stored energy from protons in the higher energy state to the surrounding tissue occurs more rapidly due to dipole-diploe interactions between the protons and the oscillating local magnetic field. The local interaction with an element having unpaired electrons -- such as an exogenous contrast agent -- shortens the T1 value of the protons. Furthermore, the degree of T1 shortening that occurs is proportional to the contrast agent's concentration.

One element with unpaired electrons is gadolinium (Gd), which possesses seven unpaired electrons. It is the most commonly-used clinical MRI T1-shortening contrast agent. Since the fluctuating magnetic field due to unpaired electrons does not extend

[A] Derivation from Jerosch-Herold *et al*(27).

very far in space, the T1-shortening effect depends only on the local concentration of gadolinium(28) as follows:

$$\frac{1}{T1_{with\ Gd}} = \frac{1}{T1_{without\ Gd}} + (Gd\ relaxivity) \times (Gd\ concentration) \qquad [1.12]$$

where *Gd relaxivity* is a constant that depends on the chemical specifics of the particular gadolinium-based agent being used. Since the elemental form of gadolinium is toxic, a metabolically-inert, chelated version of gadolinium that is completely excreted from the body is used in humans. By non-invasively measuring T1 with and without the gadolinium-based contrast agent, one can estimate the *in vivo* Gd concentration within the tissue if the Gd relaxivity, either provided by the manufacturer or calculated using other techniques, is known. The relationship between Gd concentration and those parameters is as follows:

$$Gd\ concentration = \left(\frac{1}{T1_{with\ Gd}} - \frac{1}{T1_{without\ Gd}}\right) \cdot \left(\frac{1}{Gd\ relaxivity}\right) \qquad [1.13]$$

Gadolinium-based contrast agents have extracellular distribution. Therefore, the estimation of the myocardial ECV can be made by measuring the hematocrit and the concentrations of the Gd-based contrast agent in the blood and myocardium. The concentrations of Gd-based contrast agent in the blood and myocardial tissue can be estimated using the relation in equation 1.13.

$$ECV_{myo} = (1 - Hct) \cdot \left(\frac{C_{myo}}{C_b}\right) = (1 - Hct) \cdot \left(\frac{\frac{1}{T1_{myo\ with\ Gd}} - \frac{1}{T1_{myo\ without\ Gd}}}{\frac{1}{T1_{blood\ with\ Gd}} - \frac{1}{T1_{blood\ without\ Gd}}}\right) \qquad [1.14]$$

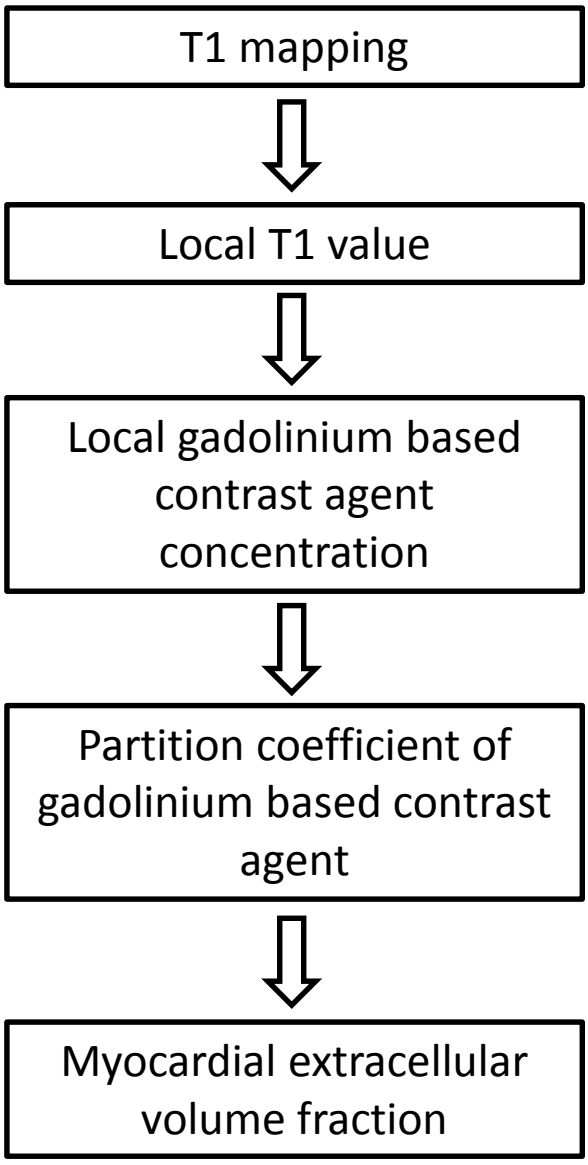

Figure 1.4: *Assessment of myocardial fibrosis using T1 mapping MRI. Flow chart explaining the calculation of myocardial extracellular volume fraction using T1 mapping MRI.*

In other words, the myocardial partition coefficient for gadolinium (λ_{Gd}) is the slope of the linear fit of 1/(myocardial T1) vs 1/ (LV blood pool T1), which are each measured at

various time points before and after injection of the contrast agent. Thus, the myocardial ECV, a surrogate marker of myocardial fibrosis, can be non-invasively estimated by performing T1 mapping MRI of the heart before and serially after injection of a gadolinium-based contrast agent (Figure 1.4).

1.3 PULMONARY ARTERIAL HYPERTENSION (PAH)

1.3.1 Background of PAH

(In the following section, text in quotation marks is taken directly from the cited source)

Pulmonary hypertension is a hemodynamic and pathophysiological state characterized by an elevated pressure in the pulmonary artery(2,29,30). Increased pulmonary pressure can be caused by many different mechanisms(29). For example, in patients with pulmonary hypertension due to lung diseases, elevated pulmonary pressure is secondary to increased left atrial pressure; while in patients with chronic thromboembolic pulmonary hypertension, the pulmonary pressure's elevation is caused by mechanical obstruction of the pulmonary vascular (29). The classification (Table 1.1) of pulmonary hypertension is based on clinical and pathophysiological characteristics(2,29):

Group 1: Pulmonary arterial hypertension (PAH), which can be idiopathic or associated with other conditions.

Group 2: Pulmonary hypertension due to left heart diseases.

Group 3: Pulmonary hypertension due to lung diseases and/or hypoxia

Table 1.1: Classification of Pulmonary Hypertension. Table reprinted with permission from Simonneau *et al(2)*

1. Pulmonary arterial hypertension
   - 1.1. Idiopathic PAH
   - 1.2. Heritable PAH
     - 1.2.1. Bone morphogenic protein receptor type II
     - 1.2.2. Activin-like receptor kinase-1, endoglin, mothers against decapentaplegic 9, caveolin-1, and KCNK3
     - 1.2.3. Unknown
   - 1.3. Drug and toxin induced
   - 1.4. Associated with:
     - 1.4.1. Connective tissue disease
     - 1.4.2. HIV infection
     - 1.4.3. Portal hypertension
     - 1.4.4. Congenital heart diseases
     - 1.4.5. Schistosomiasis

1’ Pulmonary veno-occlusive disease and/or pulmonary capillary hemangiomatosis

1” Persistent pulmonary hypertension of the newborn (PPHN)

2. Pulmonary hypertension due to left heart disease
   - 2.1. Left ventricular systolic dysfunction
   - 2.2. Left ventricular diastolic dysfunction
   - 2.3. Valvular disease
   - 2.4. Congenital/acquired left heart inflow/outflow tract obstruction and congenital cardiomyopathies
3. Pulmonary hypertension due to lung diseases and/or hypoxia
   - 3.1. Chronic obstructive pulmonary disease
   - 3.2. Interstitial lung disease
   - 3.3. Other pulmonary disease with mixed restrictive and obstructive pattern
   - 3.4. Sleep-disordered breathing
   - 3.5. Alveolar hypoventilation disorders
   - 3.6. Chronic exposure to high altitude
   - 3.7. Developmental lung diseases
4. Chronic thromboembolic pulmonary hypertension (CTEPH)
5. Pulmonary hypertension with unclear multifactorial mechanisms
   - 5.1. Hematologic disorders: chronic hemolytic anemia, myeloproliferative disorders, splenectomy
   - 5.2. Systemic disorders: sarcoidosis, pulmonary histiocytosis, lymphangioleiomyomatosis
   - 5.3. Metabolic disorders: glycogen storage disease, Gaucher disease, thyroid disorders
   - 5.4. Others: tomoral obstruction, fibrosing mediastinitis, chronic renal failure, segmental PH

Group 4: Chronic thromboembolic pulmonary hypertension.

Group 5: Pulmonary hypertension with unclear multifactorial mechanisms.

“Pulmonary arterial hypertension (PAH) is caused by restricted flow through the pulmonary arterial circulation, leading to an increase in pulmonary vascular resistance and ultimately resulting in right heart failure”(3). The prevalence of PAH is about 15 per million, based on evidence from a French registry(31). It is a progressive and debilitating disease with high morbidity and mortality(29,31,32): “specifically, PAH presents a 15% mortality within 1 year on modern therapy”(3).

The loss of vascular luminal cross section is the predominant cause of the increase in the pulmonary vascular resistance in PAH(3). The mechanism causing the loss of vascular luminal cross section in PAH includes an imbalance of cellular proliferation and apoptosis. PAH is characterized by various arterial abnormalities such as intimal hyperplasia, medial hypertrophy, adventitial proliferation, thrombosis in situ, varying degrees of inflammation, and plexiform arteriopathy(3). In another 20% of patients, excessive vasoconstriction plays a significant role(3).

“The current hemodynamic definition of PAH is a mean pulmonary artery pressure (mPAP) greater than 25 mm Hg; a pulmonary capillary wedge pressure, left atrial pressure, or left ventricular end-diastolic pressure less than or equal to 15 mm Hg; and a pulmonary vascular resistance greater than 3 Wood units”(3). Echocardiography is the most appropriate study for preliminary evaluation of patients suspected with PAH(3). However, a complete right heart catheterization (RHC) is required to confirm the diagnosis of PAH(3). “The following general steps are employed in the diagnosis of

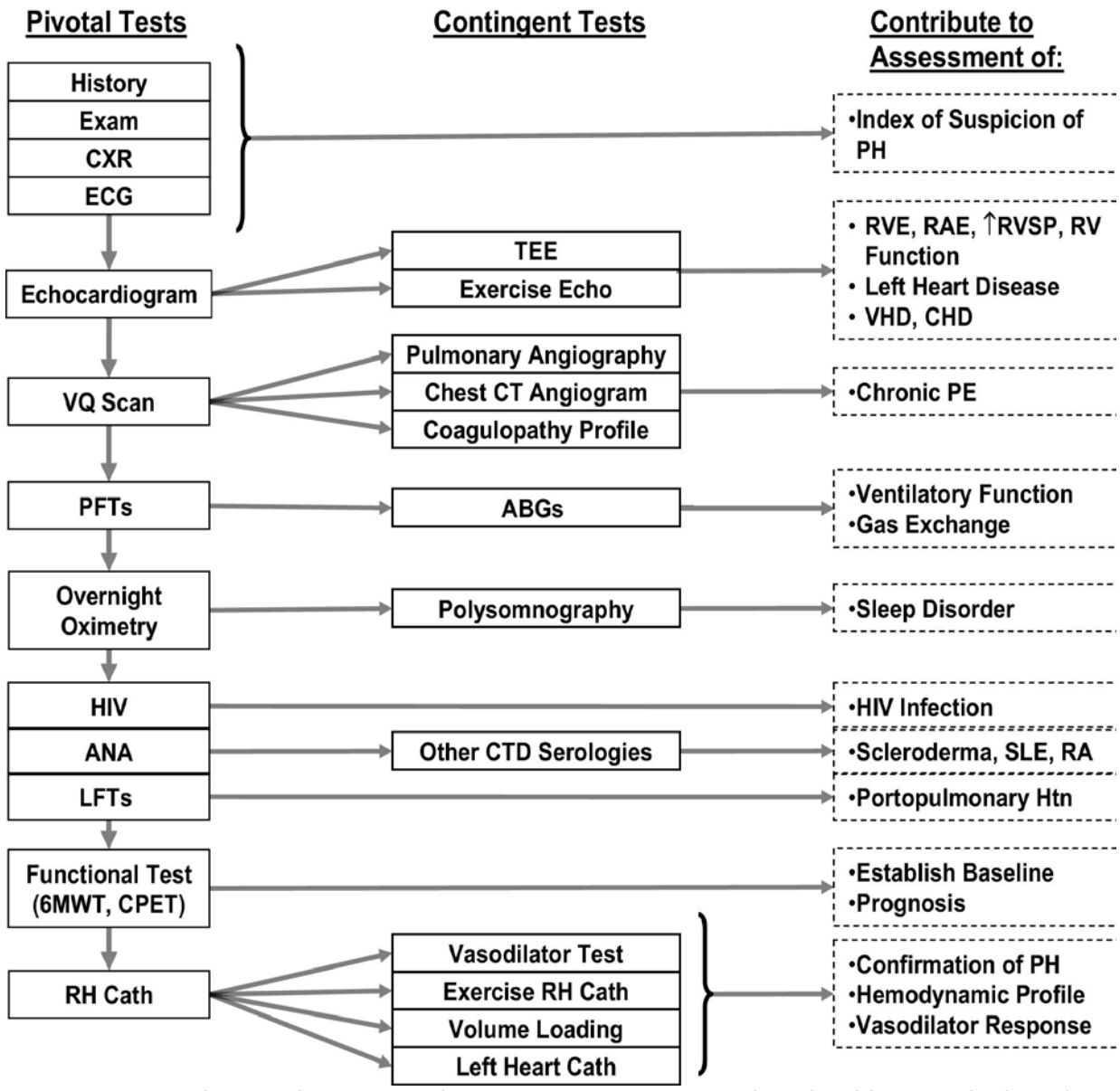

Figure 1.5: *Diagnostic approach to PAH. Image reprinted with permission from McLaughlin et al(3).*

PAH: 1) detection of a substrate in which the likelihood of a pulmonary vasculopathy may be increased; 2) discovery of the presence of pulmonary hypertension; 3) classification of the type of pulmonary hypertension; 4) confirmation of the presence of suspected pulmonary hypertension; and 5) determination of an appropriate treatment

category”(3). The detailed diagnostic strategy for assessment of PAH is shown in figure 1.5(3). “Poor exercise capacity based on a 6-minute walk (6MW) test or cardiopulmonary exercise test, high right atrial pressure, significant right ventricular dysfunction, evidence of RV failure, low cardiac index, elevated brain natriuretic peptide (BNP), and underlying diagnosis of scleroderma spectrum diseases are predictors of poor prognosis of PAH”(3).

1.3.2 Right ventricle in PAH

As mentioned earlier, PAH is characterized by an increase in pulmonary vascular resistance due to the presence of pulmonary vasculopathy(33-35). This elevation in pulmonary vascular resistance leads to an increase in right ventricular afterload. The right ventricle (RV) attempts to compensate for the increased afterload by increasing its contractility(36). The RV can to some degree overcome acute increases in RV afterload(36); however, the increased afterload in PAH is above the limit for a healthy RV to overcome(36). Following this increased RV afterload, “the RV begins to undergo concentric remodeling, with the right atrial pressure remaining normal despite a steep increase in mPAP, and cardiac index is maintained”(37). The first response is adaptive RV myocardial hypertrophy(36,37), which cannot compete with sustained increase in the pressure overload(37). Here, the RV adaptation stops despite a further increase in the afterload(37). The specific mechanisms that underlie the halt of the RV adaptation remain unclear(37). Eventually, to provide compensatory preload and to maintain stroke volume despite reduced fractional shortening, the RV chamber pools more blood resulting in RV dilation(36). “As contractile weakening progresses, decompensated RV failure occurs, characterized by increased filling pressures, diastolic dysfunction,

diminished cardiac output, and worsened tricuspid regurgitation"(36). Patient survival is primarily determined by the ability of the RV to adapt to the afterload, and ultimately the main cause of death in patients with PAH is RV failure(38). Therefore, therapies improving or normalizing pulmonary pressure in patients with PAH, if unaccompanied by parallel improvement in RV hemodynamics and function, do not necessarily lead to clinical improvement and prolonged survival(36).

1.4 MOTIVATION

Gadolinium-enhanced T1 mapping MRI is becoming increasingly important in the evaluation of various cardiovascular diseases, and it has been applied to quantify both diffuse fibrosis(10,27,39-41) and focal fibrosis(40,42-44) in the left ventricle (LV). It has also shown potential for the diagnosis of several diseases affecting the LV myocardial ECV(40,45,46). Modified Look-Locker inversion recovery (MOLLI)(47) and shortened MOLLI (ShMOLLI)(48) are the current widely-used T1 mapping techniques for the heart. However, their spatial resolution is limited due to cardiac and respiratory motion during image acquisition. These techniques employ readout acquisition windows of approximately 200 ms to avoid artifacts due to cardiac motion and breath-holding to reduce respiratory artifacts. They typically yield in-plane spatial resolutions in the range of 2.0 – 2.4 mm^2, making them well-suited for imaging structures such as the LV wall that are on the order of 1 cm^2. Due to the spatial resolution constraints, T1 mapping of the heart has generally been confined to the LV.

Assessment of myocardial fibrosis would be valuable in PAH(49,50), arrhythmogenic right ventricular cardiomyopathy(51), congenital heart disease, and

atrial fibrillation(52), conditions where assessment of the thinner RV and left atrial walls is necessary. For imaging structures with complex geometries such as the RV wall, not only is high in-plane resolution an important factor, but high through-plane resolution is also crucial. Since high-resolution 2D acquisitions are limited by SNR considerations and cannot provide a continuous 3D coverage, there is a need for a high resolution cardiac 3D T1 mapping methods. Furthermore, continuous 3D T1 mapping coverage is necessary for quantitative assessment of other structures, such as peri-infarct region.

As described earlier, PAH is a devastating disease with high mortality, and right heart failure is the main cause of mortality in these patients (29,31,32,37,53). The ultimate goal of the therapy for PAH is to protect the RV(37). Pressure overload in PAH leads to progressive RV hypertrophy, systolic dysfunction, and dilatation, resulting in a series of complex changes in cardiomyocytes and their extracellular matrix(35,37). The extent of focal fibrosis at the septal RV insertion sites, measured using late gadolinium enhancement (LGE) MRI, has been shown to positively correlate with increased afterload and inversely correlate with RV performance in PAH patients(49,50). Quantitative assessment of RV myocardial fibrosis might then be a valuable tool for improving patient management. Specifically, noninvasive quantification of RV fibrosis, using T1 mapping to calculate the ECV, may potentially improve patient management by providing a tool to assess, design and establish an optimal therapeutic approach.

1.5 SPECIFIC AIMS

The overall goal of this dissertation is to develop and apply noninvasive high-resolution T1 mapping methods for assessment of myocardial fibrosis in thin structures such as the RV wall.

Specific Aim #1 is to develop a high resolution 2D cardiac T1 mapping technique to image the thin wall of the RV. This aim includes the following sub-aims: (a) to develop a free breathing 2D MRI technique capable of acquiring high resolution T1 mapping data (b) to accelerate image acquisition by implementing compressed sensing- and parallel imaging- based image reconstruction algorithms, additionally employing an adaptive data acquisition algorithm (c) to validate the proposed method in phantoms and to compare its ability to image the RV wall with MOLLI in healthy volunteers.

Current cardiac T1 mapping techniques provide limited spatial resolution due to the constraints imposed by breath-holding requirements and a limited data acquisition window due to cardiac motion. In this aim, we developed a novel high resolution free-breathing cardiac T1 mapping method which uses navigator-gating and compressed sensing to overcome these constraints. We also developed a novel adaptive data acquisition algorithm, which in real-time accounts for the interplay between navigator-gating and undersampling patterns well-suited for compressed sensing, to reduce the acquisition time. The material for this aim is covered in Chapter 2 and this has been previously published in Mehta *et al(54).*

Specific Aim #2 is to measure right ventricular myocardial fibrosis in patients with PAH using the novel T1 mapping technique developed in Aim #1. Specifically, we aim to

test the hypotheses that (a) RV ECV is elevated in patients with PAH compared to reference subjects, and (b) RV ECV correlates with the increase in RV systolic pressure, RV end diastolic volume index, and decreased in RV ejection fraction in these patients.

In this aim, we applied the method developed in Aim #1 to non-invasively measure the RV myocardial ECV in the patients with PAH. To the best of our knowledge, this is the first study to non-invasively assess the changes in the RV myocardial ECV and evaluate the correlation of the RV myocardial ECV with RV pressure overload, RV systolic function, and RV dilation in the patients with PAH. The material for this Specific Aim is covered in Chapter 3, and it is not yet published.

Specific Aim #3 is to extend the T1 mapping method developed in Aim #1 to perform high-resolution 3D T1 mapping of the heart within a clinically-acceptable scan time. This aim includes the following sub-aims: (a) to develop a free-breathing 3D cardiac T1 mapping technique (b) to further accelerate data acquisition by undersampling along two data dimensions (the phase and partition encoding dimensions) and adopt a regional sparsity-based 4D image reconstruction algorithm (c) to validate this proposed 3D T1 mapping method by comparing it to 2D MOLLI and the 2D T1 mapping method developed in Aim #1 in healthy subjects.

In general, 3D acquisitions provide higher SNR than 2D acquisitions at the expense of longer imaging times. The additional spatial dimension and increased SNR in 3D acquisitions allow higher acceleration rates than in 2D acquisitions. In this Aim, we developed an image reconstruction algorithm that employs 3D region-based

sparsity, a partial Fourier acquisition, and parallel imaging to improve the reconstruction quality and increase the acceleration rate. Additionally, an adaptive sampling strategy, which combines probability density function-based and Poisson-disc-based sampling criteria, was developed to improve the reconstruction quality. The material for this Specific Aim is covered in Chapter 4, and it is not yet published.

Chapter 2

Development of high resolution two-dimensional T1 mapping technique

2.1 INTRODUCTION:

Gadolinium-enhanced T1 mapping is becoming increasingly important in the evaluation of various cardiovascular diseases. Modified Look-Locker inversion recovery imaging (MOLLI)(47) and shortened MOLLI (ShMOLLI)(48) are the most widely used cardiac T1 mapping methods. Employing single-shot imaging, acquisition windows of approximately 200 ms, and breath-holding to reduce respiratory artifact, these techniques typically yield in-plane spatial resolution in the range of 1.8 – 2.4 mm^2 and are well-suited for T1 mapping of structures on the order of 1 cm^2, such as the wall of the LV.

While breath-hold techniques such as MOLLI and ShMOLLI are successfully applied for many applications, others could benefit from higher spatial resolution. For example, to assess fibrosis in the peri-infarct zone or the walls of the right ventricle and the atria, higher spatial resolution would be needed. In the present study, we sought to develop a cardiac T1 mapping sequence capable of acquiring higher resolution images within a clinically acceptable scan time.

We performed three modifications to a standard MOLLI sequence(47). First, instead of using a breath-hold acquisition we used navigator gating to accept or reject the acquired data. With this modification the image acquisition time can exceed that of breath-hold methods, which provides more flexibility in sequence design. To increase spatial resolution, the second modification was to implement a segmented readout, instead of a single-shot readout, thereby acquiring the k-space data for a single image over multiple heartbeats. With a segmented readout, the limited acquisition window imposed by cardiac motion does not limit spatial resolution. However, segmenting the readout increases the total scan time. Therefore, to reduce the total scan time, the third modification was to accelerate the scan using k-t undersampling and to use compressed sensing(55-57) (CS) with parallel imaging(58) for reconstruction. CS has previously been shown to be well-suited for T1 mapping, and CS theory(55-57) recommends randomly acquiring the k-space data. As we propose using both navigator gating, which rejects data based on the diaphragm position, and CS, where random sampling is preferred, our study included an investigation of the interaction between navigator-based data rejection and undersampling patterns that are well-suited for CS. Specifically, we developed and implemented an adaptive data acquisition method that, in real time and based on the current k-t sampling pattern, recomputes an updated k-t sampling pattern that is well-suited for CS reconstruction and T1 estimation and which reduces the total scan time.

The proposed sequence was named Accelerated and Navigator-Gated look-locker Imaging for cardiac T1 Estimation (ANGIE). Computer simulations were performed to evaluate and compare the image quality that was achieved using two

different k-t undersampling strategies. ANGIE, using the better undersampling strategy, was compared to MOLLI for T1 mapping of the LV in healthy volunteers. Also, to demonstrate new capabilities of high-resolution T1 mapping with ANGIE, we compared MOLLI and ANGIE for T1 mapping of the wall of the right ventricle (RV).

2.2 THEORY:

Data sampling patterns suitable for CS often utilize a fully-sampled or nearly-fully-sampled central k-space region and a randomly-undersampled outer k-space region. For most current CS applications, a fixed, predetermined sampling pattern is used. However, for navigator-gated methods such as ANGIE, decisions regarding acceptance and rejection of the data occur during the scan, and completing sampling patterns with associated acceleration factors determined *a priori* may lead to very long acquisition times. An adaptive acquisition strategy(59), which makes real-time adjustments to the k-t sampling pattern based on which data have and have not been acquired may be used to reduce the total scan time while also collecting k-t data that are well-suited to image reconstruction using CS.

In addition to an adaptive acquisition, we also investigated the use of criteria to stop the acquisition. Since ANGIE uses CS to accelerate a T1 mapping acquisition, accurate CS reconstruction and precise T1 estimation are the two crucial factors that should determine the ANGIE data sampling method. To minimize the scan time for ANGIE, a stopping criterion to halt the acquisition should also be based on the capability to perform an accurate CS reconstruction and a precise T1 estimation. The point spread function (PSF) characterizes interference in the image due to data

undersampling, and the transform point spread function (TPSF) similarly characterizes interference in the transform domain. The transform side lobe-to-peak ratio (TSPR) is the normalized maximum possible interference occurring in the TPSF, defined by TSPR = $max_{i\neq j}\left|\frac{TPSF(i,j)}{TPSF(i,i)}\right|$ (57), and is a simplified measure of the incoherence and the severity of artifacts due to undersampling(57,60,61). Thus, we used the TSPR as a metric of CS reconstruction accuracy.

Another measure, the Cramer Rao lower bound (CRLB), provides the lowest achievable variance of an estimate for a particular parameter in a specific fitting model. In the case of T1 mapping, the parameter of interest is T1, and the CRLB indicates the precision in the T1 measurement given the sampled inversion time (TI) points. The CRLB has been used for the design of optimal TI sampling for T1 estimation previously(62,63). In cardiac applications, TI values are often governed by heart rate; thus, in ANGIE the TI values are determined by the timing of the ECG, and the CRLB is used to assess the precision of the T1 estimate. Hence, the CRLB is used to measure the sufficiency of the sampled TI values. For the CRLB calculation we used a three parameter exponential model with an independent and identically distributed Gaussian noise model.

$$M_z(t_j) = A + Be^{-t_j/T} + \mathcal{N}(0,\sigma^2) \qquad [2.1]$$

where t_j is the jth inversion time, T is the apparent T1, and σ is the noise standard deviation. Based on these models, the elements of the Fisher information matrix (F) and the CLRB are given as

$$F_{11} = \frac{N}{\sigma^2},$$

$$F_{22} = \frac{1}{\sigma^2} \sum_{j=1}^{N} e^{-2j/T},$$

$$F_{33} = \frac{B^2}{\sigma^2 T^4} \sum_{j=1}^{N} t_j^2 \, e^{-2j/T},$$

$$F_{12} = F_{21} = \frac{1}{\sigma^2} \sum_{j=1}^{N} e^{-j/T},$$

$$F_{13} = F_{31} = \frac{B}{\sigma^2 T^2} \sum_{j=1}^{N} t_j \, e^{-j/T},$$

$$F_{23} = F_{32} = \frac{B}{\sigma^2 T^2} \sum_{j=1}^{N} t_j \, e^{-2j/T},$$

$$CRLB = F_{33}^{-1} \qquad [2.2]$$

where N is the number of inversion times. The CRLB was calculated using equation 2.2, the sampled TI values, and the nominal values of the parameters to be estimated (T1 and B)(62,63).

2.3 METHODS:

2.3.1 Pulse sequence

The ANGIE pulse sequence is illustrated in figure 2.1. The basic acquisition is comprised of an inversion recovery Look-Locker experiment(64) with an inversion pulse followed by four consecutive ECG-triggered data acquisitions and a recovery period of two R-R intervals. To ensure that images are acquired at a consistent cardiac phase, the data acquisition is performed at a fixed delay time, TD, after R-wave detection. Each

data acquisition block includes a navigator echo, an optional fat saturation module, a set of catalyzing radio frequency (RF) pulses and a segmented readout module. The basic acquisition block is repeated to acquire all of the required readout segments and to acquire images at various inversion times. The navigator echo, formed using orthogonal slice-selective 90^0 and 180^0 RF pulses, is typically placed on the right hemi-diaphragm(65). The navigator acceptance window was set such that data not acquired during end expiration were discarded. The readout module consisted of a segmented balanced SSFP acquisition. Each readout was preceded by a train of 10 catalyzing RF pulses with Kaiser-Bessel window ramped flip angles to dampen the transient signal oscillations(66).

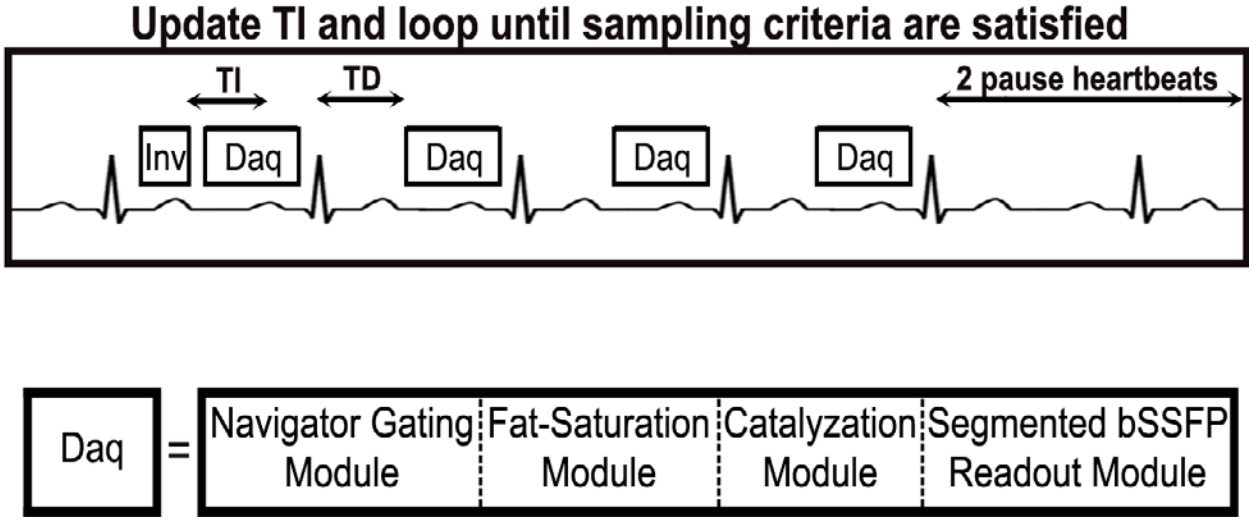

Figure 2.1: *A diagram showing the ANGIE pulse sequence scheme. This instance of ANGIE utilizes an inversion-recovery Look-Locker experiment with four ECG-triggered data acquisition modules and a waiting period of two R-R intervals. The sequence is repeated, after updating TI, until the stopping criteria are satisfied. The data acquisition*

module is comprised of a navigator-gating module, fat suppression, a set of catalyzing RF pulses, and a segmented balanced SSFP readout.

2.3.2 Adaptive acquisition algorithm

Figure 2.2A illustrates the flow of the adaptive acquisition algorithm. The various panels in Figure 2.2 assume that the ANGIE scan is in progress. Based on the current k_y-t sampling pattern (Figure 2.2B), which has been influenced by navigator acceptance and rejection of data, the algorithm computes the phase-encode lines that should be acquired next (Figure 2.2C), in order to achieve CS-suitable sampling and reconstruction. Next, the navigator is played to record the position of the diaphragm and the data are acquired. Based on the position of diaphragm, the acquired data are either accepted or rejected, and the current k_y-t sampling pattern is updated.

Suppose, for illustration, that the diaphragm was within the acceptance window and the acquired data were accepted. Then the updated k_y-t sampling pattern would appear as shown in Figure 2.2D. Next, the algorithm calculates the TSPR and the CRLB to measure the suitability of the entire k_y-t dataset to perform accurate CS reconstruction and precise T1 estimation, respectively. The acquisition is stopped only if both the TSPR and the CRLB values are below the corresponding threshold values, to ensure that both the conditions are satisfied. Otherwise the acquisition continues. In the present implementation, the initial 12.5% of the phase encode lines for each time-point correspond to the central fully sampled region and the remaining 87.5% are selected from the higher-frequency undersampled region based on a selection strategy. The adaptive selection strategy considers the entire k_y-t space, and computes the next

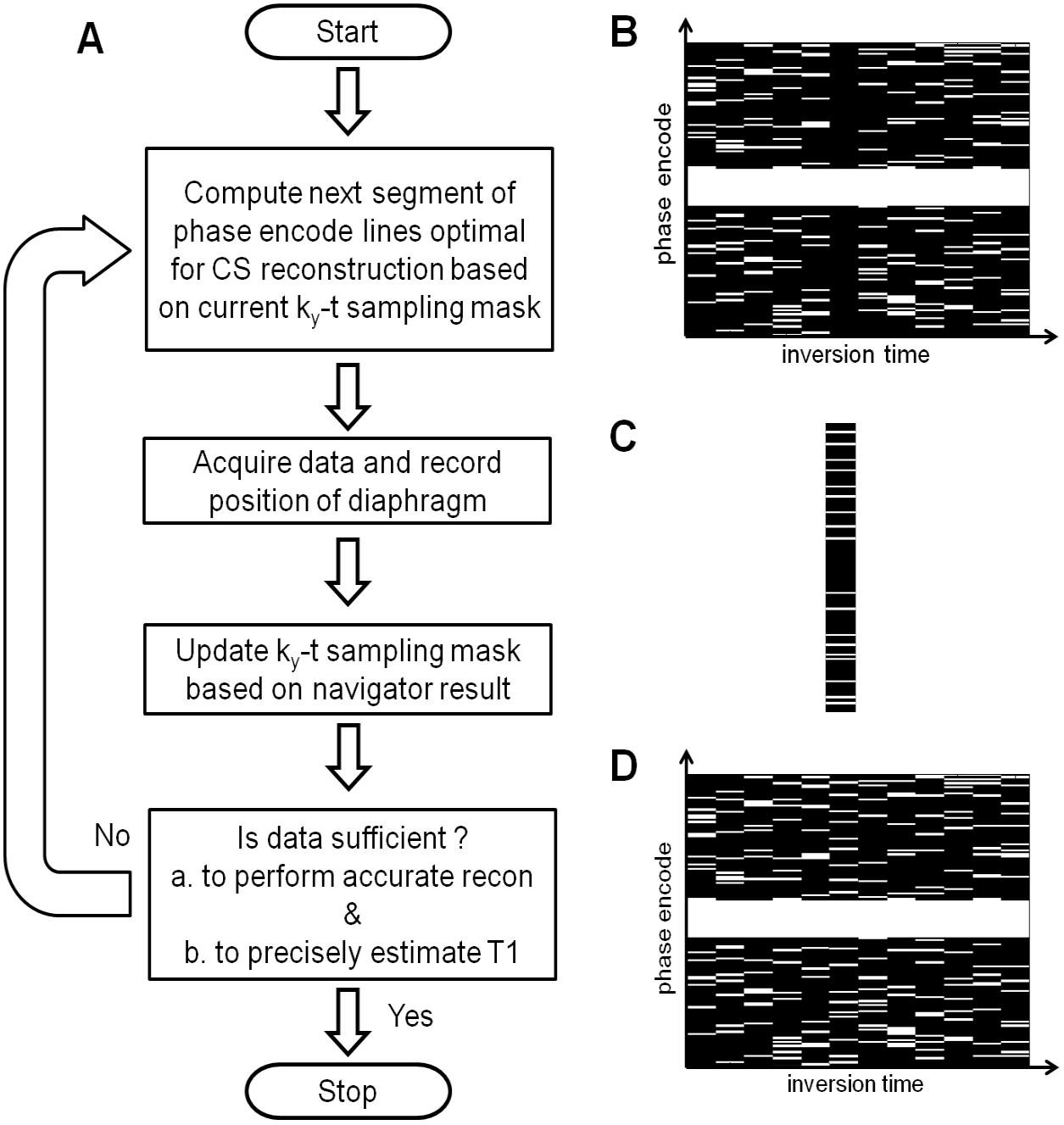

Figure 2.2: *The adaptive data acquisition algorithm.* ***A:*** *Flow chart of the algorithm.* ***B:*** *Example sampled k_y-t space. A white line represents an acquired k_y line and a black line represents a k_y line which has not been acquired.* ***C:*** *Example set of k_y lines adaptively computed for the next acquisition.* ***D:*** *Example updated k_y-t data space, which is a*

combination of k_y-t space in B and C. Each iteration of the acquisition algorithm begins by computing optimal phase encode lines suitable for CS reconstruction (example in C), based on the previously sampled data in k_y -t space (example in B). Data are acquired at the computed phase encode indices, and the diaphragm position is recorded. The acquisition is stopped if the sampled data in k_y -t space are navigator-accepted and sufficient to perform accurate CS reconstruction and to precisely estimate T1. Otherwise, the iteration is continued.

segment of phase encoding lines to acquire by determining which lines have been acquired least often over all of the inversion times (i.e., using a probability density function, or PDF). Using computer simulations, the adaptive selection strategy was compared to a nonadaptive strategy. For the nonadaptive scheme, phase encode lines were chosen based on a pre-determined acquisition order, where the lines were independently selected for each time-point. Specifically, for each time-point the center fully sampled phase encode lines were acquired initially while the outer phase encode lines were acquired later in a uniform random fashion, independent of other inversion times.

For selection of the TSPR threshold value, fully sampled datasets were retrospectively undersampled at various acceleration rates, and the corresponding reconstructed images were qualitatively evaluated. TSPR was computed for all these undersampled datasets, and a TSPR threshold value that distinguished images without artifact from those with artifact was selected. For selection of the CRLB threshold, we determined that the CRLB was $665ms^2$ when all 12 inversion times are used, which provides a T1 precision of 25.8ms. A 20% reduction in precision provides a CRLB value

of 957ms^2. Additionally, simulations of the adaptive acquisition were performed using physiological information (ECG and respiratory data) from volunteer scans. In these simulations, acquisition times were computed for different CRLB threshold values while keeping the TSPR threshold constant. We observed that the scan time increased substantially when the CRLB threshold value was reduced to lower than 950ms^2. Based on these two results we chose the CRLB threshold to be 950ms^2.

2.3.3 Image Reconstruction and post processing

The proposed ANGIE method acquires a sequence of images of tissue undergoing T1 relaxation. Also, in general terms, the MR images are spatially smooth. Therefore, ANGIE images possess spatiotemporal sparsity. Accordingly, we used CS with matrix rank as the sparse domain(67). Furthermore, we used CS in conjunction with SENSE(58) parallel imaging to reconstruct ANGIE images. The reconstruction problem was formulated as the following optimization equation:

$$\mathbf{m}^* = \arg\min_{\mathbf{m}} \|\mathcal{F}_u C_i \mathbf{m} - \mathbf{d}\|_2 + \lambda \|\mathbf{m}\|_* \qquad [2.3]$$

where **m** is the image after coil combination, C_i is the individual coil sensitivity profile, **d** is the measured k-space data, and $\| \quad \|_*$ is the nuclear norm operator. Unaliased low resolution images were obtained using the central fully-sampled region of k-space, and sensitivity maps were calculated from the low resolution images based on an eigenvector filter approach(68). The regularization parameter, λ, was empirically determined to minimize the mean squared error (MSE) using retrospective undersampling of fully sampled datasets and an acceleration of rate 4. The optimal values of λ ranged from $2*10^{-5}$ to $5*10^{-5}$ (leading to similar MSE values). More

regularization was needed when SNR was lower. Thus, datasets with in-plane resolution higher than or equal to 1.2x1.2mm^2 were reconstructed using $\lambda = 5*10^{-5}$, while datasets with in-plane resolution lower than 1.2x1.2mm^2 were reconstructed using $\lambda = 2*10^{-5}$.

The raw time-stamped k-space data were exported from the scanner to perform reconstruction offline. Each readout segment was binned to the nearest TI based on it's timestamp. The inversion time of the segment with the fully-sampled central k-space region was used as the inversion time of the entire bin. After binning, the data were reconstructed using a variable splitting algorithm with continuation(67) modified to incorporate parallel imaging. The reconstruction algorithm provided the complex coil-combined images. These individual images were phase corrected using the phase of the image with the longest TI(69), and the phase-corrected images were used to generate the T1 maps. A three parameter exponential model was used for T1 estimation using a Levenberg-Marquardt algorithm.

2.3.4 Computer simulations for sampling scheme

To compare the performance of the adaptive and nonadaptive sampling schemes, we used computer simulations based on retrospective undersampling of a fully-sampled ANGIE dataset. The simulations were performed using ECG and respiratory signals acquired from different volunteers. Undersampling was performed by assuming the same navigator acceptance pattern for both the schemes (nonadaptive and adaptive) so that the same total number of phase encodes were acquired for each scheme. The simulated acquisition was stopped for both schemes when the CRLB and the TSPR

values, calculated from the k_y-t sampling pattern of the adaptive scheme, were below the threshold values. This ensured that the simulated acquisition time was equivalent for both sampling schemes. Since the same physiological signals as well as the same acquisition time were used to simulate both data sampling methods, the same number of phase encode lines were accepted for each time frame for both sampling schemes. Therefore, only the phase encode indices varied from one scheme to the other. To consider variations in physiological signals, 9 simulations were performed, each with a different set of physiological signals. Images were reconstructed and quantitatively evaluated using the mean squared error (MSE) and structure similarity (SSIM). MSE measures the direct difference between the two images, while SSIM is a more comprehensive measurement of the similarity between two images which includes measurement of the structure, intensity and contrast, and it represents human perception more closely(70).

2.3.5 Phantom study

Twelve agarose gel phantoms containing millimolar concentrations of copper sulphate(71,72), with T1 values ranging from 200ms to 1500ms and T2 values near 50ms or 200ms, were used to validate T1 estimates made using ANGIE. The phantoms were scanned at heart rates ranging from 40 bpm to 100 bpm. Additionally, phantoms were scanned with an arrhythmic ECG signal generated using an ECG simulator (750100 Rev B Simulator, SA Instruments, Stony Brook, NY). The simulated arrhythmic ECG signal had heart rate ranging from 40 to 110 bpm with a mean and standard deviation of 74.5 bpm and 20.4 bpm, respectively. ANGIE acquisition parameters included: matrix size = 208x144, pixel size = 1.4x1.4 mm^2, slice thickness = 8mm, initial

TI = 190ms, TI increment = 80ms, TSPR threshold = 0.5, and CRLB threshold = 950ms^2. The navigator was placed in a background region to randomly accept/reject the data. T1 estimates were computed from CS-reconstructed images. A single point inversion-recovery spin-echo sequence with twenty TI values ranging from 50-5500ms was used to measure reference T1 values of the phantoms.

2.3.6 Volunteer studies for T1 mapping of the left ventricle

All studies were performed using a 1.5T MR scanner (Avanto, Siemens, Erlangen, Germany) in accordance with protocols approved by our institutional review board. To compare ANGIE to MOLLI, we performed acquisitions using standard MOLLI(47), ANGIE with resolution similar to MOLLI, and high resolution ANGIE in 6 healthy volunteers (age 28 ± 3 yrs). For each subject a mid-ventricular short-axis slice was imaged during late diastole. Relevant imaging parameters for MOLLI were repetition time (TR) = 2.4ms, echo time (TE) =1.0 ms, field of view (FOV) read = 285-430mm, FOV phase = 69.8%, matrix size = 192x108, pixel size = 1.5-2.2x1.8-2.8 mm^2, flip angle = 35^0, slice thickness = 8mm, acquisition window = 155ms, initial TI = 100ms, and TI increment = 80ms. Relevant parameters for high-resolution ANGIE were TR = 3.2ms, TE = 1.6ms, FOV read = 285-430mm, FOV phase = 69.2%, matrix size = 304x216, pixel size = 0.9-1.4x0.9-1.4 mm^2, flip angle = 35^0, slice thickness = 8mm, acquisition window = 115ms, initial TI = 200ms, TI increment = 80ms, phase encodes per readout = 36, navigator acceptance window = ± 3 mm, TSPR threshold = 0.5, and CRLB threshold = 950ms^2. The initial TI for ANGIE was higher than for MOLLI because ANGIE contained a navigator module and a fat saturation module prior to the readout module, which were not present in MOLLI. Furthermore, MOLLI uses partial Fourier along the

phase encode and readout directions. Partial Fourier along the phase encode direction allows fewer repetitions before the center of k-space is acquired, while partial Fourier along the readout direction allows a lower TR value, thus reducing the initial TI. For low-resolution ANGIE the matrix size was changed to 208x144, which yielded a pixel size of 1.4-2.1x1.4-2.1mm^2. Since MOLLI is a breath-held technique while ANGIE is a free-breathing technique, there will often be a mismatch of anatomical slice location. For this reason, MOLLI was acquired at several different slice locations and the closest anatomical slice was used for comparison. T1 maps were generated and contours were drawn to compute LV myocardial T1 and blood-pool T1.

2.3.7 Volunteer studies for T1 mapping of the right ventricle

To evaluate ANGIE for assessment of the T1 of the RV wall, which is 3-5mm thick in healthy adults(73), we utilized a high-resolution protocol. For comparison, we also performed acquisitions using standard MOLLI(47). Nine healthy volunteers (age 28 ± 5 yrs) underwent MRI of a short-axis slice. The image acquisition was timed to occur at end systole to take advantage of the thicker RV wall and greater separation of the RV wall from the liver and the chest wall(74). Relevant imaging parameters for MOLLI were TR = 2.6ms, TE =1.16 ms, FOV read = 390-440mm, FOV phase = 68.8%, matrix size = 192x106, pixel size = 2.0-2.3x2.5-2.9 mm^2, flip angle = 35^0, slice thickness = 4mm, acquisition window = 164ms, initial TI = 100ms, and TI increment = 80ms. Relevant parameters for high-resolution ANGIE were TR = 3.2ms, TE = 1.6ms, FOV read = 270-315mm, FOV phase = 100%, matrix size = 224x224, pixel size = 1.2-1.3x1.2-1.3 mm^2, flip angle = 35^0, slice thickness = 4mm, acquisition window = 76ms, initial TI = 160ms, TI increment = 80ms, phase encodes per readout = 24, navigator acceptance window =

± 3 mm, TSPR threshold = 0.25, and CRLB threshold = 950ms^2. A slice thickness of 4 mm was used to reduce through-plane partial volume effects, which also reduces the SNR. Hence, a lower TSPR threshold value was used as compared to the TSPR threshold value used for the LV acquisition.T1 maps were generated from the reconstructed images and RV contours were drawn using magnitude images (not T1 maps) to compute RV myocardial T1. The contours were drawn in a conservative manner to exclude trabeculations and were forced to have continuous coverage from the anterior RV insertion point to the inferior RV insertion point. A quantitative comparison of image sharpness between ANGIE and MOLLI was performed using the average edge width sharpness metric(75). This sharpness metric computes the mean of the edge width over all the edges in the image detected after applying a Sobel filter(75). The metric measurement was confined to a rectangular region covering only the heart to avoid biases from other regions.

2.3.8 Inter-observer and intra-observer variability

For the assessment of the inter-observer variability, two observers independently analyzed the data for estimation of the myocardial T1 values. Specifically, both the observers manually drew contours delineating the LV wall and the RV wall as described in section 2.3.7. Additionally, both observers repeated the analysis for evaluation of intra-observer variability. The intraclass correlation coefficient(76) (ICC) and the coefficient of repeatability(77) (CR) were computed to compare the T1 repeatability between and within observers. The ICC is a statistical metric to assess the consistency or homogeneity between the techniques(76). Its value ranges from 0 to 1, with 0 being completely inconsistent and 1 being completely consistent measurements. The CR

represents the 95% confidence interval of the difference between the two techniques and is calculated using following equation(77).

$$CR = 1.98 \times \sqrt{\frac{\sum(t_1 - t_2)^2}{n-1}} \quad [2.4]$$

where t_1 and t_2 represent measurements made using each technique.

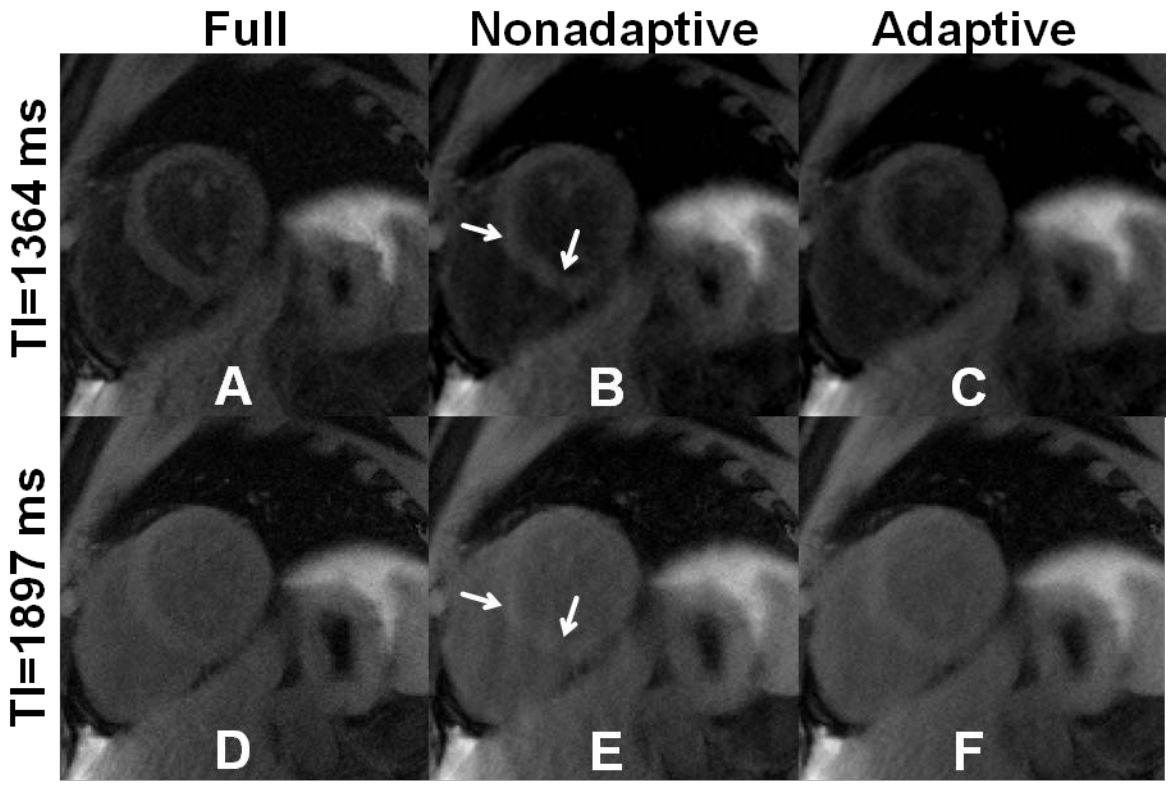

Figure 2.3: *Comparison of ANGIE images acquired using two different undersampling schemes, adaptive and nonadaptive. (A,D): Fully sampled images. (B,E): Images reconstructed from data using a nonadaptive scheme, and (C,F): Images reconstructed from data using an adaptive scheme. Images C and F have reduced aliasing artifacts compared to B and E (arrows), demonstrating that adaptive sampling performs better than nonadaptive sampling.*

2.4 RESULTS:

2.4.1 Computer simulations to compare sampling schemes

Figure 2.3 shows example results from simulations comparing the adaptive and the nonadaptive acquisition schemes. Specifically, example CS-reconstructed images at two inversion times, generated from identical fully-sampled raw datasets retrospectively undersampled using the nonadaptive and the adaptive schemes are shown in Figure 2.3B, E and Figure 2.3C, F, respectively. Fully-sampled reference images are shown in the first column (Figure 2.3A, D). Visual inspection shows that the results generated

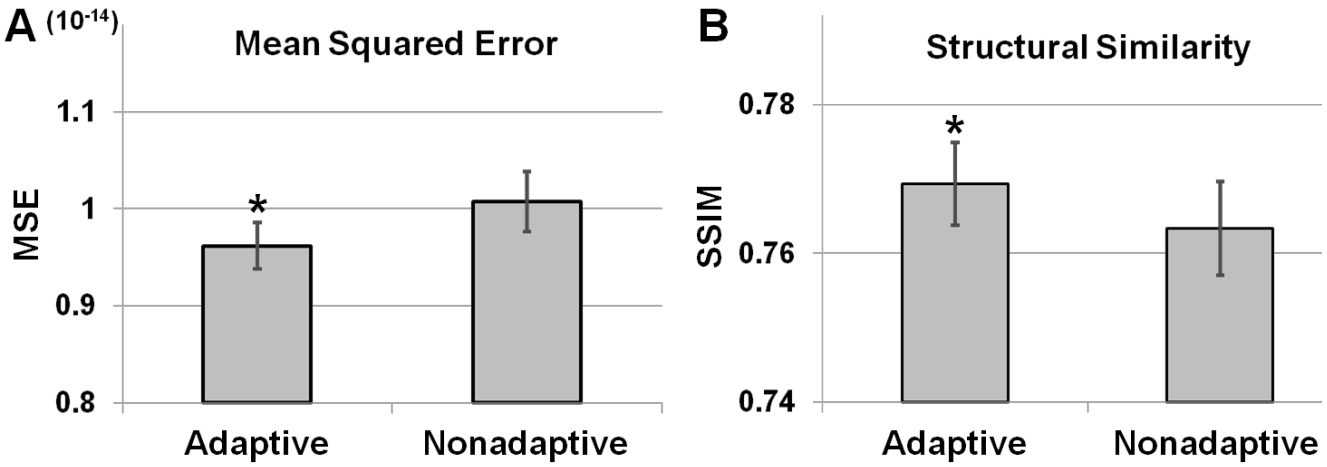

Figure 2.4: *Quantitative analysis of two sampling schemes, adaptive and nonadaptive. Mean squared error (mean ± standard error) (A) and structural similarity (mean ± standard error) (B), averaged over time, of the CS-reconstructed images compared to the fully-sampled reference images. Results show that the adaptive method achieved a lower MSE and higher SSIM compared to the nonadaptive method. (* p<0.05 v.s. nonadaptive).*

using the adaptive scheme most closely resemble the fully-sampled images. Results using the nonadaptive scheme showed residual aliasing artifacts. A quantitative comparison of the sampling schemes from nine sets of simulations, each using different physiological signals, evaluated MSE and SSIM, and the results are shown in Figure 2.4. SSIM and MSE from the adaptive scheme were significantly better than the nonadaptive scheme ($p<0.05$).

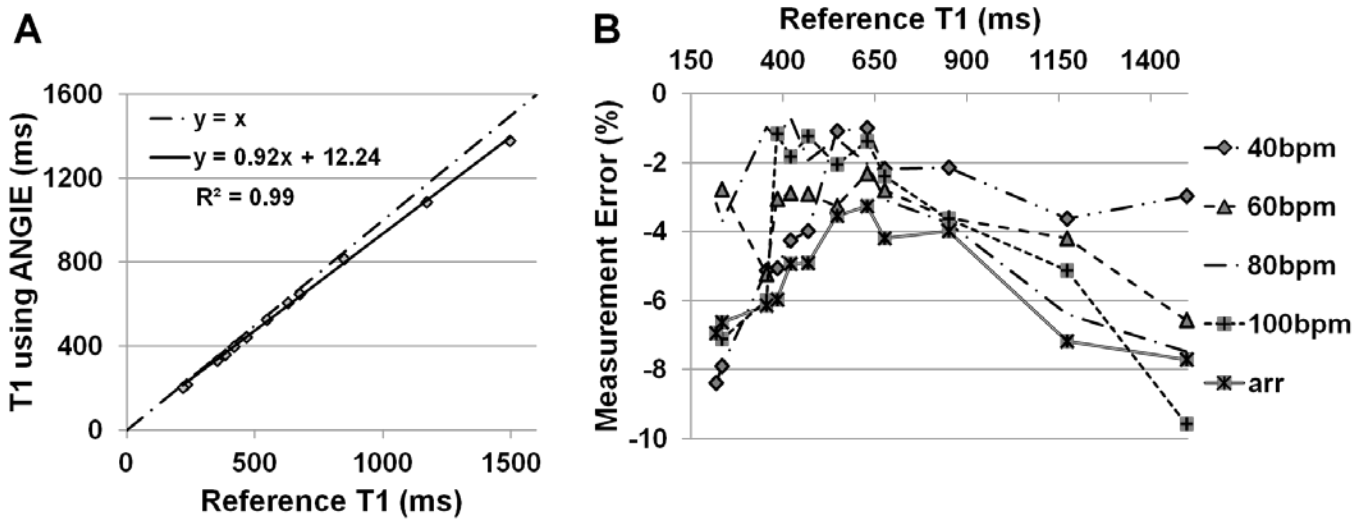

Figure 2.5: *Phantom results.* ***A:*** *Using a simulated arrhythmic ECG, a good correlation of T1 estimates is achieved comparing ANGIE to the reference inversion-recovery spin echo method.* ***B:*** *Percentage error in T1 estimates using ANGIE, as compared to the IR spin echo reference method, for twelve phantoms at five different simulated ECG patterns.*

2.4.2 Phantom study

The T1 estimates obtained using ANGIE imaging of phantoms were related to reference T1 values with a slope of 0.92 ± 0.03 and a bias of 22 ± 16ms over all the simulated

ECG patterns, using a linear model ($T1_{ANGIE}$ = slope*$T1_{ref}$+bias). Figure 2.5A displays the correlation between ANGIE T1 estimates using a simulated ECG signal with an irregular heart rate and reference T1 estimates. Figure 2.5B displays the percentage error in measuring T1 using ANGIE for all twelve phantoms at five different ECG patterns, including a simulated irregular heart rate. The maximum error under these conditions was less than 10%.

2.4.3 Volunteer studies for T1 mapping of the left ventricle

Example T1 maps acquired from a healthy volunteer are shown in Figure 2.6. Figure 2.6A, 2.6B and 2.6C are T1 maps generated from high-resolution ANGIE, low-resolution

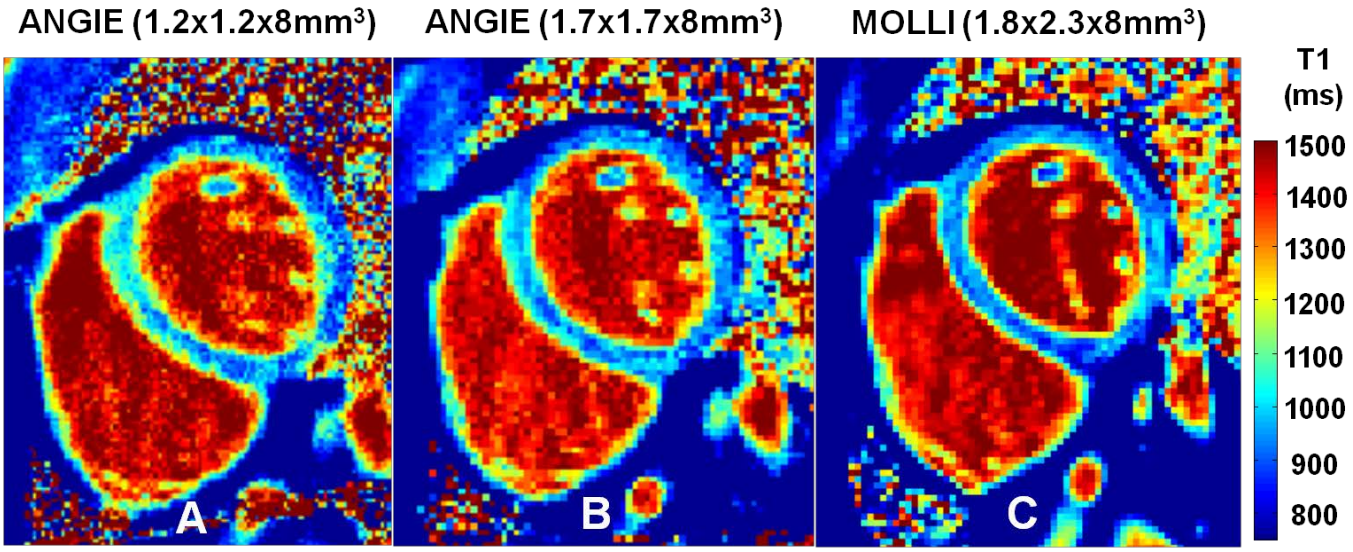

Figure 2.6: *Example T1 maps acquired from a healthy volunteer for left ventricular wall imaging.* ***A****: T1 map using high-resolution ANGIE (1.2x1.2x8 mm³),* ***B****: T1 map using lower-resolution ANGIE (1.7x1.7x8 mm³), and* ***C****: T1 map using MOLLI (1.8x2.3x8 mm³). The ANGIE T1 maps are in good agreement with the MOLLI T1 map in this healthy volunteer.*

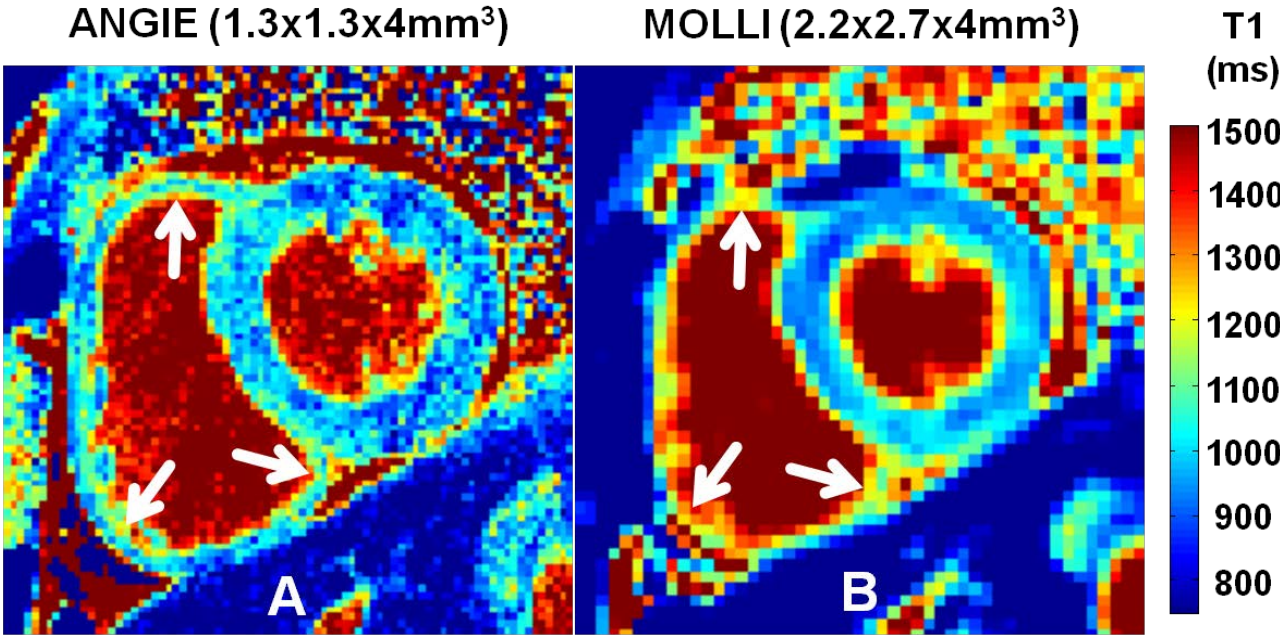

Figure 2.7: *Example T1 maps acquired from a healthy volunteer for right-ventricular wall imaging.* ***A****: High-resolution ANGIE (1.3x1.3x4 mm³), and* ***B****: lower-resolution MOLLI (2.2x2.7x4 mm³). The T1 maps illustrate the ability of ANGIE to achieve high resolution and resolve (arrows) the right-ventricular wall compared to MOLLI.*

ANGIE, and MOLLI, respectively. All three T1 maps appear similar and contain T1 estimates which are in good agreement with the literature(78-80). Because the slice thickness is 8 mm for all of these T1 maps, through-plane partial volume effects obscure the ability of ANGIE to demonstrate sharper edges using this protocol. Its benefits are readily appreciated below where a 4 mm slice thickness was used for the RV protocol. Nonetheless, Table 2.1 summarizes the T1 values of the LV myocardium and the blood, the scan time, the acceleration rate and the navigator efficiency. The variations in blood T1 values among the three acquisitions are within 6% (p=NS), which is in agreement

with our phantom results and our estimated errors given the effects of variations in heart rate. The mean scan time for high-resolution ANGIE T1 mapping from six volunteers was 70 ± 37s per slice with a navigator efficiency of 59 ± 23%.

Table 2.1. Scan time and T1 mapping results from healthy volunteers for LV wall imaging.

	MOLLI	**Adaptive ANGIE (high res)**	**Adaptive ANGIE (low res)**
Scan Time	17 (hb)	70 ± 37 s	41 ± 15 s
Myocardial T1 (ms)	975 ± 100	979 ± 82	954 ± 71
Blood T1 (ms)	1459 ± 59	1419 ± 73	1376 ± 54
Accel. Rate	1.7 (Parallel)	3.2 ± 0.4 (CS)	3.3 ± 0.8 (CS)
Navigator Efficiency (%)	-	59 ± 23	59 ± 17

2.4.4 Volunteer studies for T1 mapping of the right ventricle

Example T1 maps acquired using the RV protocol from a healthy volunteer are shown in Figure 2.7. Specifically, Figure 2.7A and 2.7B are end-systolic T1 maps generated from high-resolution ANGIE and lower-resolution MOLLI datasets respectively. The RV wall is better delineated (arrows) in ANGIE compared to MOLLI due to its higher spatial resolution and shorter acquisition window. Table 2.2 summarizes the scan time, the T1 values of both LV and RV myocardium, the acceleration rate and the navigator efficiency. Figure 2.8 shows the results from quantitative comparisons of ANGIE and MOLLI. In particular, Figures 2.8A and 2.8B show box and whisker plots comparing the mean and standard deviation of T1 estimates of pixels within the RV wall contour, respectively, for ANGIE and MOLLI. ANGIE provided significantly lower intrascan variation in the RV T1 estimate compared to MOLLI ($p<0.05$). Figure 2.8C shows a bar

chart comparing the average edge width between MOLLI and ANGIE, which was significantly lower for ANGIE ($p<0.01$).

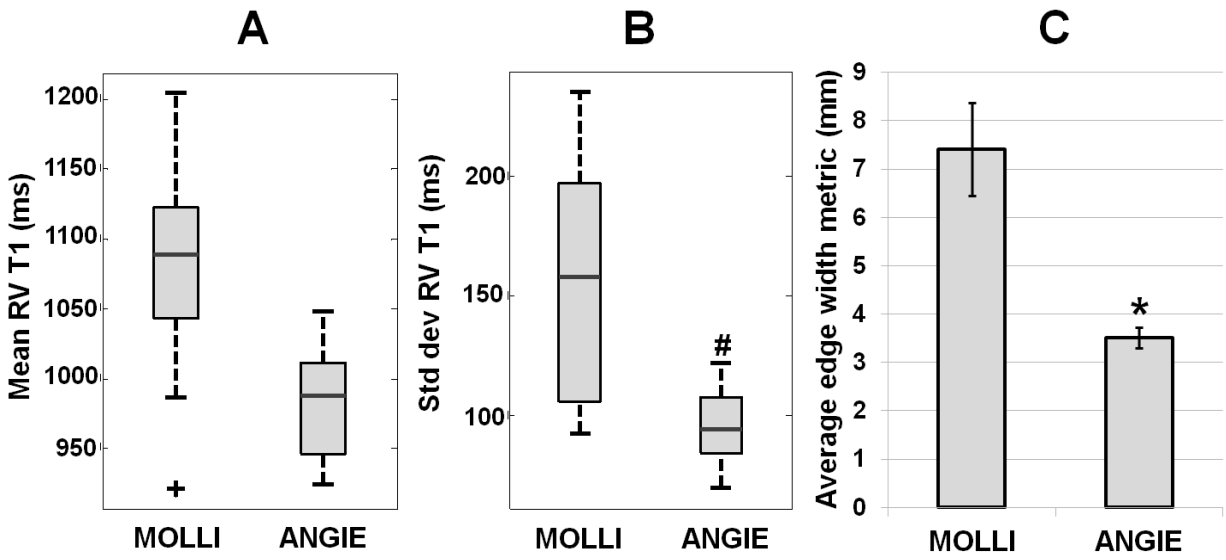

Figure 2.8: *Quantitative comparison between high-resolution ANGIE and lower-resolution MOLLI in nine healthy volunteers from the RV wall imaging study.* ***A:*** *Box plot comparing mean T1 estimates of pixels within the RV contours.* ***B:*** *Box plot comparing the standard deviations of T1 estimates of pixels within the RV contours.* ***C:*** *Bar chart comparing the average edge width, an image sharpness metric, for MOLLI and ANGIE. (B) ANGIE showed lower intrascan variation in the RV T1 estimates compared to MOLLI (# $p<0.05$ v.s. MOLLI). (C) The average edge width of ANGIE was significantly smaller compared to MOLLI (*$p<0.01$ vs MOLLI). Note: The '+' sign in the panel A is an outlier.*

Table 2.2. Scan time and T1 estimates from healthy volunteers for RV wall imaging.

	MOLLI	ANGIE
Scan Time	17 (hb)	157 ± 53 s
Left ventricular wall T1 (ms)	974 ± 58	942 ± 90
Right ventricular wall T1 (ms)	1076 ± 157	980 ± 96
Accel. Rate	1.7 (Parallel)	2 ± 0.1 (CS)
Navigator Efficiency (%)	-	59 ± 18

2.4.5 Inter-observer and intra-observer variability

The ICC for inter-observer variability was 0.927 for the RV myocardial T1 and 0.893 for the LV myocardial T1. The CR for inter-observer variability, expressed as a percentage of the mean, was 3.00% for the RV myocardial T1 and 2.92% for the LV myocardial T1. The ICC for intra-observer variability was 0.931 for the RV myocardial T1 and 0.932 for the LV myocardial T1. The CR for intra-observer variability was 2.87% for the RV myocardial T1 and 2.02% for the LV myocardial T1. T1 estimation with ANGIE for both the LV and RV myocardium shows good inter-observer and intra-observer agreement.

2.5 DISCUSSION:

We developed an improved method, ANGIE, to perform high-resolution cardiac T1 mapping within a clinically reasonable scan time. ANGIE makes use of a segmented readout strategy, navigator gating, adaptive data undersampling, and parallel-CS image reconstruction. The accuracy of cardiac T1 estimation using ANGIE was evaluated by performing comparisons with MOLLI in phantoms and healthy volunteers. The use of high-resolution ANGIE T1 mapping for assessment of thin structures such as the RV wall was demonstrated in healthy volunteers.

In this study we developed an acquisition algorithm that adapts to the navigator rejection of data by recalculating, in real-time, a sampling pattern that is well-suited for CS image reconstruction. We also developed stopping criteria to halt data acquisition when the k_y-t sampling is sufficient for an accurate CS reconstruction and a precise T1 estimation. The adaptive acquisition was crucial in reducing the scan time. Specifically, the scan time for adaptive low-resolution ANGIE was 41±15s with a navigator efficiency of 59±17%, while for nonadaptive low-resolution ANGIE the scan time was 81±28s with a navigator efficiency of 45±15%(81), illustrating an improvement of 49% in acquisition time due to the adaptive method . Generally, in CS the acquisition is stopped based on the acceleration rate. For ANGIE, if a simple stopping criterion based on the acceleration rate is used, it may lead to undesirable k_y-t sampling patterns or long acquisition times. Using the CRLB ensures that the acquisition is only long enough to sample time points crucial to meet a specific precision for the T1 estimate, and using the TSPR ensures that the data for the sampled time points is sufficient to perform high-quality reconstruction. The selection of the phase encode lines using the adaptive acquisition scheme provided better image quality for the same amount of data, minimizing the scan time needed to achieve good image quality.

In the adaptive acquisition algorithm, the selection of phase encode lines was performed based on a PDF metric. It is possible that selection of the phase encode lines based on a TSPR metric may provide even better results. However, optimal selection of phase encode lines based on a TSPR metric would require minimization of the TSPR over all possible combinations of unacquired phase encode lines. Depending on the number of phase encode lines per segment and the number of unacquired phase

encode lines, the set of possible combinations can contain a large number of elements, and minimizing TSPR over this large set is computationally intensive. Thus, with our current hardware, real-time selection of phase encode lines based on a TSPR metric is not feasible. For this reason, our selection of phase encode lines was based on a PDF metric.

Most of the recently published cardiac T1 mapping techniques(47,48,82-84) make use of a single shot readout, limiting spatial resolution due to the small acquisition window imposed by cardiac motion. ANGIE uses a segmented readout, which enables higher spatial resolution. However, using a segmented readout might raise the concern that ANGIE T1 estimates may be more sensitive to variations in heart rate. By design, ANGIE uses a variable density sampling scheme where the fully-sampled central k-space region, which primarily determines image contrast, is acquired in a single readout segment for each TI. Furthermore, the time stamp of the central portion of k-space defines the inversion time for each image. Employing this methodology, our phantom study demonstrated the accuracy of ANGIE T1 estimation with different simulated ECG patterns, including an arrhythmic pattern, and the volunteer study showed in vivo agreement of the ANGIE T1 estimates with MOLLI and prior literature(78-80). We observed that our phantom results showed greater errors for phantoms with longer T1 values. This is primarily attributed to the use of only two recovery heartbeats. These errors can be substantially reduced by using four recovery heartbeats, which would increase the total scan time by a factor of 1.33. Also, since ANGIE uses a segmented readout and free breathing, it can be extended to perform a 3D acquisition. In that case higher acceleration rates may be feasible due to higher SNR and redundancy along the

third dimension. The development of 3D ANGIE will be investigated in Chapter 4 of this dissertation.

In Figure 2.6, the higher spatial resolution of ANGIE is not readily apparent, even though the in-plane pixel size is smaller. These data were used for assessment of the LV and for comparing ANGIE and MOLLI T1 values. However, due to through-plane partial volume effects resulting from a slice thickness of 8 mm, the images and T1 maps do not clearly demonstrate the benefits of higher in-plane resolution. In contrast, the RV imaging study used a slice thickness of 4mm. The improvement in in-plane spatial resolution is very clear in these datasets, as seen in Figure 2.7, and this benefit was quantified using the average edge width metric.

In Figure 2.7, ANGIE and MOLLI show very different T1 values for mediastinal fat. While MOLLI measures the T1 of fat properly, ANGIE yields very high values for the fat T1. This occurs because the ANGIE scans employed fat suppression to more clearly delineate the borders of the RV wall. With the use of fat suppression, the fat signal is unchanged from one inversion time to the next, resulting in an apparent long T1 for fat. However, ineffective fat suppression, for example due to magnetic field inhomogeneity, yields a low fat T1 estimate as seen in the examples shown in Figure 2.6. Thus, fat-suppressed ANGIE may produce incorrect fat T1 values, which could be problematic in patients with fatty infiltration of the myocardium. However, the use of fat suppression is by no means a requirement for ANGIE.

Assessment of RV fibrosis may be important in diseases such as arrhythmogenic RV dysplasia(51), congenital heart disease, and pulmonary hypertension. To the best of

our knowledge, the present study is the first report of T1 mapping of the RV wall. We measured an RV wall T1 of 980 ± 96 ms using high-resolution ANGIE imaging, which is similar to typical T1 estimates of the LV wall. A few prior studies have suggested that the RV wall has shorter post-contrast T1 compared to the LV wall based on the inversion time required to null healthy myocardium in LGE MRI(85,86). However, Grosse-Wortmann et al. proposed that the apparent difference in the T1 relaxation of the right and left ventricular walls is due to partial volume effects on the thin RV(74). The T1 value (1076 ± 157ms) of the RV wall that we measured using low-resolution MOLLI trended higher compared to the T1 (974 ± 58ms) of the LV wall. Thus, our observations are consistent with the partial volume effect conjecture proposed by Grosse-Wortmann et al(74) and suggest the RV T1 value measured using high-resolution ANGIE is more accurate compared to low-resolution MOLLI.

For high-resolution T1 mapping of the RV using ANGIE, a conservative degree of acceleration (rate 2) was used. In practice, this acceleration rate was achieved by selecting a particular value for the TSPR threshold. A conservative approach was chosen because the aim was to achieve T1 mapping of the RV, which requires excellent image quality with minimal artifacts. Excellent image quality was demonstrated by good inter-observer (ICC: 0.927; CR: 3.00%) and intra-observer (ICC: 0.931; CR: 2.87%) agreement for RV T1 estimation. Future work will aim to further accelerate the acquisition and reduce scan time.

This study on developing and applying ANGIE has some limitations. First, reconstruction of ANGIE images was performed offline, where reconstruction of high-resolution datasets took approximately 13.25 minutes on a standard desktop PC

(3.4GHz Intel(R)i7 CPU with 12GB RAM). Improving the speed of reconstruction is currently an active area of research. Second, ANGIE has a relatively long scan time compared to existing techniques. A third limitation of this study is that the ANGIE protocol used fat suppression while the MOLLI protocol did not. This difference may have affected both the visualization and edge sharpness comparisons between the two techniques. Although ANGIE has these limitations, its capability to perform high-resolution T1 mapping may open up new avenues of investigation by allowing myocardial fibrosis measurements in thin structures.

In summary, we developed the ANGIE method that can acquire high spatial resolution (~1.1x1.1mm^2) cardiac T1 maps within a clinically acceptable scan time by applying navigator gating, compressed sensing and an adaptive acquisition algorithm to a segmented inversion recovery Look-Locker sequence. As a result, ANGIE opens the prospect of performing a quantitative assessment of thin structures such as the RV wall and, possibly in the future, the left-atrial walls and subtle features of the peri-infarct zone.

Chapter 3

Application of high resolution T1 mapping in patients with pulmonary arterial hypertension (PAH)

3.1 INTRODUCTION

Pulmonary arterial hypertension (PAH) is a progressive and debilitating disease with high morbidity and mortality(29,31,32) characterized by increased pulmonary vascular resistance due to the presence of pulmonary vasculopathy(33-35). The ability of the right ventricle (RV) to adapt to this afterload is the key determinant of a patient's symptoms and survival, and ultimately RV failure is the main cause of death in patients with PAH(38). Mortality in PAH correlates directly with the development of right heart failure(37,53). Thus, measurements that gauge RV health provide the best potential to assess the severity of PAH(38). One of the primary goals of the therapy for PAH is to protect the right heart(87). Current assessment of RV performance is based on echocardiographic and right heart catheterization data, but these techniques have significant drawbacks(50): right heart catheterization is an invasive procedure, and measurements performed using echocardiography are less accurate due to factors such as use of geometrical approximations, operator dependence and patient-dependent

echo window. MRI, a noninvasive and versatile imaging modality, has the potential to offer a more complete assessment of the RV in PAH(34,49,50,88).

Pressure overload conditions in PAH lead to progressive RV hypertrophy, systolic dysfunction, RV dilation, RV diastolic dysfunction and tricuspid regurgitation(36) , resulting in a complex series of changes in cardiomyocytes and their extracellular matrix(35,37). The extent of focal fibrosis at the septal RV insertion sites, measured using late gadolinium enhancement (LGE) MRI, has been shown to positively correlate with an increase in afterload and inversely correlate with RV performance in patients with PAH(49,50). Thus, quantitative measurement of changes in RV extracellular space may present a valuable prognostic marker of the health of the RV in patients with PAH.

As described in Chapter 1, gadolinium-enhanced T1 mapping MRI has emerged as a valuable tool for evaluation of various cardiovascular diseases presenting changes in myocardial extracellular volume fraction (ECV) (10,27,39-41). By performing T1 mapping before and after injection of gadolinium-based contrast agent, the myocardial ECV value can be estimated, which has been shown to correlate with diffuse myocardial fibrosis(27,39). However, current clinically-preferred T1 mapping techniques such as MOLLI(47) have limited spatial resolution, restricting their application to assessment of the LV ECV. As detailed in Chapter 2 of this dissertation, we recently developed a novel T1 mapping technique, ANGIE(89), which provides high-resolution T1 mapping for assessment of thin structures such as the wall of the RV.

The aim of the present study was to use ANGIE to test the hypothesis that RV ECV is elevated in patients with PAH compared to reference subjects. Furthermore, the

association between the degree of RV fibrosis in PAH, as measured by RV ECV, with RV pressure overload, RV systolic function, and RV dilation was also evaluated.

3.2 METHODS

3.2.1 Population

Twenty-two patients were recruited to undergo cardiac magnetic resonance imaging (CMR) with gadolinium based contrast agent. The study population was sub-divided into two groups of subjects. Group 1 consisted of patients diagnosed with pulmonary arterial hypertension while group 2 consisted of patients with chronic left ventricular systolic heart failure. Patients were excluded from the study in the following situations:

1) Patient has estimated glomerular filtration rate (GFR) less than 45 cc/min based on a serum creatinine (cr) drawn within 30 days of the MRI study.
2) Patient has acute kidney injury or history of paraproteinemia syndromes such as multiple myeloma.
3) Patient is pregnant.
4) Patient has an implanted pacemaker and/or defibrillator.
5) Patient has cerebral aneurysm clips, cochlear implants, or other metallic implants or prostheses that are contraindications to MRI.
6) Patient has severe claustrophobia or inability to lay flat for the MRI exam.
7) Patient is sensitive/allergic to Gd-DTPA.
8) Patient is unable to provide informed consent.

3.2.2 CMR Protocol

All CMR studies were performed using a 1.5T MRI scanner (Avanto, Siemens, Erlangen, Germany). After peripheral IV access was obtained and ECG leads for gating and monitoring were placed, the patient was positioned in the magnet with a phased array surface coil overlying the chest. The imaging protocol was as follows:

3.2.2.a Localizer

Standard localizers were performed to identify the short and long axes planes.

3.2.2.b Cine steady-state free precession (SSFP)

Steady-state free precession cine images were obtained for estimation of LV and RV volumes, and ejection fraction. The sequence parameters are as follows: TR=2.7 ms, TE=1.3 ms, flip angle=73^0, FOV=300-350 mm, and resolution=1.8 x 1.4mm^2. A stack of 8mm thick short axis images with a 2 mm gap between them were used to cover the LV from apex to base. Three standard long-axis images were also acquired (4-chamber, 2-chamber, and 3-chamber views).

3.2.2.c Pre-contrast ANGIE T1 mapping

A single mid-ventricular short-axis slice was imaged using ANGIE at end systole to take advantage of the thicker RV wall and greater separation of the RV wall from the liver and the chest wall. ANGIE used the following imaging parameters: TR = 3.2ms, TE = 1.6ms, flip angle = 35^0, FOV read= 270-340 mm, FOV phase = 100%, matrix size = 224x224, resolution = 1.2-1.4x1.2-1.4 mm^2, slice thickness = 4mm, acquisition window = 102ms, phase encodes per readout = 32, navigator acceptance window = ± 3 mm,

initial inversion time = 160ms, inversion time increment = 80ms, and number of inversion time points=10-12.

3.2.2.d Contrast injection

A bolus of 0.15 mmol/kg of Gd-DTPA (Magnevist, Bayer Healthcare) was injected using peripheral IV access.

3.2.2.e Late gadolinium enhancement (LGE) imaging

LGE imaging was performed 10 minutes following Gd-DTPA injection at the same locations as described for the cine imaging. A phase sensitive inversion recovery GRE sequence was used with the inversion time set to null normal-appearing myocardium. The acquisition was performed using following sequence parameters: TR = 7.1 ms, TE = 3.4 ms, flip angle = 25^0, FOV = 300 - 340 mm, resolution = 1.8 x 1.3 x 8 mm^3. The image acquisition was timed to occur at end systole for alignment with T1 mapping acquisitions.

3.2.2.f Post-contrast ANGIE T1 mapping

Post-contrast ANGIE T1 mapping acquisitions were performed at 5-minute intervals for 30 minutes following LGE acquisitions. The sequence parameters and slice location was the same as pre-contrast ANGIE T1 mapping acquisition.

3.2.2.g Modified Look-Locker inversion recovery (MOLLI) T1 mapping

MOLLI T1 mapping was performed along with ANGIE, both pre and post-contrast, in 10 out of the 12 PAH patients for validation of ANGIE LV ECV measurements. A shorter variant of MOLLI comprised of two inversion recovery based Look-Locker experiments was used in this study. The shorter variant MOLLI sequence acquired 5 images after an

initial inversion, followed by a 4 heart beat pause; then, it acquired 3 images after a second inversion(90,91). The slice location for the MOLLI images was the same as with ANGIE, and the MOLLI image acquisitions were similarly timed to occur at end systole for direct comparison with ANGIE. Relevant imaging parameters for MOLLI were: TR = 2.7ms, TE =1.16 ms, FOV read = 300-310mm, FOV phase = 100%, matrix size = 192x154, pixel size = 1.6-1.7x1.9-2.1 mm^2, flip angle = 35^0, slice thickness = 4mm, acquisition window = 234ms, initial TI = 100ms, inversion time increment = 80ms, and number of inversion time points=10-12.

3.2.3 CMR data analysis

All image analysis was performed using custom software developed in MATLAB (The Mathworks, Inc., Natick, Massachusetts).

3.2.3.a Image reconstruction for ANGIE

ANGIE image reconstruction, using a compressed sensing with matrix rank sparsity in conjunction with SENSE parallel imaging, was performed as described in Section 2.3.3. The regularization parameter was set to 5*10-5 based on our previous study.

3.2.3.b T1 and ECV estimation

The reconstruction algorithm provided complex coil-combined images. These individual images were phase-corrected using the phase of the image with the longest TI(92), and the phase-corrected images were used to generate the T1 maps. A three-parameter exponential model was used for T1 estimation using a Levenberg-Marquardt algorithm.

$$M_z(t_j) = A + Be^{-t_j/T1^*} + \mathcal{N}(0, \sigma^2) \quad [3.1]$$

where t_j is the j[th] inversion time, T1[*] is the apparent T1, and σ is the noise standard deviation. A Look-Locker correction was applied to estimate T1 from the apparent T1 using the following equation(93): $[T1 = T1^* \cdot (B/A - 1)]$. Manual contours were drawn along the magnitude images in a conservative manner to exclude trabeculations to compute T1 in the RV myocardium, LV blood pool and remote LV myocardium. The remote LV myocardium was determined by the absence of enhancement in LGE image. The myocardial partition coefficient for Gd-DTPA (λ_{Gd}) was computed from the myocardial and the LV blood pool T1 estimates using following equation(27,94,95):

$$\lambda_{Gd} = \frac{Gd\ conc.\ in\ myocardium}{Gd\ conc\ in\ blood.} = \frac{1/T_{1\ myo\ with\ Gd} - 1/T_{1\ myo\ without\ Gd}}{1/T_{1\ blood\ with\ Gd} - 1/T_{1\ blood\ without\ Gd}} \quad [3.2]$$

λ_{Gd} was calculated as the slope of the linear fit of 1/(myocardial T1) vs 1/ (LV blood pool T1) measured at various time points pre- and post-injection of the contrast agent. The myocardial ECV was calculated from λ_{Gd} and the blood hematocrit (Hct) using the following relation(27,94,95).

$$myocardial\ extracellular\ volume\ fraction\ (ECV) = \lambda_{Gd}(1 - Hct) \quad [3.3]$$

3.2.3.c Planimetry analysis

Myocardial borders were manually delineated on SSFP cine images using Argus software (Siemens Medical Solutions, Munich, Germany) to estimate RV and LV volumes and ejection fractions.

3.2.4 Echocardiography based right ventricular systolic pressure (RVSP)

Right ventricular systolic pressure (RVSP) was measured in patients who presented sufficient tricuspid regurgitation on echocardiography. RVSP was determined from peak tricuspid regurgitation jet velocity and right atrial (RA) pressure using a simplified Bernoulli equation(96,97):

$$RVSP = 4\,x\,[peak\ velocity\ of\ tricuspid\ regurgitation]^2 + RA\ pressure \qquad [3.4]$$

Peak velocity of tricuspid regurgitation was measured using continuous-wave Doppler ultrasound of the tricuspid regurgitation jet. RA pressure was estimated from the diameter of the inferior vena cava and the presence or absence of inspiratory collapse.

3.2.5 Propagation of error and uncertainty in measuring ECV due to errors and uncertainties in T1 estimates

As discussed earlier, myocardial fibrosis is assessed by acquiring T1 maps of the heart before and after injection of a gadolinium based contrast agent to estimate the myocardial ECV as follows:

$$ECV_{myo} = (1 - Hct) \cdot \left(\frac{\frac{1}{T1_{myo\ post}} - \frac{1}{T1_{myo\ pre}}}{\frac{1}{T1_{blood\ post}} - \frac{1}{T1_{blood\ pre}}} \right) \qquad [3.5]$$

It is important to understand the error and uncertainty in these ECV measurements. Computer simulations were performed to estimate the propagation of error and uncertainty in ECV due to errors and uncertainties in T1. Throughout the analysis following values were used as the nominal values(98): hematocrit=40%, normal ECV=

25%, native myocardial T1=950ms, native blood T1=1551ms, first post-contrast blood T1=291ms, first post-contrast myocardial T1=451ms, second post-contrast blood T1=343ms and second post-contrast myocardial T1=500ms.

3.2.5.a Analysis of propagation of error for ECV measurement using T1 estimates at two time points

For ECV error propagation analysis using two T1 mapping time points (one pre-contrast and one post-contrast), partial derivatives were applied to equation 3.5. The corresponding closed form solutions are as follows:

$$\frac{\partial ECV_{myo}}{\partial T1_{myo\ pre}} = \left(\frac{1-Hct}{T1_{myo\ pre}{}^2}\right)\cdot\left(\frac{T1_{blood\ post}\cdot T1_{blood\ pre}}{T1_{blood\ pre}\ - T1_{blood\ post}}\right) \quad [3.6]$$

$$\frac{\partial ECV_{myo}}{\partial T1_{myo\ post}} = \left(\frac{1-Hct}{T1_{myo\ post}{}^2}\right)\cdot\left(\frac{T1_{blood\ post}\cdot T1_{blood\ pre}}{T1_{blood\ post}\ - T1_{blood\ pre}}\right) \quad [3.7]$$

$$\frac{\partial ECV_{myo}}{\partial T1_{blood\ pre}} = \left(\frac{(1-Hct)\cdot T1_{blood\ post}{}^2}{T1_{myo\ post}\cdot T1_{myo\ pre}}\right)\cdot\left(\frac{T1_{myo\ post}-T1_{myo\ pre}}{(T1_{blood\ post}\ - T1_{blood\ post})^2}\right) \quad [3.8]$$

$$\frac{\partial ECV_{myo}}{\partial T1_{blood\ post}} = \left(\frac{(1-Hct)\cdot T1_{blood\ pre}{}^2}{T1_{myo\ post}\cdot T1_{myo\ pre}}\right)\cdot\left(\frac{T1_{myo\ pre}-T1_{myo\ post}}{(T1_{blood\ post}\ - T1_{blood\ post})^2}\right) \quad [3.9]$$

3.2.5.b Analysis of propagation of error for ECV measurement using T1 estimates at three time points

For ECV error propagation analysis using three T1 mapping time points (one pre-contrast and two post-contrast), error was added to the nominal value of a single T1 estimate to provide a new set of T1 values. The reciprocal of the new set of T1 values

were fitted to a line to estimate the new ECV value. The error in the new ECV value was measured relative to the nominal reference ECV value. The process was repeated for all six T1 values to estimate the error in ECV due to error in the estimate of the corresponding T1.

3.2.5.c Analysis of propagation of uncertainty for ECV measurement using T1 estimates at two time points

For analysis of propagation of uncertainty in the ECV using two T1 mapping time points (one pre-contrast and one post-contrast), we assumed that the T1 estimates are independent and follow a normal distribution [$\mathcal{N}(\mu,\sigma)$]. It is also assumed that for a given tissue the T1 uncertainty expressed as a percentage of the mean value is the same for pre and post injection of contrast agent. The closed form solution was derived from equation 3.5 using standard rules for variance estimation(99):

$$\sigma^2_{ECV_{myo}} = \mu^2_{ECV_{myo}}\left[\left(\frac{\mu_{T1_{myo\ post}}\cdot\mu_{T1_{myo\ pre}}}{\mu_{T1_{myo\ post}}-\mu_{T1_{myo\ pre}}}\right)^2\cdot\left(\frac{\sigma^2_{T1_{myo\ post}}}{\mu^4_{T1_{myo\ post}}}+\frac{\sigma^2_{T1_{myo\ pre}}}{\mu^4_{T1_{myo\ pre}}}\right)\right.$$
$$\left.+\left(\frac{\mu_{T1_{blood\ post}}\cdot\mu_{T1_{blood\ pre}}}{\mu_{T1_{blood\ post}}-\mu_{T1_{blood\ pre}}}\right)^2\cdot\left(\frac{\sigma^2_{T1_{blood\ post}}}{\mu^4_{T1_{blood\ post}}}+\frac{\sigma^2_{T1_{blood\ pre}}}{\mu^4_{T1_{blood\ pre}}}\right)\right] \qquad [3.10]$$

3.2.5.d Analysis of propagation of uncertainty for ECV measurement using T1 estimates at three time points

Stochastic simulations were performed to estimate the propagation of uncertainty in ECV, measured using three T1 mapping time points (one pre-contrast and two post-contrast), due to uncertainty in T1. The uncertainty in ECV was measured over a range of uncertainties in myocardial (0 to 10%) and blood (0 to 10%) T1. For each combination of uncertainty in myocardial and blood T1, 10,000 sets of T1 values were

generated. Each set contained six T1 values (native myocardial T1, native blood T1, first post-contrast blood T1, first post-contrast myocardial T1, second post-contrast blood T1 and second post-contrast myocardial T1) which are independent of each other and follow a normal distribution [$\mathcal{N}(\mu, \sigma)$] based on the mean and standard deviation of the corresponding tissue and time point. The ECV value for each set of T1 values is estimated by fitting the reciprocal of the T1 values to a line. The standard deviation of the ECV, measured as a percentage of the mean value, over the 10,000 sets of T1 values is considered as the corresponding uncertainty in ECV.

3.2.6 Statistical analysis

All statistical analysis was performed using SigmaPlot 12.5 (Systat Software, Inc., San Jose, California). Continuous variables are expressed as mean ± standard deviation. The distribution of the continuous variables between groups was assessed using Shapiro-Wilk test for normality. Comparisons of continuous variables between groups were performed using Student's unpaired t-test or the Wilcoxon 2-sample test (Mann-Whitney U test), depending on whether or not they followed a normal distribution, respectively. The agreement between ANGIE and MOLLI for measurement of LV ECV was evaluated using Bland-Altman analysis. Correlations of RV ECV with RV systolic pressure, LV ECV, and planimetry based RV and LV function parameters were assessed using Pearson's correlation for linear association.

3.3 RESULTS

Table 3.1. Patient characteristics. (* p<0.05 v.s. LHF)

Patient Characteristics	PAH (N=12)	LHF (N=10)
Age (Yr)	60 (± 15.3)	60 (± 7.0)
Female Sex n (%)	7 (58)	2 (20)
Body Mass Index	26.0 (± 5.9)	28.8 (± 5.1)
LV Ejection Fraction (%)	54 (± 5.5)*	24 (± 8.1)
RV Ejection Fraction (%)	36 (± 7.2)*	47 (± 9.9)
Medical History n (%)		
Hypertension	9(75)	9 (90)
Hyperlipidemia	5 (42)	7 (70)
Diabetes	3 (25)	3 (30)
Atrial fibrillation	1 (8)	3 (30)
Obstructive Sleep Apnea	3 (25)	3 (30)

3.3.1 Study Population

22 patients were enrolled in the study (41% females, 60 ± 12.5 years). The study population was sub-divided into two groups of subjects. Group 1 (12 patients, 58% females, 60 ± 15.3 years) consisted of patients diagnosed with pulmonary arterial hypertension (PAH) while group 2 (10 patients, 20% females, 60 ± 7.0 years) consisted of patients with chronic left ventricular systolic heart failure (LHF) as reference subjects. Patient characteristics for the entire cohort are described in Table 3.1. As mentioned in section 3.2.2.g, additional MOLLI acquisitions were performed for ECV validation in 10

out of the 12 patients from PAH group and 0 out of the 10 patients from LHF group. 4 out of 22 patients (all 4 LHF patients) did not present sufficient tricuspid regurgitation on echocardiography to perform accurate measurement of RVSP. SSFP cine acquisitions were skipped in 1 out of 22 patients (LHF group) due to lack of available imaging time. For the correlation analysis, data from both the groups were used to take advantage of the wider range of the parameter values for better assessment of the association.

3.3.2 Image quality and ECV estimation

Example high-resolution pre- and post-contrast ANGIE T1 maps of the LV and RV acquired from a LHF (a-b) and a PAH (c-d) patient are shown in Figure 3.1. ANGIE T1 maps in both patient groups showed good definition of not only the thick-walled LV but also the thin-walled RV. Figure 3.2 illustrates the estimation of RV (A and C) and LV (B and D) myocardial partition coefficient for Gd-DTPA (λ_{Gd}) from T1 estimates of the corresponding myocardium and LV blood pool. Myocardial ECV was estimated from λ_{Gd} and blood hematocrit using equation 3.3.

3.3.3 ECV measurement results

As shown in Figure 3.3, the ANGIE measurements of LV ECV in PAH patients were in close agreement with MOLLI (mean difference = 0.36%; 95% CI: -1.14 to 1.86%). The agreement of ANGIE with MOLLI validates the accuracy of myocardial ECV measurements using ANGIE T1 mapping. Figure 3.4 summarizes the binary comparison of the ECV measurements between the two groups of patients. The RV

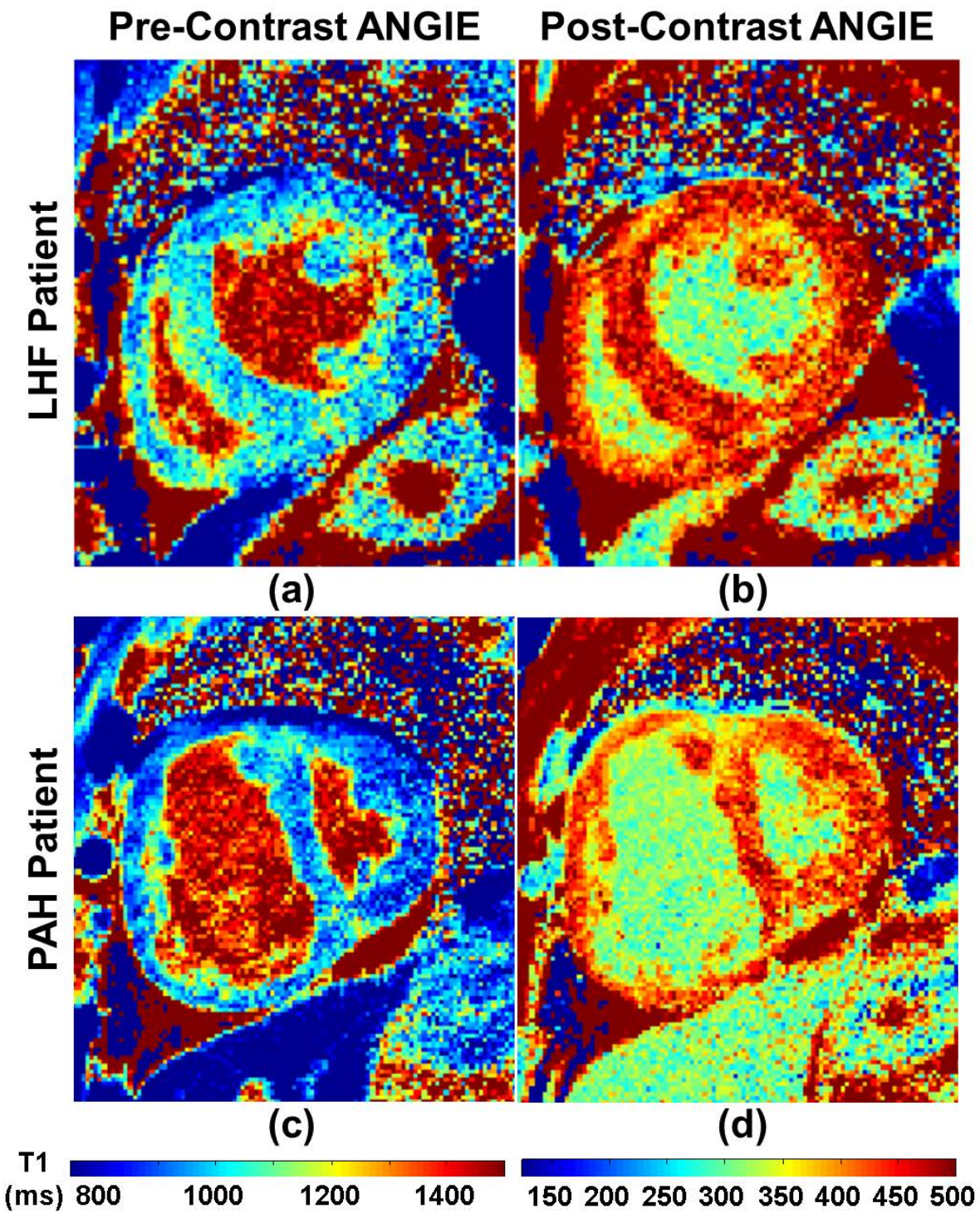

Figure 3.1: *Example ANGIE T1 maps acquired from patients with left-sided heart failure (LHF) (a,b) and pulmonary arterial hypertension (PAH) (c,d). a and c: T1 maps*

prior to injection of gadolinium. b and d: ANGIE T1 maps 25 minutes after injection of gadolinium. The ANGIE T1 maps show good definition of the RV wall.

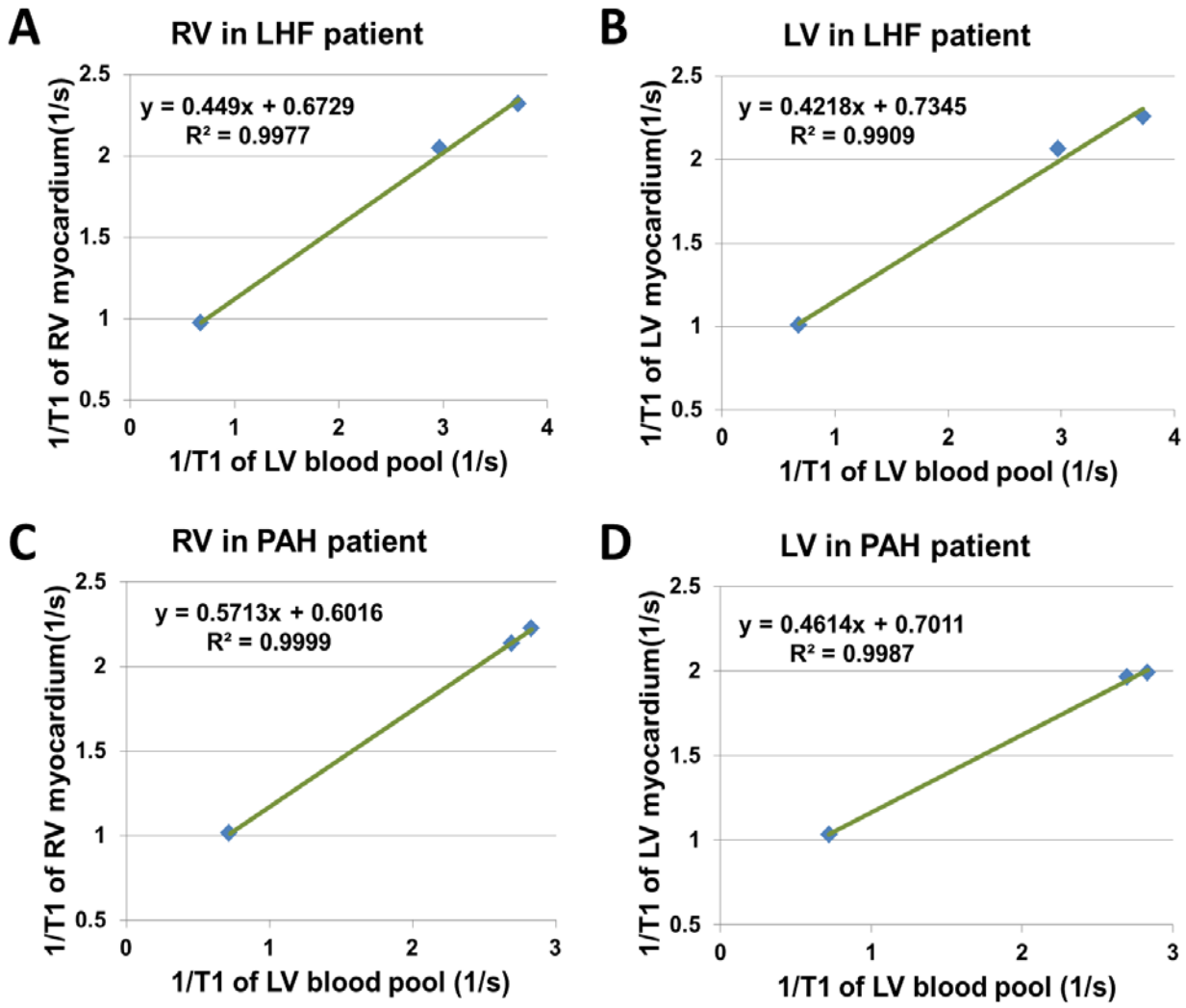

Figure 3.2: *Example results illustrating estimation of myocardial partition coefficient for Gd-DTPA (λ_{Gd}) in patients with left-sided heart failure (LHF) (**A-B**) and pulmonary arterial hypertension (PAH) (**C-D**). **A and C:** RV myocardial results. **B and D:** LV myocardial results. λ_{Gd} is estimated as the slope of the linear fit of 1/(myocardial T1) vs*

1/ (LV blood pool T1) measured at various time points pre- and post-injection of contrast agent.

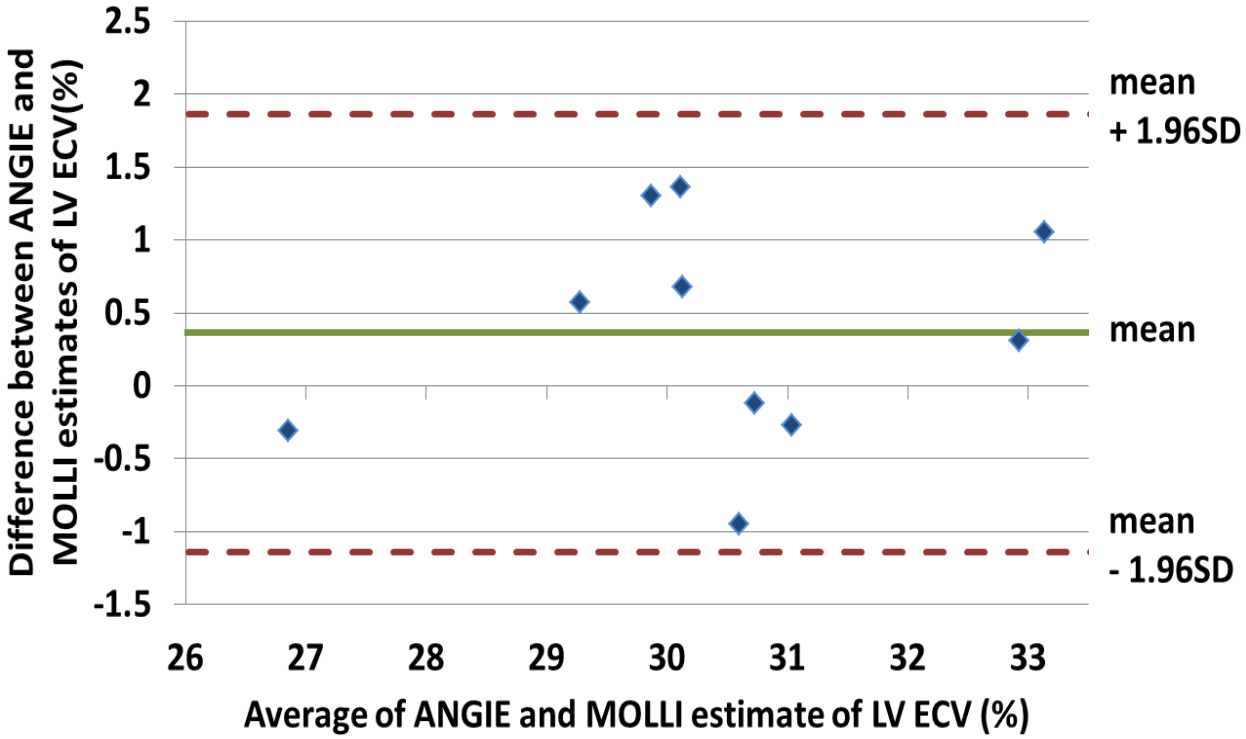

Figure 3.3: *Validation of the accuracy of ECV measurement using ANGIE T1 mapping. Bland-Altman plot comparing LV ECV estimates using ANGIE and MOLLI in patients with PAH. ANGIE measurements of LV ECV (in regions excluding scar on LGE) in PAH patients were in close agreement with MOLLI.*

ECV in PAH patients was significantly greater than the RV ECV in LHF patients ($p<0.01$; difference = 6.08%; 95% CI: 4.27 to 7.89%) (Figure 3.4A). This result supports the hypothesis that the RV ECV is elevated in patients with PAH compared to patients with LHF. Interestingly, the LV ECV in the PAH patient group was also significantly greater than the LV ECV in the LHF patient group ($p<0.01$; difference = 2.70%; 95% CI:

0.80 to 4.60%) (Figure 3.4B). The difference of RV ECV with LV ECV in patients with PAH was significantly greater than the corresponding difference in patients with LHF ($p<0.01$; difference = 3.38%; 95% CI: 1.67 to 5.09%) (Figure 3.4C).

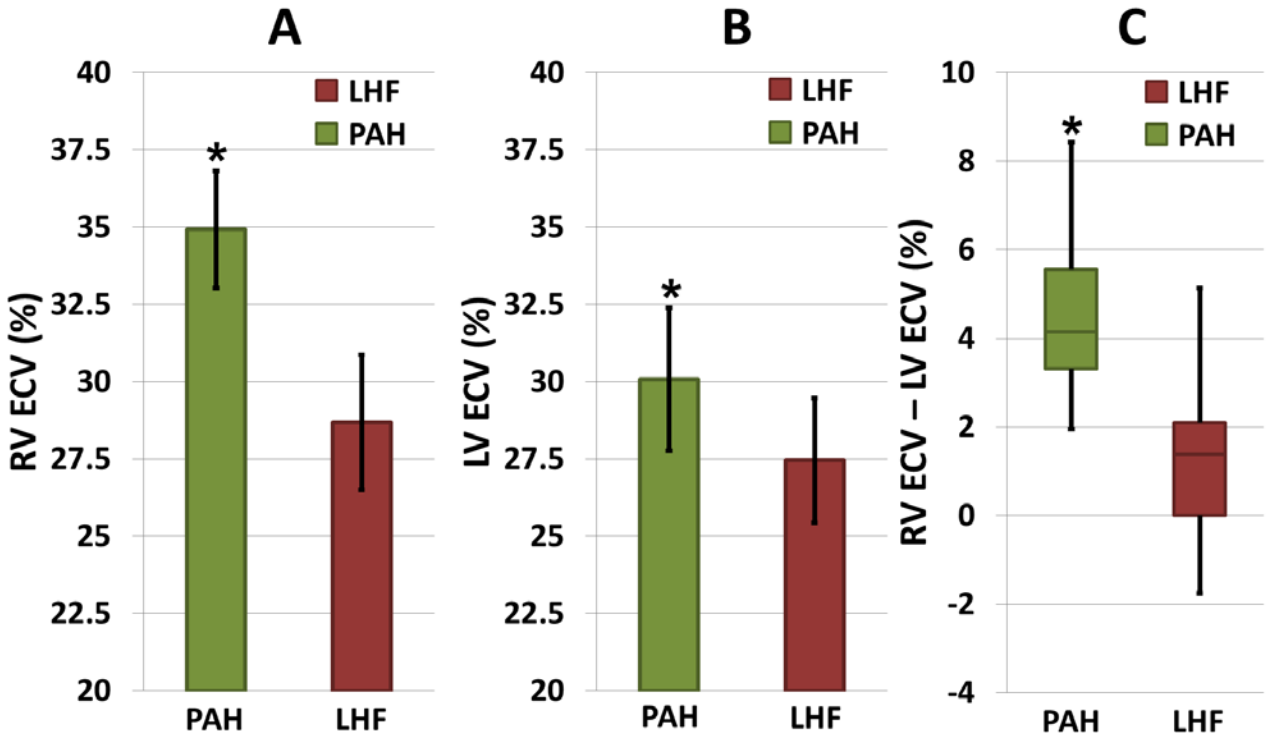

Figure 3.4: *Myocardial ECV measurement results.* ***A:*** *Comparison of RV myocardial ECV measurements.* ***B:*** *Comparison of LV myocardial ECV measurements.* ***C:*** *Comparison of the difference of RV ECV with LV ECV between patients with PAH and LHF. *: p<0.01 vs. ANGIE in HF patients. RV ECV and LV ECV were significantly higher in PAH patients than in LHF patients. Additionally, the difference between RV ECV and LV ECV in PAH patients was also significantly higher than the corresponding difference in LHF patients.*

3.3.4 Association of RV ECV with RV pressure and function parameters

Figure 3.5 summarizes the correlation results of RV ECV with RV pressure overload and RV function parameters. Specifically, the RV ECV showed positive correlation with RV systolic pressure ($r=0.6586$, $p<0.01$) (Figure 3.5A), indicating a relationship between RV fibrosis and RV pressure overload. The RV ECV also showed significant correlation with reduced RV function parameters, including RV ejection fraction ($r=-0.6366$, $p<0.01$) (Figure 3.5B), RV end-systolic volume index ($r=0.6567$, $p<0.01$) (Figure 3.5C), and RV end-diastolic volume index ($r=0.5596$, $p<0.02$).

3.3.5 Association of RV ECV with LV ECV and function parameters

Additionally, significant correlation was found between RV ECV and LV ECV ($r=0.7278$, $p<0.01$), indicating an association between RV and LV fibrosis. The RV ECV also showed significant correlation with LV function parameters, including LV ejection fraction ($r=0.7909$, $p<0.01$) and LV end-diastolic volume index ($r=-0.6429$, $p<0.01$).

3.3.6 Propagation of error and uncertainty in measuring ECV due to errors and uncertainties in T1 estimates

Figure 3.6 summarizes the error-propagation results for ECV estimation using two T1 mapping time points (one pre-contrast and one post-contrast). The error in ECV is more sensitive to myocardial T1 error than blood T1 error, and it is also more sensitive to error in post-contrast T1 values than native T1 values. The maximum error in ECV under the used simulation conditions was less than 20% of the true value. Figure 3.7

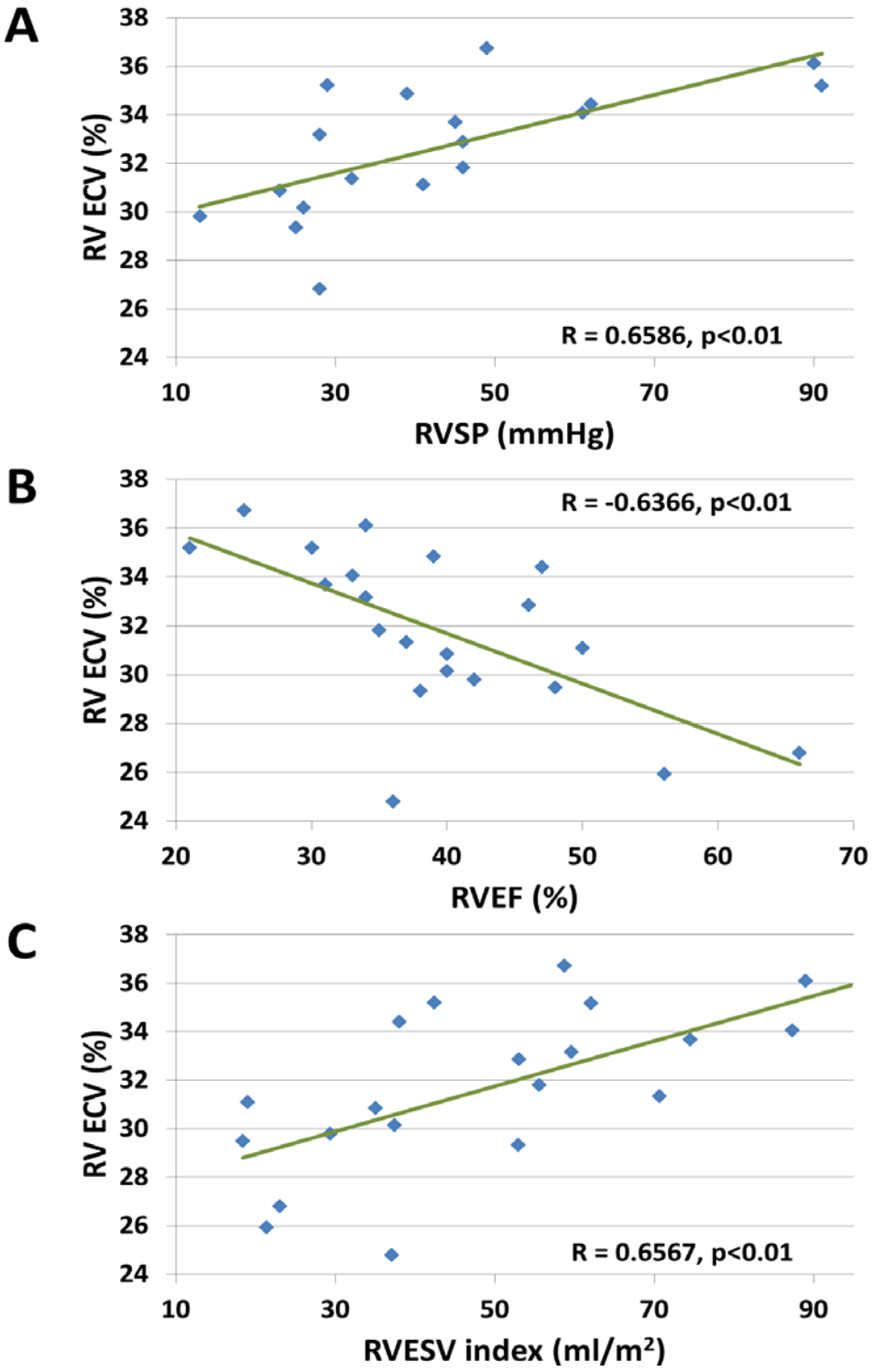

Figure 3.5: *Linear correlation results of RV ECV with RV pressure overload and RV function parameters.* ***A:*** *RV ECV vs echocardiography-based RVSP.* ***B:*** *RV ECV vs RV ejection fraction (RVEF).* ***C:*** *RV ECV vs RV end-systolic volume (RVESV) index.*

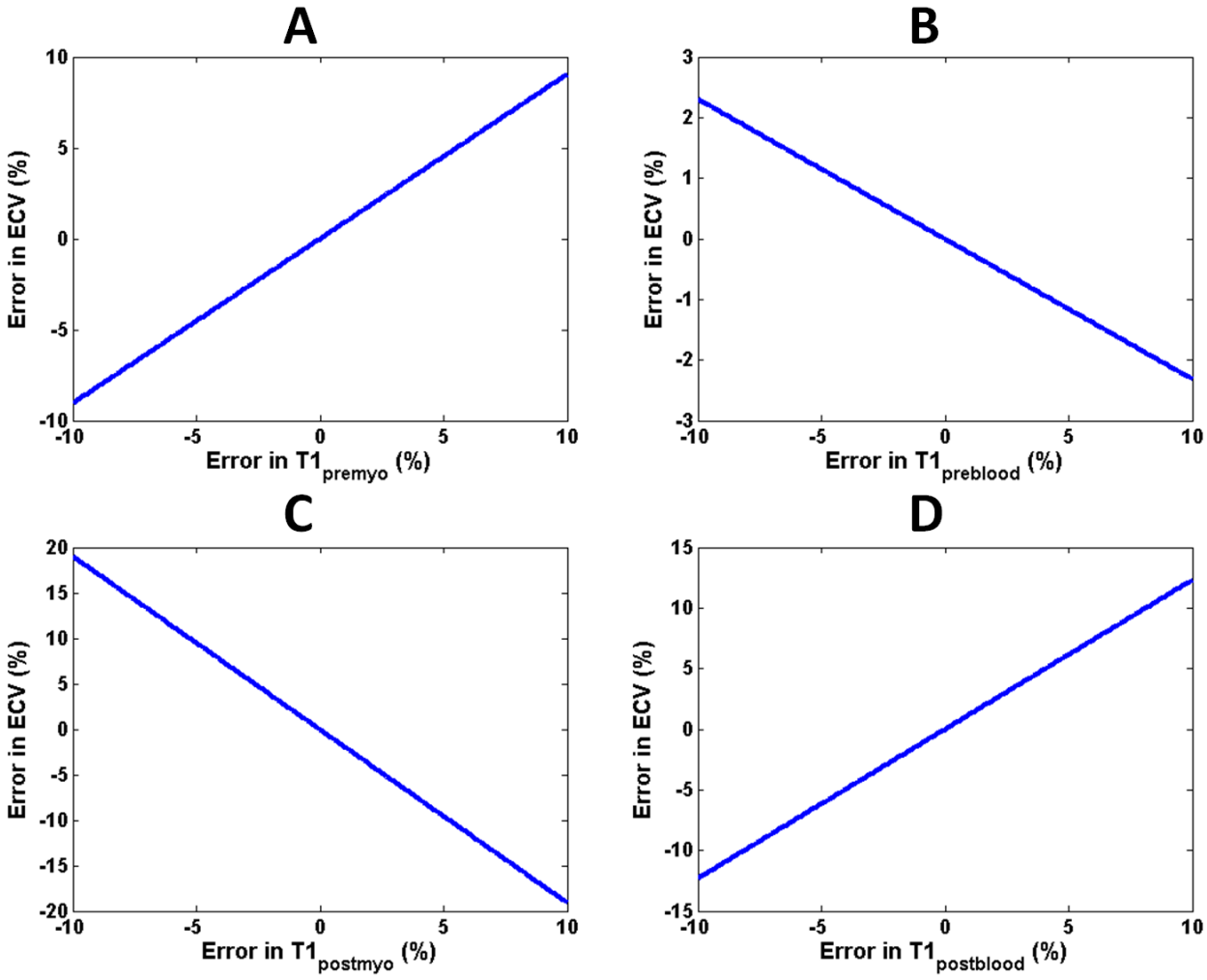

Figure 3.6: *Error propagation results for ECV estimation using T1 values from two time points (one pre-contrast and one post-contrast).* ***A:*** *Error in estimating ECV due to error in native (pre-contrast) myocardial T1.* ***B:*** *Error in estimating ECV due to error in native (pre-contrast) blood T1.* ***C:*** *Error in estimating ECV due to error in post-contrast myocardial T1.* ***D:*** *Error in estimating ECV due to error in post-contrast blood T1. The maximum error in ECV under these conditions was less than 20% of the true value.*

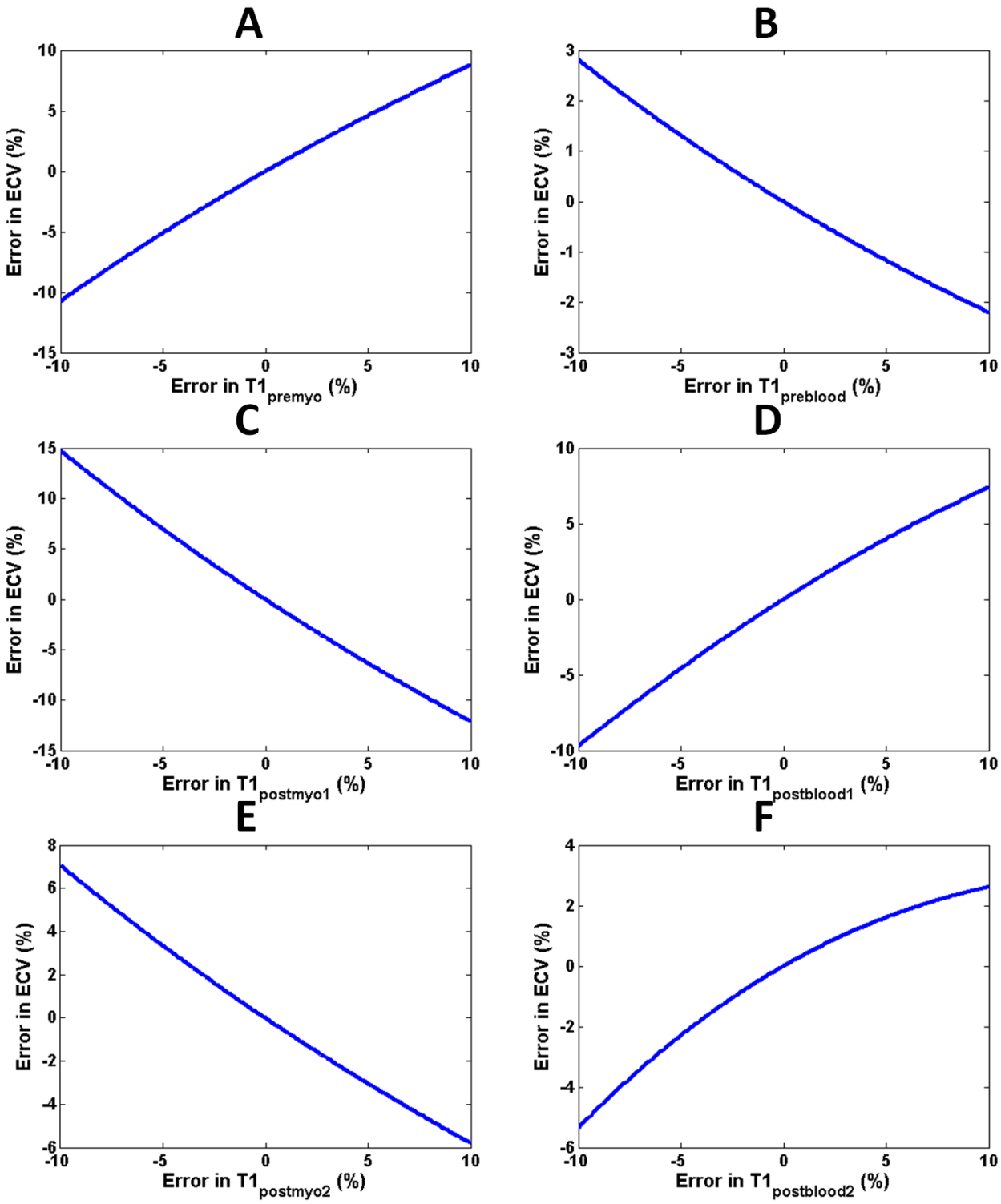

Figure 3.7: *Error propagation results for ECV estimation using T1 values from three time points (one pre-contrast and two post-contrast).* ***A:*** *Error in estimating ECV due to*

error in native (pre-contrast) myocardial T1. ***B:*** *Error in estimating ECV due to error in native (pre-contrast) blood T1.* ***C:*** *Error in estimating ECV due to error in first (earliest) post-contrast myocardial T1.* ***D:*** *Error in estimating ECV due to error in first (earliest) post-contrast blood T1.* ***C:*** *Error in estimating ECV due to error in second (latest) post-contrast myocardial T1.* ***D:*** *Error in estimating ECV due to error in second (latest) post-contrast blood T1. The maximum error in ECV under these conditions was less than 15% of the true value.*

summarizes the error-propagation results for ECV estimated using three time points (one pre-contrast and two post-contrast). Similar to the previous case, the error in ECV is more sensitive to error in myocardial T1 compared than in blood T1. Furthermore, the error in ECV is most sensitive to the errors in the earliest post-contrast time point and least sensitive to the errors in the latest post-contrast time point. The error propagation is asymmetric across zero and more sensitive to the underestimation of T1 values. The maximum error in ECV under the simulation conditions was less than 15% of the true value. Based on the phantom results for error values in T1 estimates, the maximum underestimation of ECV is 17.33% of the true value while the maximum overestimation of ECV is 13.46% of the true value. The maximum underestimation is present when there are simultaneous errors in native myocardial T1 (-9%) and post-contrast blood T1 (-7%). The maximum overestimation is present when there are simultaneous errors in native blood T1 (-10%) and post-contrast myocardial T1 (-5%). Based on the patient results, the difference (21.21%) in RV ECV between PAH and LHF patients expressed as a percentage of RV ECV in LHF patients is higher than the worst possible

overestimation of ECV (13.46%) as well as the worst possible underestimation of ECV (17.33%). Figure 3.8 shows simulation results estimating the uncertainty in ECV

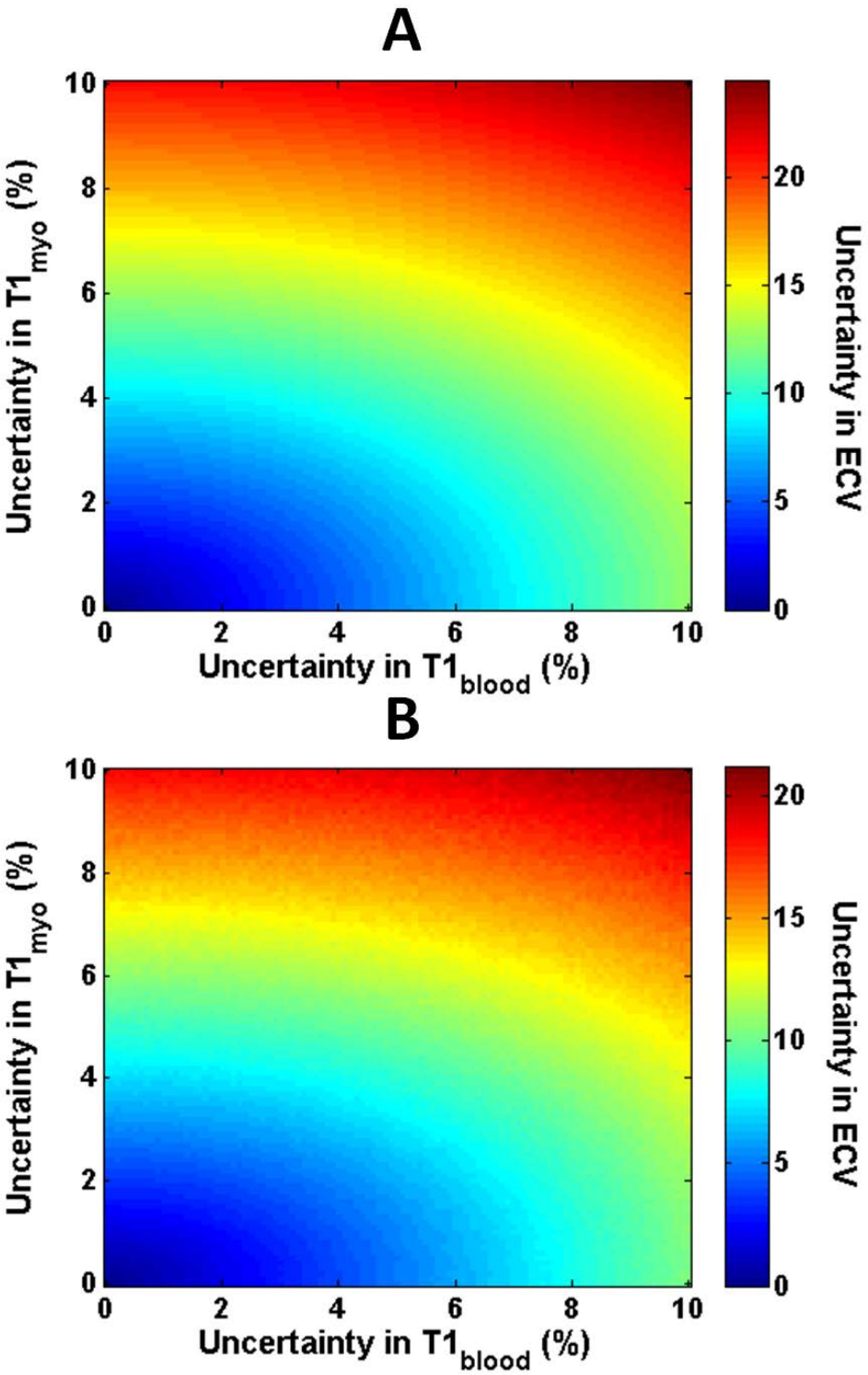

Figure 3.8: *Propagation of uncertainty in ECV due to uncertainties in T1 values.* ***A:*** *Simulation results for ECV estimation using two time points (one pre-contrast and one post-contrast).* ***B:*** *Simulation results for ECV estimation using three time points (one pre-contrast and two post-contrast).*

estimation due to uncertainties in blood and myocardial T1. The uncertainty in ECV is more sensitive to uncertainty in myocardial T1 than in blood T1. Based on the uncertainty results from the volunteer study, the uncertainty of ECV for the LV myocardium is 18.31% and for the RV myocardium is 18.90%. However, ECV values are estimated using global T1 values over a region of interest. Each region of interest approximately contains 100 pixels. Since averaging over 'n' samples reduces the uncertainty of the estimate by a factor of $\sqrt{n}$. The uncertainty in ECV is reduced by a factor of 10 (i.e. uncertainty of ECV in LV=1.83% of true value; RV=1.89% of true value) due to averaging over 100 pixels.

The results from this analysis provide crucial information from a perspective of designing efficient T1 mapping parameters. Errors in ECV are more sensitive to T1 values of the earliest post-contrast time point and the pre-contrast time point, and they are more sensitive to errors in myocardial T1 than blood T1. In order to reduce the errors in ECV, the T1 mapping technique should provide minimal errors in the earliest post-contrast and pre-contrast myocardial T1. However, the ranges for pre- and post-contrast injection T1 values are quite different. Usually, the same set of imaging parameters are used for pre and post-contrast T1 mapping to mitigate systemic bias in T1 estimates. Based on this analysis, a different set of parameters should be used for T1 mapping pre- and post-contrast injection, optimizing the T1 mapping at those time

points to reduce the error in the ECV measurement. This scheme should be explored in the future.

3.4 DISCUSSION

3.4.1 Main findings

We have demonstrated that high-resolution ANGIE T1 mapping can be used to non-invasively characterize not only the LV, but also the thin-walled RV myocardium by measuring the myocardial ECV in both. We detected an elevated RV ECV in patients with PAH compared to patients with LHF. Specifically, the key findings based on the results of this study are:

1) ANGIE T1 mapping accurately measures the ECV, illustrated by the LV ECV agreement between ANGIE and MOLLI in patients with PAH (mean difference = 0.36%; 95% CI: -1.14 to 1.86%) (Figure 3.3).
2) PAH patients had a higher RV ECV, indicative of a higher degree of RV fibrosis, than did LHF patients. The mean difference in RV ECV was 6.08% ($p<0.01$) (Figure 3.4A).
3) The degree of RV fibrosis in these patients, as measured by RV ECV, linearly increased with RV pressure overload as measured by RVSP ($r=0.6586$, $p<0.01$) (Figure 3.5A);
4) The degree of RV fibrosis in these patients linearly decreased with RV systolic function measured by RVEF ($r=-0.6366$, $p<0.01$) (Figure 3.5B).

5) The degree of RV fibrosis in these patients linearly increased with RV dilation, as measured by RV end-systolic volume index ($r=0.6567$, $p<0.01$) (Figure 3.5C).

3.4.2 Importance of RV ECV in the context of prior studies

A few previous studies have shown that the extent of enhancement in LGE MRI is positively correlated with an increase in afterload and inversely correlated with RV performance in patients with PAH(50,100-102). However, LGE MRI is only capable of detecting focal fibrosis, which is present at the advanced stages of PAH(49). Recently, the quantitative measurement of myocardial ECV was introduced(27,94), allowing the detection of both focal fibrosis and diffuse fibrosis, as well as other subtle changes in ECV(103). A few recent studies(104-106) have investigated RV fibrosis using T1 mapping MRI in the context of PAH. However, the evaluation of fibrosis in these studies was confined to either the RV insertion site or the inter-ventricular septum, which is an indirect assessment of the health of the entire RV. Fibrosis at those sites presents only at the advanced stages of PAH, by which time an optimal therapeutic window of opportunity may have already passed.

The quantitative assessment of fibrosis by directly estimating the ECV of the RV myocardium, including the free wall, may provide for the early detection of myocardial involvement in PAH. To the best of our knowledge, this is the first study presenting the measurement of RV ECV in the context of PAH. Interestingly, our study shows a stronger correlation of the degree of fibrosis with RV pressure overload and function than studies of Garcia-Alvarez et al and Garcia-Lunar et al(104-106). This may be due to the locations in the RV where the ECV measurements were taken. Specifically, we

measured fibrosis of the entire RV myocardium as opposed to just at the RV insertion site or the inter-ventricular septum. Furthermore, our results show that the degree of LV fibrosis in PAH patients increases with the degree of RV fibrosis.

3.4.3 Key impacts

Non-invasive measurement of ECV of RV myocardium, using ANGIE T1 mapping, represents a significant improvement over the measurement of focal fibrosis at the RV insertion site using LGE. Increased LV ECV is associated with adverse cardiovascular outcomes(107), and an increased ECV in the RV may provide a prognostic marker in patients with PAH. Since contrast-enhanced CMR T1 mapping can be performed repetitively as a serial or follow-up scan without any major side-effects, RV ECV as a measurement of RV fibrosis may be a useful endpoint in clinical studies designed at evaluating new therapies targeted at halting the progression of or reversing RV fibrosis. Furthermore, with the emergence of goal-oriented and patient-specific therapeutic management, the RV ECV could be used to assess disease progression, or it could be used as a surrogate marker to evaluate anti-fibrotic therapeutic response.

3.4.4 Study limitations

A limitation of this study is the small sample size of the enrolled patients. Additionally, the reference group of LHF subjects does not represent the ideal control for performing comparisons with PAH patients due to the potential presence of secondary effects on the RV. We used LHF patients as control subjects because measuring the ECV requires contrast administration, and these subjects were already scheduled to undergo

contrast-enhanced CMR. Even with these limitations, these results are promising, and this method merits evaluation in a future study with larger patient population.

3.5 CONCLUSION

Pre- and post-contrast ANGIE imaging provides high-resolution T1 mapping and ECV assessments for both the LV and the thin-walled RV. LV ECV by ANGIE and MOLLI were in close agreement. The degree of RV fibrosis in this patient cohort increased with RV pressure overload, RV dilation and decreasing RV systolic function. Quantitative tissue characterization of the RV, using the ECV estimated from contrast-enhanced ANGIE T1 mapping, may represent a valuable noninvasive marker of the health of the RV in patients with PAH.

Chapter 4

Development of a high resolution three-dimensional T1 mapping technique

4.1 INTRODUCTION

T1 mapping MRI has emerged as a valuable tool for evaluation of various cardiovascular diseases that affect the myocardial ECM and ECV (10,27,39-41,103,107). It has also shown potential for the diagnosis of systemic diseases involving substances such as lipids(108) or iron(109) that alter myocardial T1. The myocardial ECV calculated from contrast-enhanced T1 mapping MRI has been shown to correlate with diffuse myocardial fibrosis(27,39,110). The assessment of myocardial fibrosis would also be valuable in disorders such as pulmonary hypertension(49,50,104), arrhythmogenic right ventricular cardiomyopathy(51), congenital heart disease, and atrial fibrillation(52), where imaging thinner myocardial structures such as the RV and left atrial walls would be important. However current T1 mapping techniques such as MOLLI(47) and its variants(48,82) have limited spatial resolution, typically yielding in-

plane resolutions that are well-suited for T1 mapping of structures on the order of 1 cm^2 such as the LV wall. Thus, myocardial T1 mapping has generally been limited to the LV.

In Chapter 2, we developed ANGIE, a novel high-resolution T1 mapping method uses navigator-gating and readout segmentation to avoid cardiac and respiratory motion artifacts and enable free-breathing acquisition. It provides high spatial resolution T1 mapping for the assessment of thin structures such as the RV wall, and it was used to image the RV in PAH patients in Chapter 3. However, high resolution 2D imaging is limited by low SNR, low acquisition efficiency and restricted coverage of the heart. Furthermore, T1 mapping applications such as the quantification of peri-infarct regions and infarct tissue heterogeneity require high spatial resolution and continuous volumetric coverage of the heart. A 3D acquisition provides higher SNR and acquisition efficiency along with greater coverage of the heart, but standard 3D navigated techniques have prohibitively long scan times. Recently, 3D myocardial T1 mapping techniques have been proposed for volumetric coverage of the heart(111,112); however, those techniques do not provide adequate spatial resolution to image thin structures such as the RV wall within a clinically-acceptable scan time.

Thus, the aim of the present study was to extend ANGIE to perform high-resolution 3D T1 mapping of the heart within a clinically-acceptable scan time. An adaptively-driven undersampling strategy was developed, employing an image reconstruction algorithm that combines compressed sensing (CS) with local low-rank sparsity, partial Fourier and SENSE based parallel imaging (PI) to achieve high acceleration for 3D ANGIE. Computer simulations were performed to evaluate and

optimize the developed image reconstruction algorithm. 3D ANGIE was compared to 2D ANGIE and 2D MOLLI for T1 mapping of both ventricles in healthy volunteers.

4.2 METHODS

4.2.1 Pulse sequence

The 3D ANGIE pulse sequence is illustrated in Figure 4.1. The base pulse sequence is same as the one previously described for 2D acquisition(54). The basic acquisition is comprised of an inversion recovery Look-Locker experiment(64), with an inversion pulse followed by four consecutive ECG-triggered data acquisitions and a recovery period of two R-R intervals. To ensure that images are acquired at a consistent cardiac phase, the data acquisition is performed at a fixed delay time, TD, after R-wave detection. Each data acquisition block includes a navigator echo, an optional fat saturation module, a set of catalyzing RF pulses and a segmented readout module. The basic acquisition block is repeated to acquire all of the required readout segments at various inversion times. The navigator echo, formed using orthogonal slice-selective 90^0 and 180^0 RF pulses, is typically placed on the right hemi-diaphragm(65). The navigator acceptance window was set such that data not acquired during end expiration were discarded. The readout module consisted of a segmented balanced SSFP acquisition. Each readout was preceded by a train of catalyzing RF pulses with Kaiser-Bessel window ramped flip angles to dampen the transient signal oscillations(66).

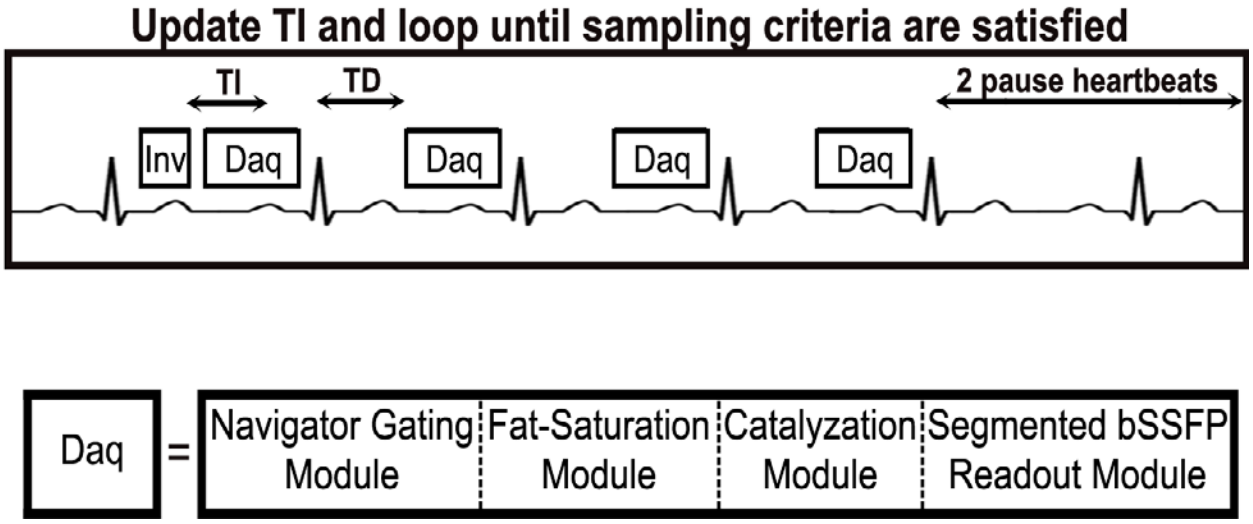

Figure 4.1: *A diagram showing the ANGIE pulse sequence scheme. This instance of ANGIE utilizes an inversion-recovery Look-Locker experiment with four ECG-triggered data acquisition modules and a waiting period of two R-R intervals. The sequence is repeated, after updating TI, until the stopping criteria are satisfied. The data acquisition module is comprised of a navigator-gating module, fat suppression, a set of catalyzing RF pulses, and a segmented balanced SSFP readout.*

4.2.2 Image reconstruction algorithm

Standard 3D navigator-based techniques have prohibitively long scan times. Correspondingly, a simple extension of 2D ANGIE to perform a 3D acquisition would significantly increase the scan time, making it unsuitable for patient studies. Hence, acceleration of 3D ANGIE acquisition for reduction of scan time to meet clinical requirements is one of the key challenges of this project. 2D ANGIE employs an image reconstruction algorithm comprised of CS and PI for acceleration. Since ANGIE images possess spatio-temporal correlation, the ANGIE image series (N_x by N_y by N_t) was

reshaped into a Casorati matrix (N_x x N_y by N_t) and the rank of this Casorati matrix was used as the CS sparse domain(89). The reconstruction problem was formulated as the following optimization equation:

$$\mathbf{m}^* = \arg\min_{\mathbf{m}} \|\mathcal{F}_u C_i \mathbf{m} - \mathbf{d}\|_2 + \lambda \|\mathbf{m}\|_* \quad [4.1]$$

where **m** is the image after coil combination, C_i is the individual coil sensitivity profile, **d** is the measured k-space data, and $\| \quad \|_*$ is the nuclear norm operator. As the spatial dimensions (N_x x N_y) become large compared to the temporal dimension (N_t), the rank of the Casorati matrix becomes almost equal to the temporal dimension (N_t). Such a condition limits the sparsity due to spatio-temporal correlations, consequently limiting the achievable acceleration rate. This effect is more severe for volumetric datasets due to the additional spatial dimension. Prior studies have shown that dynamic MRI data present higher local spatio-temporal correlation than global spatio-temporal correlation(113-115), which allows higher acceleration rates to be achieved. An image reconstruction algorithm that combines CS with local low-rank sparsity, partial Fourier and SENSE PI was developed to achieve high acceleration for 3D ANGIE. The updated reconstruction problem was formulated as the following optimization equation:

$$\mathbf{m}^* = \arg\min_{\mathbf{m}} \|\mathcal{F}_u C_i \mathbf{m} - \mathbf{d}\|_2 + \lambda_1 (\textstyle\sum_b \|\mathbf{m_b}\|_*) + \lambda_2 \left\|\mathbf{m} - |\mathbf{m}| * e^{-2\pi i \varphi_{lowres}}\right\|_2 \quad [4.2]$$

where **m** is the image after coil combination, C_i is the individual coil sensitivity profile, **d** is the measured k-space data, $\mathbf{m_b}$ is a small region of **m** reformatted into a Casorati matrix, $\| \quad \|_*$ is the nuclear norm operator, and φ_{lowres} is the reference low resolution phase image. Unaliased low resolution images were obtained using the central fully-

sampled region of k-space, and φ_{lowres} was computed from these images. Sensitivity maps were calculated from the low resolution unaliased images based on an eigenvector filter approach(68). A projection onto convex sets (POCS) algorithm was used to solve the reconstruction problem.

4.2.3 Adaptive sampling strategy

Data sampling patterns suitable for CS often utilize a fully-sampled or nearly-fully-sampled central k-space region and a randomly-undersampled outer k-space region. For most current CS applications, a fixed, predetermined sampling pattern is used. However, for navigator-gated methods such as ANGIE, decisions regarding acceptance and rejection of the data occur during the scan, and completing sampling patterns with acceleration factors determined *a priori* may lead to very long acquisition times. In Chapter 2 of this dissertation, an adaptive acquisition strategy(116) was developed that makes real-time adjustments to the k-t sampling pattern based on which data have and have not been acquired. Such an acquisition strategy may be used to reduce the total scan time while also collecting k-t data that are well-suited to image reconstruction using CS. For 2D ANGIE, the adaptive selection strategy considers the entire k_y-t space and computes the next segment of phase encoding lines to acquire by determining which lines have been acquired least often over all of the inversion times (i.e., using a probability density function).

A Poisson-disc based sampling strategy was employed to increase image reconstruction quality. Poisson-disc based sampling is a strategy in which the sampling positions – here, individual k-space lines within the k_y-k_z space -- are decided based on

a Poisson-disc distribution to avoid clustered sampling. Each sampling point is surrounded by a forbidden region ("forbidden disc") that no other points can reside in. Previous studies have shown that Poisson-disc based sampling provides superior CS-PI reconstruction results compared to random sampling(117,118). For 3D ANGIE, we combined both strategies together: the adaptive selection strategy ensured that probability density function-based criteria are satisfied across time (over k-t) and that Poisson-disc based sampling criteria are satisfied across space (over k_y-k_z).

4.2.4 Post processing

Data binning, phase correction, and T1 calulations were performed as described in Chapter 3.

4.2.5 Validation of image reconstruction algorithm

The proposed image reconstruction algorithm was evaluated and optimized using computer simulations based on retrospective undersampling of a fully-sampled 3D ANGIE dataset. However, a high-resolution fully-sampled 3D ANGIE acquisition will have extremely long scan time, which may lead to subject discomfort and motion artifacts. Since the evaluation and optimization of the image reconstruction algorithm requires ground truth images, a low-resolution fully-sampled 3D ANGIE dataset was used for these simulations. Relevant parameters for fully-sampled low resolution 3D ANGIE were FOV read = 400mm, FOV phase = 72.5%, matrix size = 200x144x20, pixel size = 2.0x2.0x5 mm^3, flip angle = 35^0, acquisition window = 170.5ms, initial TI = 220ms, TI increment = 80ms, phase encodes per readout = 55, and navigator acceptance window = ± 3 mm. Image reconstruction results of retrospectively-

undersampled fully-sampled datasets were evaluated qualitatively as well as quantitatively at various acceleration rates. Quantitative evaluation was performed using RMSE and SSIM, as described in Chapter 2, section 2.3.4(70).

4.2.6 Selection of the acceleration rate

Retrospective-undersampling analysis using a low-resolution fully-sampled 3D ANGIE dataset is sufficient for evaluation of an image reconstruction algorithm. However, reconstruction analysis of a low-resolution dataset cannot provide the optimal acceleration rate for a high-resolution image set due to differences in matrix size and SNR. Since a high-resolution fully-sampled 3D ANGIE acquisition may be corrupted with motion artifacts due to subject discomfort from the lengthy scan time, reconstructions from a high-resolution 3D ANGIE dataset with a conservative acceleration rate were used as a reference for these simulations. Relevant parameters for the 3D ANGIE acquisition were TR = 3.5ms, TE = 1.77ms, FOV read = 310mm, FOV phase = 100%, matrix size = 224x224x14 (including 2 partitions for slice oversampling), pixel size = 1.4x1.4x4 mm^3, flip angle = 35^0, acquisition window = 112ms, initial TI = 175ms, TI increment = 70ms, phase encodes per readout = 32, navigator acceptance window = ± 3 mm , partial Fourier reduction factor of 3/4 along the phase encode direction, and effective prospective acceleration rate = 6. A conservatively-accelerated 3D ANGIE dataset was retrospectively undersampled at higher acceleration rates, and the T1 maps generated from this reconstruction were quantitatively evaluated. The evaluation was performed primarily by comparing the definition of the wall of the RV with the reference results. The optimal acceleration rate, based on these simulation results, was used for the volunteer study.

4.2.7 Phantom study

Eleven agarose gel phantoms containing millimolar concentrations of copper sulphate(71,72), with T1 values ranging from 200ms to 1500ms and T2 values near 50ms or 200ms, were used to validate T1 estimates made using 3D ANGIE. The phantoms were scanned at heart rates ranging from 40 bpm to 100 bpm. ANGIE acquisition parameters included: TR = 3.5ms, TE = 1.75ms, FOV read = 300-310mm, FOV phase = 100%, matrix size = 224x224x14 (including 2 partitions for slice oversampling), pixel size = 1.3-1.4x1.3-1.4x4 mm^3, flip angle = 35^0, acquisition window = 112ms, initial TI = 175ms, TI increment = 70ms, phase encodes per readout = 32, navigator acceptance window = ± 3 mm, and partial Fourier reduction factor of 3/4 along the phase encode direction. The acceleration rate was chosen based on the results from the evaluation of the image reconstruction algorithm in section 4.2.6. The navigator was placed in a background region to randomly accept/reject the data. T1 estimates were computed from CS-reconstructed images as described in Chapter 2, section 2.3.3. A single point inversion-recovery spin-echo sequence with twenty TI values ranging from 50-5500ms was used to measure the reference T1 values of the phantoms.

4.2.8 Volunteer study

All studies were performed in accordance with protocols approved by our institutional review board. High-resolution native T1 mapping of the heart using 3D ANGIE was evaluated by comparing 3D ANGIE T1 measurements with 2D ANGIE and 2D MOLLI in six healthy volunteers. Healthy volunteers underwent an MRI on a 1.5T system (Avanto, Siemens, Erlangen, Germany) using a 32-channel phased-array receiver coil. The

image acquisition was timed to occur at end systole to take advantage of the thicker RV wall and greater separation of the RV wall from the liver and the chest wall. Relevant parameters for high-resolution 3D ANGIE were TR = 3.5ms, TE = 1.75ms, FOV read = 300-310mm, FOV phase = 100%, matrix size = 224x224x14 (including 2 partitions for slice oversampling), pixel size = 1.3-1.4x1.3-1.4x4 mm^3, flip angle = 35^0, acquisition window = 112ms, initial TI = 175ms, TI increment = 70ms, phase encodes per readout = 32, navigator acceptance window = ± 3 mm, and partial Fourier reduction factor of 3/4 along the phase encode direction. The acceleration rate was chosen based on the results from the evaluation of image reconstruction algorithm. 2D MOLLI and 2D ANGIE were also performed at basal, mid-ventricular, and apical short-axis slice positions. A shorter variant[38, 39] of MOLLI comprising of two inversion recovery based Look-Locker experiments was used in this study, as described in Chapter 3, Section 3.2.2.g(90,91). Relevant MOLLI imaging parameters were TR = 2.6ms, TE =1.16 ms, FOV read = 390-403mm, FOV phase = 77.1%, matrix size = 192x118, pixel size = 2.5-2.6x2-2.1 mm^2, flip angle = 35^0, slice thickness = 4mm, acquisition window = 180ms, initial TI = 100ms, and TI increment = 80ms. Relevant imaging parameters for high-resolution 2D ANGIE were TR = 3.5ms, TE = 1.75ms, FOV read = 300-310mm, FOV phase = 100%, matrix size = 224x224, pixel size = 1.3-1.4x1.3-1.4 mm^2, flip angle = 35^0, slice thickness = 4mm, acquisition window = 112ms, initial TI = 175ms, TI increment = 70ms, phase encodes per readout = 32, navigator acceptance window = ± 3 mm, TSPR threshold = 0.25, and CRLB threshold = $950ms^2$. T1 maps were generated from the reconstructed images, and contours were drawn using the reconstructed magnitude images to

compute myocardial and blood T1 values. The contours were drawn in a conservative manner to avoid trabeculations.

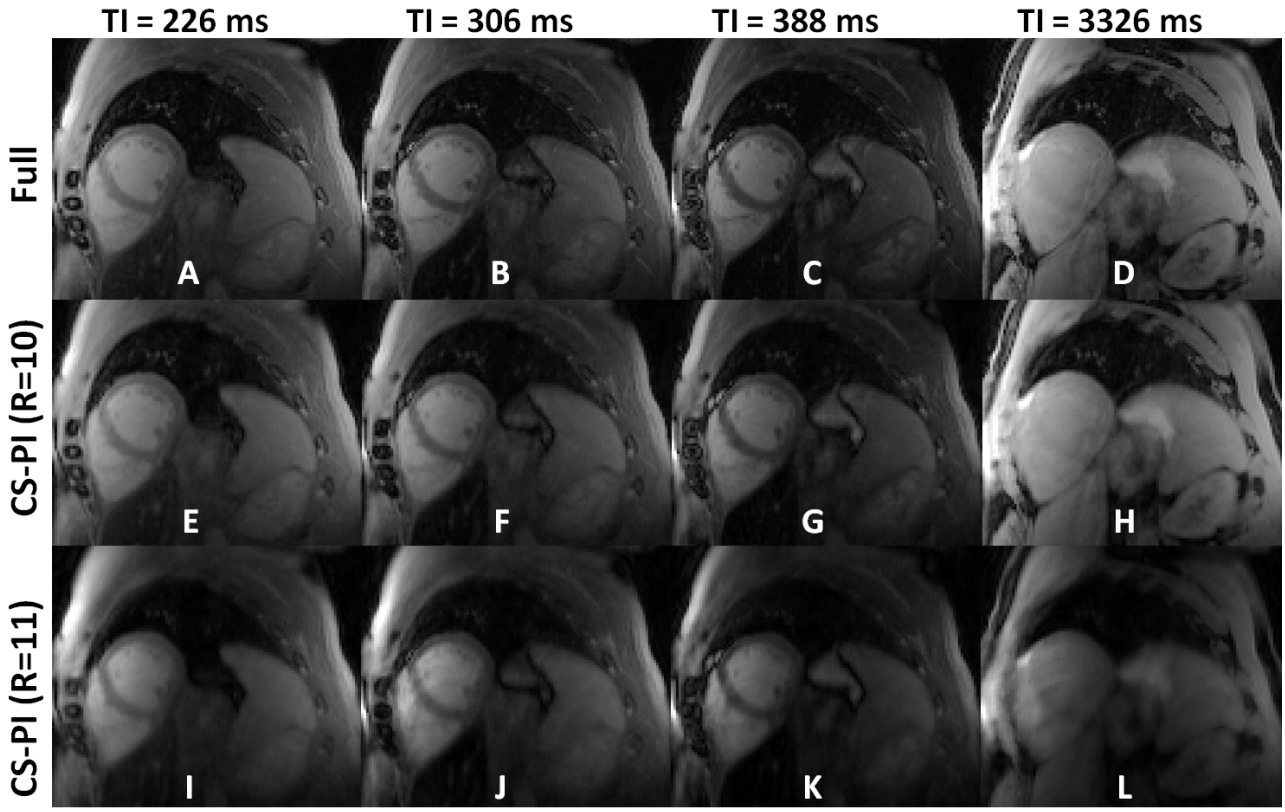

Figure 4.2: *Example reconstruction results from computer simulations retrospectively undersampling a low-resolution fully-sampled 3D ANGIE dataset. Fully sampled (**A-D**), CS-PI reconstructed (Rate 10) (**E-H**) and CS-PI reconstructed (Rate 11) (**I-L**) images from a single partition at four inversion time points of a 3D ANGIE dataset acquired from a healthy volunteer. The image reconstruction algorithm effectively suppresses aliasing artifacts and retains image spatial resolution for rate 10 undersampling, but not for rate 11 undersampling. These results illustrate that high acceleration rates can be achieved using the proposed image reconstruction algorithm.*

4.3 RESULTS

4.3.1 Computer simulations to validate image reconstruction algorithm

Figure 4.2 shows example results from retrospective acceleration simulations comparing the reconstruction image quality at two acceleration rates with fully-sampled reference images. Specifically, example CS-PI reconstructed images from a single partition at four inversion times, generated from a low-resolution fully-sampled 3D ANGIE dataset retrospectively undersampled at rate 10 and rate 11, are shown in Figure 4.2E-H and Figure 4.2I-L, respectively. Corresponding fully-sampled reference images, generated using the Fourier transform of the fully-sampled dataset, are shown in the top row (Figure 4. A-D). Visual inspection shows that the resulting images generated using rate 10 undersampling most closely resemble the fully-sampled images. The image reconstruction algorithm effectively suppresses aliasing artifacts and retains spatial resolution data acquired with rate 10 acceleration. However, the images reconstructed using rate 11 undersampling show residual aliasing artifacts and image blurring. Figure 4.3 summarizes the quantitative evaluation results from nine sets of simulations. The difference for RMSE and SSIM between rate 10 and 11 is higher than the corresponding difference between rate 9 and 10, suggesting that the optimal acceleration rate for low-resolution 3D ANGIE acquisition is rate 10. These results illustrate that low-resolution 3D ANGIE using the proposed reconstruction algorithm is capable of achieving a high acceleration rate (R=10).

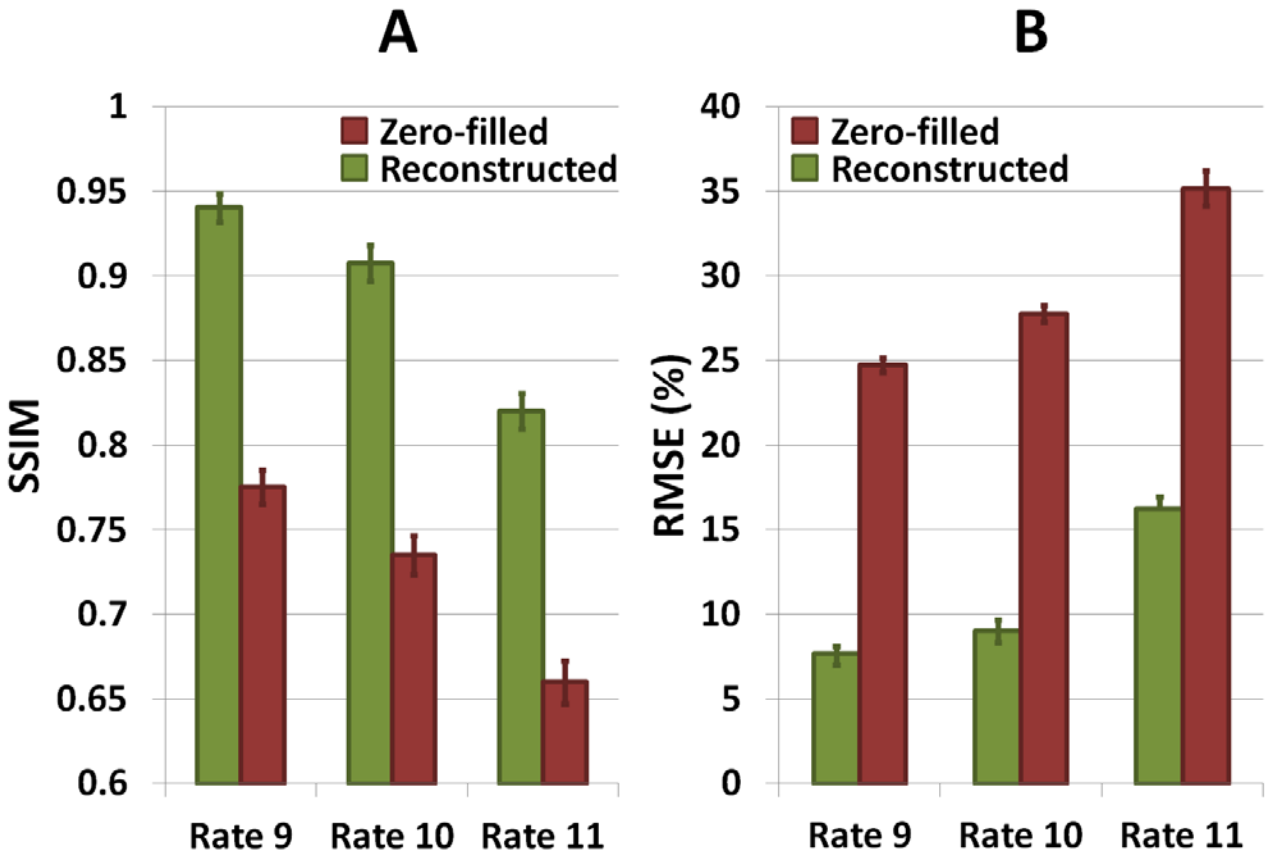

Figure 4.3: *Quantitative evaluation results of computer simulations for validation of image reconstruction algorithm. Structural similarity (mean ± standard deviation) (**A**) and root mean squared error expressed as percentage (mean ± standard deviation) (**B**), averaged over time and partitions, of the CS-PI reconstructed images compared to the fully-sampled reference images. The difference for RMSE and SSIM between rate 10 and 11 is higher compared to the corresponding difference between rate 9 and 10, suggesting the optimal acceleration rate for low-resolution 3D ANGIE acquisition is rate 10.*

4.3.2 Computer simulations for selection of acceleration rate

Figure 4.4 shows example T1 maps summarizing results from computer simulations for selection of acceleration rate. Specifically, example T1 maps at three different partitions, generated using a prospectively accelerated (rate 6) 3D ANGIE dataset retrospectively undersampled to rate 7 and rate 8 are shown in Figure 4.4D-F and Figure 4.4G-I, respectively. Corresponding reference T1 maps, which were generated from prospectively accelerated (rate 6) 3D ANGIE acquisitions, are shown in the top row (Figure 4.4A-C). The definition and the coverage of the RV wall (arrows) is preserved in the results from rate 7 accelerated dataset (Figure 4.4D-F) and are comparable to the reference results using rate 6 acceleration (Figure 4.4A-C). However, images reconstructed using rate 8 acceleration (Figure 4.4G-I) show some loss of RV definition as well as coverage (arrows). The simulation results show that rate 7 acceleration is optimal for high-resolution 3D ANGIE, using the acquisition parameters for the dataset in these simulations. Based on these results, rate 7 acceleration was employed for 3D ANGIE acquisitions in subsequent phantom and volunteer studies.

4.3.3 Phantom study

The phantom 3D ANGIE T1 estimates agreed reasonably well to the conventional inversion recovery reference T1 values, with a slope of 0.90 ± 0.04 and a bias of 62 ± 15ms over all simulated heart rates using a linear model ($T1_{ANGIE}$ = slope*$T1_{ref}$+bias). Figure 4.5A displays the correlation between reference T1 estimates and ANGIE T1 estimates, using a simulated ECG signal with a heart rate of 60bpm. Figure 4.5B

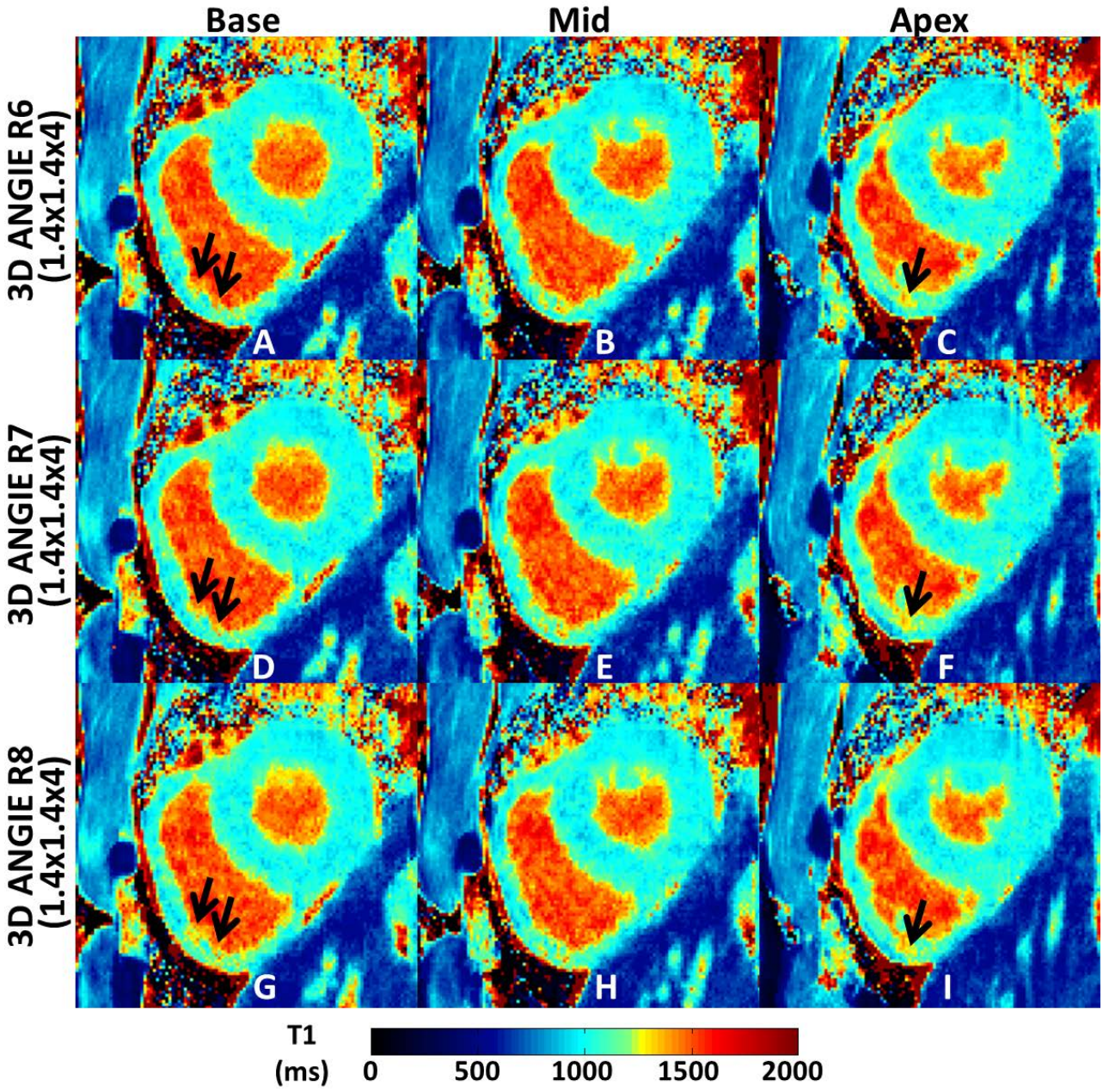

Figure 4.4: *Example results from simulations for selection of acceleration rate. High – resolution T1 maps at three different slice positions generated using a* ***A-D:*** *prospectively accelerated (rate 6) 3D ANGIE dataset as reference;* ***E-H:*** *prospectively accelerated (rate 6) 3D ANGIE dataset retrospectively undersampled to rate 7; and* ***I-L:***

*prospectively accelerated (rate 6) 3D ANGIE dataset retrospectively undersampled to rate 8. The definition and the coverage of RV wall (arrows) is preserved for results from the rate 7-accelerated dataset (**D-F**) but lost for results from the rate 8-accelerated dataset (**G-I**) compared to results from rate 6 accelerated dataset (**A-C**). These results illustrate that rate 7 acceleration is optimal for high-resolution 3D ANGIE with the acquisition parameters used for the dataset in these simulations.*

displays the percentage error in measuring T1 using ANGIE for all eleven phantoms at four different simulated heart rates. The maximum absolute error under these conditions was less than 10%.

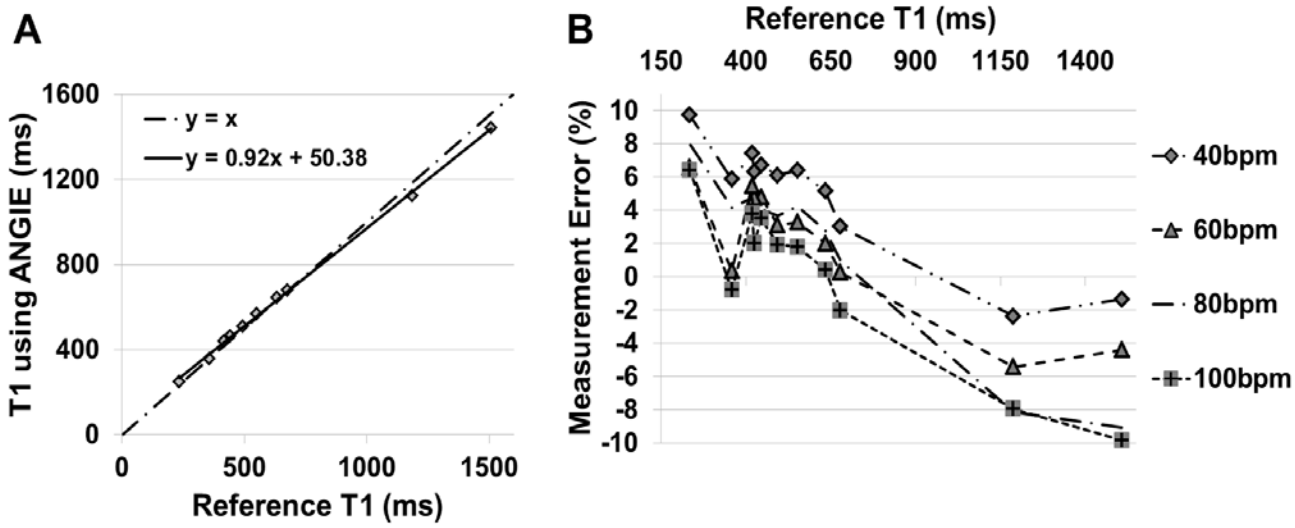

Figure 4.5: *Phantom results. **A:** Using a simulated ECG with heart rate at 60bpm, a good correlation of T1 estimates is achieved comparing ANGIE to the reference inversion-recovery spin echo method. **B:** Percentage error in T1 estimates using ANGIE, as compared to the IR spin echo reference method, for eleven phantoms at four different simulated heart rates.*

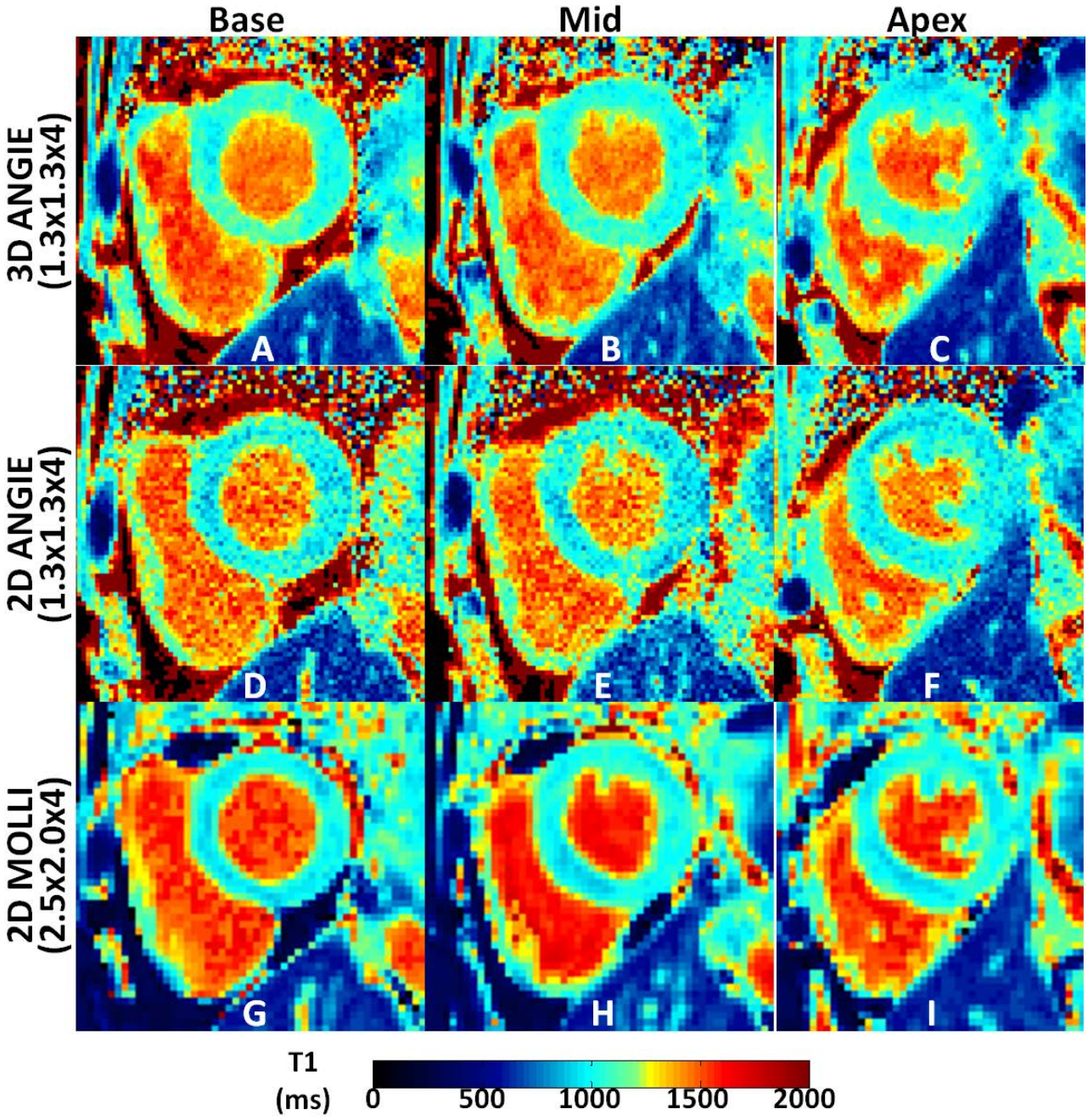

Figure 4.6: *Comparison of T1 mapping techniques in a healthy volunteer. Example native T1 maps from a healthy volunteer at three different slice positions acquired using 3D ANGIE (**A-C**), 2D ANGIE (**D-F**) and 2D MOLLI (**G-I**). 2D MOLLI provided high SNR but incomplete definition of the RV wall, whereas 2D ANGIE provided good definition of*

the RV wall but lower SNR. However, 3D ANGIE provided both good definition of the RV wall and high SNR.

4.3.4 Volunteer study

Example T1 maps acquired from a healthy volunteer comparing all three T1 mapping techniques are shown in Figure 4.6. Specifically, figure 4.6A-C, 4.6D-F and 4.6G-I are T1 maps at basal, mid-ventricular, and apical slices generated from 3D ANGIE, 2D ANGIE, and 2D MOLLI, respectively. 2D MOLLI (Figure 4.6G-I) provided high SNR but incomplete definition of the RV wall, whereas 2D ANGIE (Fig. 4.6D-F) provided good definition of the RV wall but lower SNR. Three-dimensional ANGIE (Fig. 4.6A-C) provided good definition of the RV wall as well as high SNR. Figure 4.7 shows the results from quantitative comparisons of 3D ANGIE, 2D ANGIE and 2D MOLLI. In particular, Figures 4.7A and 4.7B shows Bland-Altman plots comparing the mean T1 estimates measured using 3D ANGIE with 2D ANGIE and 2D MOLLI respectively. Figure 4.7C shows bar chart comparing the standard deviation of T1 estimates of pixels within a contour for 3D ANGIE, 2D ANGIE and 2D MOLLI. The left ventricular myocardium and blood T1 estimates using 3D ANGIE were in close agreement with 2D ANGIE (mean difference = 0.2ms; 95% CI: -60.9ms to 61.4ms) and 2D MOLLI (mean difference = 0.0ms; 95% CI: -74.4ms to 74.4ms). The RV T1 estimates using 3D ANGIE were in close agreement with 2D ANGIE. 3D ANGIE provided significantly lower intrascan variation in the RV myocardial ($p<0.02$), LV myocardial ($p<0.01$), and LV blood pool ($p<0.01$) T1 estimates compared to 2D ANGIE. 3D ANGIE also provided

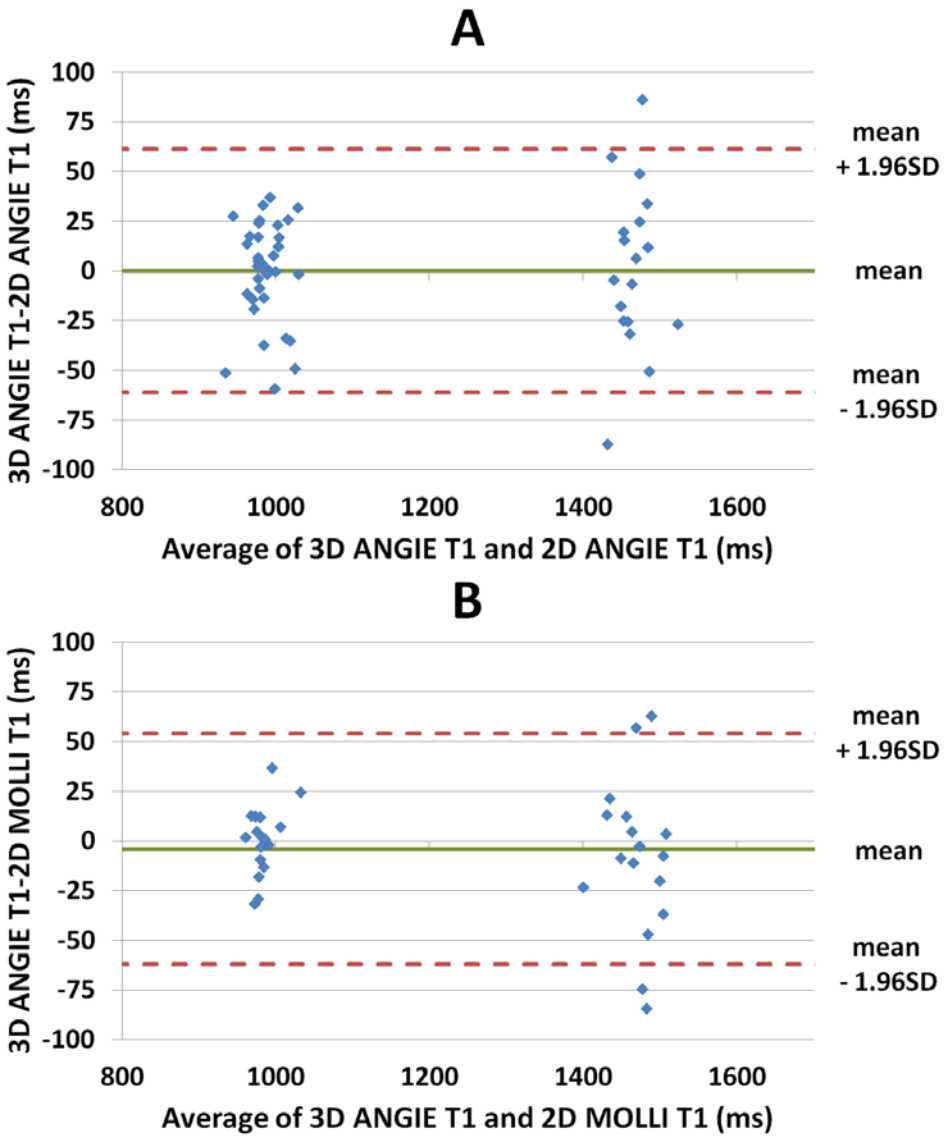
A
3D ANGIE T1-2D ANGIE T1 (ms)
100
75
50
25
0
-25
-50
-75
-100
800
1000
1200
1400
1600
Average of 3D ANGIE T1 and 2D ANGIE T1 (ms)
mean
+ 1.96SD
mean
mean
- 1.96SD
B
3D ANGIE T1-2D MOLLI T1 (ms)
100
75
50
25
0
-25
-50
-75
-100
800
1000
1200
1400
1600
Average of 3D ANGIE T1 and 2D MOLLI T1 (ms)
mean
+ 1.96SD
mean
mean
- 1.96SD
C
Std dev T1 (ms)
160
140
120
100
80
60
40
20
0
#
*
*
*
RV myo
LV myo
LV blood
2D MOLLI
2D ANGIE
3D ANGIE

Figure 4.7: *Quantitative comparison between 3D ANGIE, 2D ANGIE and 2D MOLLI in six healthy volunteers.* ***A:*** *Bland-Altman plot comparing mean T1 estimates measured using 3D ANGIE with 2D ANGIE.* ***B:*** *Bland-Altman plot comparing mean T1 estimates measured using 3D ANGIE with 2D MOLLI.* ***C:*** *Comparison of the standard deviation of T1 estimates from pixels within a contour. #: p<0.02 v.s. 3D ANGIE; *p<0.01 vs 3D ANGIE (A and B) Myocardial and blood T1 estimates were in close agreement between all three techniques. (C) 3D ANGIE showed significantly lower intrascan variation in the RV myocardial (p<0.02), LV myocardial (p<0.01) and LV blood pool (p<0.01) T1 estimates compared to 2D ANGIE, and additionally in the LV blood pool (p<0.01) T1 estimate compared to 2D MOLLI.*

significantly lower intrascan variation in the LV blood pool T1 ($p<0.01$), while the intrascan variation in the LV myocardial T1 trended lower compared to 2D MOLLI ($p=0.076$).

Table 4.1 summarizes the scan time results. The acquisition time for 3D ANGIE was 6.4 ± 1.4 mins for the entire slab and 2.1 ± 0.8 mins per slice for 2D ANGIE, illustrating the improvement in acquisition time per unit slice. However, the navigator acceptance rate was higher for 3D ANGIE compared to 2D ANGIE. The subjects usually fell asleep during the 3D ANGIE acquisition resulting in a consistent and shallow breathing pattern.

Table 4.1. Scan time results from healthy volunteer study

	2D MOLLI	2D ANGIE	3D ANGIE
Scan Time	12 (hb)	2.1 ± 0.8 mins	6.4 ± 1.4 mins
Accel. Rate	1.7	2.0	7.0
Navigator Efficiency (%)	-	57 ± 14	67 ± 15
Number of slices	1	1	12
Scan time per slice	12 (hb)	128 ± 50 s	32 ± 7 s

4.4 DISCUSSION

We developed an improved method to perform high-resolution 3D cardiac T1 mapping within a clinically reasonable scan time. 3D ANGIE makes use of a segmented readout, navigator gating, adaptive data undersampling, and parallel-CS image reconstruction to achieve the necessary acquisition requirements. The proposed image reconstruction algorithm was evaluated using simulations to determine an optimal undersampling rate. The accuracy of cardiac T1 estimation and the scan time using 3D ANGIE were evaluated by performing comparisons with 2D MOLLI and 2D ANGIE in healthy volunteers.

Figure 4.7B compares the intrascan variation in T1, measured as the standard deviation in T1 of all the pixels within a contour, between the three techniques. The intrascan T1 variation for the RV myocardium ($p<0.02$), LV myocardium ($p<0.01$) and LV blood ($p<0.01$) was significantly lower using 3D ANGIE than 2D ANGIE. However, the mean difference between the intrascan T1 variation using 3D ANGIE and 2D ANGIE was much lower for the RV myocardium compared to the LV myocardium and LV blood, with differences of 22.0 ms, 45.1 ms, and 48.7 ms, respectively. The RV myocardial wall is thin and known to be highly trabeculated; therefore, the intrascan RV T1 variation is

affected not only by the SNR of the acquisition technique but also by the partial volume effect due to minor trabeculations. Alternatively, the LV myocardial wall is thick and does not contain minor trabeculations, so its intrascan T1 variation, and additionally that of the LV blood pool, is primarily affected by the SNR of the acquisition technique. Additionally, the intrascan T1 variation using 3D ANGIE was significantly lower for the LV blood pool and trended lower for the LV myocardium compared to 2D MOLLI ($p<0.01$ and $p=0.076$, respectively), illustrating the SNR improvement for high-resolution 3D ANGIE relative to low-resolution 2D MOLLI.

As detailed in Chapter 3, myocardial fibrosis is assessed by calculating the myocardial ECV from contrast-enhanced T1 mapping images. Therefore, it is crucial to understand the propagation of error and uncertainty in ECV due to errors and uncertainties in the T1 estimates from 3D ANGIE. Based on the analysis described in section 2.3.9 and phantom results for error values in T1 estimates in section 4.3.3, the maximum underestimation of ECV using 3D ANGIE is 22.13%, and the maximum overestimation of ECV using 3D ANGIE is 16.37%. The maximum underestimation is present when there are simultaneous errors in native and post-contrast myocardial T1. The maximum overestimation is present when there are simultaneous errors in native and post-contrast blood T1. Based on the analysis described in section 2.3.9 and uncertainty results from the volunteer study, the uncertainty of ECV for the LV myocardium is 12.68% of the true value and for the RV myocardium is 16.87% of the true value.

Quantitative assessment of left atrial myocardial fibrosis would also be valuable in disorders such as atrial fibrillation(52). However, the left atrial wall is extremely

thin(119), with a thickness of 1.89 ± 0.48 mm and a range of 0.5-3.5mm. Thus, T1 mapping MRI may require a sub-millimeter in-plane resolution to avoid partial volume effects when assessing left atrial fibrosis. 2D ANGIE cannot provide sub-millimeter in-plane resolution due to restrictions posed by SNR. However, 3D ANGIE, with its higher SNR, may overcome this limitation and provide sub-millimeter in-plane resolution at the expense of coverage along the through plane direction or scan time.

Additionally, assessment of fibrosis for quantification of infarct tissue heterogeneity, an independent predictor of post-myocardial infarction mortality(120,121), requires high spatial resolution to detect subtle features of the peri-infarct zone and volumetric coverage to image the entire infarct and peri-infarct zone. 2D ANGIE provided restricted volumetric coverage due to its comparatively long acquisition time, a limitation which 3D ANGIE overcomes. Thus, 3D ANGIE may allow the quantitative assessment of subtle features in the peri-infarct zone and infarct tissue heterogeneity.

3D ANGIE uses readout segmentation and acquires four ECG-triggered readouts after the application of a single inversion pulse. Since the inversion time of the readout segment is also dependent on the R to R interval, heart rate variability may cause variability in the inversion time among different parts of k-space, which may lead to blurring or artifacts. By design, 3D ANGIE uses a variable density sampling scheme where the fully-sampled central k-space region, which primarily determines image contrast, is the first k-space partition acquired for each TI. This ensures the readout segments corresponding to the central k-space region are acquired close to each other, reducing the variability in inversion time. Furthermore, each readout segment is time

stamped and is binned according to its individual inversion time to minimize the variation of the inversion time within each bin. The average over the time stamps of the central fully-sampled portion of k-space defined the inversion time for each image.

Recently, there has been much debate concerning the use of saturation recovery versus inversion recovery for cardiac T1 mapping(122). Inversion recovery provides a wider dynamic range and higher SNR, factors which are important for CS-based reconstruction and high resolution imaging of thin structures. Additionally, inversion recovery provides robust T1 estimates even in the absence of a proton density image(122). Nevertheless, saturation recovery's higher accuracy and lower sensitivity to off-resonance, flip angle, heart rate variability and other factors may be advantageous for 3D T1 mapping(122,123). The current implementation of 3D ANGIE used inversion recovery; however, 3D ANGIE is not restricted to its use, and saturation recovery for 3D ANGIE T1 mapping will be investigated in the future.

3D ANGIE has some limitations that might affect its clinical applicability. First, 3D ANGIE uses a CS-PI based image reconstruction algorithm that currently requires an offline reconstruction. The iterative CS-PI image reconstruction takes a relatively long time to generate images compared to a FFT-based reconstruction. 3D ANGIE reconstruction was implemented in MATLAB (MathWorks, Natick, MA), and reconstruction of high resolution 3D ANGIE data took approximately 55 minutes on a workstation (18 x 2.5GHz Intel Xeon(R) CPU with 128GB RAM). Furthermore, the reconstruction parameters need an occasional adjustment to provide optimal results. Improving the speed to allow real-time image reconstruction is currently an active area of research(124).

Second, 3D ANGIE may have relatively long scan time compared to post-contrast washout dynamics, which could potentially confound ECV estimates. The scan time for post-contrast T1 mapping is primarily restricted by the effects of the dynamics of contrast agent. However, the post-contrast T1 values of the myocardium and blood (T1 range 250 to 700ms) are much lower than their respective native T1 values (T1 range 800 to 1700ms) due to the T1 shortening effects of gadolinium. Recently, Kellman et al showed that the optimal sample time points, as well as the optimal T1 mapping protocol, are different for post-contrast T1 mapping and native T1 mapping(122,123). The optimal post-contrast T1 mapping protocol employs fewer readouts and recovery heart beats per inversion compared to protocol for native T1 mapping(122). Thus, for post-contrast T1 mapping, 3D ANGIE would employ fewer readouts and recovery heart beats per inversion than with native T1 mapping. 3D ANGIE with an abbreviated protocol would reduce the scan time for post-contrast T1 mapping. Additionally, 3D ANGIE uses a variable density sampling scheme where the fully-sampled central k-space region -- which primarily determines image contrast -- is acquired at the beginning of the acquisition. This ensures the central fully sampled k-space region is acquired within a shorter interval of time, reducing the effects of variation due to contrast agent dynamics.

4.5 CONCLUSION

In summary, we developed 3D ANGIE, which can acquire high spatial resolution (~1.3x1.3x4mm^3) 3D cardiac T1 maps within a clinically-acceptable scan time. The design specifications were achieved by applying an adaptively-driven undersampling

strategy with an image reconstruction algorithm that combines compressed sensing with local low-rank sparsity, a partial Fourier acquisition, and parallel imaging (SENSE) with a navigator-gated and segmented inversion recovery Look-Locker sequence. Although 3D ANGIE is not currently ready for routine clinical use, its capability to perform high resolution 3D T1 mapping with high SNR opens up new avenues of potential applications, such as performing a quantitative assessment of thin structures like the RV wall, the left-atrial wall and subtle features of the peri-infarct zone.

Chapter 5

Conclusions & future directions

5.1 CONCLUSIONS

T1 mapping MRI has been used to non-invasively measure myocardial ECV, allowing the assessment of myocardial fibrosis; however, its application has until now been limited to imaging the LV due to spatiotemporal constraints imposed by most widely-used T1 mapping techniques. The primary innovation of this dissertation research was to develop high spatial resolution T1 mapping techniques capable of imaging thin myocardial structures such as the wall of the RV with a clinically-acceptable scan time. Furthermore, one of the two newly-developed T1 mapping techniques was applied in patients with pulmonary arterial hypertension (PAH) to assess RV fibrosis.

5.1.1 Development of 2D ANGIE

In Chapter 2, we presented ANGIE, a novel high-resolution 2D cardiac T1 mapping. We applied navigator-gating and readout segmentation in an inversion recovery Look-Locker sequence to overcome breath-hold constraints and achieve high spatial resolution. Since these features substantially increase imaging time, we used CS with matrix rank sparsity, in conjunction with SENSE PI, for acceleration. Additionally, we implemented an adaptive acquisition algorithm, which accounts for the interplay between navigator-gating and undersampling patterns that are well-suited for

compressed sensing, to further minimize scan time. ANGIE was validated in phantoms and in a comparison with MOLLI for T1 mapping of the LV in healthy volunteers. ANGIE provided high spatial resolution (1.2 x.1.2 x 4 mm^3) cardiac T1 mapping within clinically-acceptable scan time, enabling quantitative assessment of thin structures. We then performed ANGIE T1 mapping of the RV wall to demonstrate its improvement over MOLLI in healthy volunteers. To the best of our knowledge, this study was the first to report T1 mapping of the RV wall.

5.1.2 Application of 2D ANGIE in patients with PAH

In the study discussed in Chapter 3, we applied 2D ANGIE to assess RV fibrosis in PAH patients, using contrast-enhanced ECV measurements as a surrogate indicator of fibrosis. To the best of our knowledge, the study presented in Chapter 3 was the first to report the measurement of RV ECV in the context of PAH. In this study, pre- and post-contrast 2D ANGIE imaging provided high-resolution T1 mapping and ECV assessments for both ventricles. We found that the LV ECV measurements from 2D ANGIE and MOLLI were in close agreement. We demonstrated that the degree of the RV fibrosis, as measured by RV ECV, was higher in patients with PAH compared to patients with left-sided heart failure. Furthermore, the degree of the RV fibrosis measured by RV ECV in this cohort of patients increased with RV pressure overload and RV dilation, and it decreased with RV systolic function. From these observations, we concluded that quantitative tissue characterization of the RV using 2D ANGIE to measure the ECV may represent a valuable noninvasive marker of RV health in patients with PAH.

5.1.3 Development of 3D ANGIE

In the study discussed in Chapter 4, we extended 2D ANGIE to perform high-resolution 3D cardiac T1 mapping. To achieve high acceleration we used an image reconstruction algorithm that combines CS with local low-rank sparsity, a partial Fourier acquisition, and SENSE parallel imaging. Furthermore, an adaptively-driven undersampling strategy, enforcing probability density function-based criteria across time and a Poisson-disc based sampling criteria across space, was employed to improve image quality. 3D ANGIE provided high spatial resolution (~1.3x1.3x4mm^3) volumetric cardiac T1 mapping within a clinically acceptable scan time (~ 6.4 mins). Furthermore, we demonstrated that 3D ANGIE T1 maps provided good definition of the thin RV wall with high SNR in healthy volunteers. As a result, 3D ANGIE opens the prospect of performing quantitative assessment of the RV wall, and potentially the left-atrial walls and subtle features of the peri-infarct zone.

5.2 FUTURE DIRECTIONS

5.2.1 Applications

5.2.1.a RV ECV in patients with PAH

Our investigation of 2D ANGIE in patients with PAH for assessment of the RV fibrosis showed the importance of RV ECV measurement in patients with PAH. However, the study had a small sample size and did not include any patient follow-up. Nonetheless, its results are extremely promising. A similar future study in a larger patient population

with patient follow-up evaluating the prognostic value of RV ECV in PAH patients could be extremely valuable.

5.2.1.b RV ECV in other disease settings

Our study of the application of 2D ANGIE in patients with PAH demonstrated that 2D ANGIE could accurately estimate RV ECV. Assessing RV myocardial fibrosis could also be valuable in disorders such as arrhythmogenic right ventricular cardiomyopathy(51) and congenital heart disease. In the future, ANGIE RV ECV measurement of fibrosis might be applied in these patients.

5.2.1.c Peri-infarct zone in post-myocardial infarction patients

The peri-infarct zone represents tissue that is injured by ischemia but remains viable[28]. Recent studies have shown that infarct tissue heterogeneity increases the inducibility of sustained monomorphic ventricular tachycardia and is an independent predictor of post-myocardial infarction mortality[18, 29]. Quantitative assessment of the peri-infarct zone not only provides a tool to improve risk stratification of post-MI patients, but it may also provide important insight into the pathophysiological determinants of post-MI risk and could be applied to optimize management of post-MI patients[18]. However, quantitative assessment of subtle features of the peri-infarct zone and infarct tissue heterogeneity requires high spatial resolution and volumetric coverage. 3D ANGIE, which provides both, could potentially be useful for the quantitative assessment of the peri-infarct zone and infarct tissue heterogeneity in post-MI patients.

5.2.1.d Assessment of left atrial fibrosis in patients with atrial fibrillation

Quantitative assessment of left atrial myocardial fibrosis using T1 mapping MRI would be valuable in atrial fibrillation(52). However, the left atrial wall is extremely thin(119), with an average thickness of 1.89 ± 0.48 mm, ranging from 0.5-3.5mm. Left atrial T1 mapping may therefore require sub-millimeter in-plane resolution to avoid partial volume effects for performing quantitative assessment of fibrosis. 2D ANGIE cannot provide sub-millimeter in-plane resolution due to restrictions imposed by SNR. However, 3D ANGIE, which provides higher SNR, may overcome this limitation and allow for sub-millimeter in-plane resolution at the expenses of through-plane coverage or imaging time. 3D ANGIE may therefore be applied to quantitatively assess left atrial fibrosis in the patients with atrial fibrillation.

5.2.2 Technical developments

ANGIE provides high spatial resolution, volumetric cardiac T1 mapping within a clinically-acceptable scan time. This allows the quantitative assessment of myocardial fibrosis of thin structures such as the RV wall. However, for applications requiring even higher spatial resolution or whole heart coverage, 3D ANGIE's imaging time may not be clinically-acceptable. Even though ANGIE has opened up the application of T1 mapping to thin structures such as the RV wall, much room for technical improvement still exists.

5.2.2.a Non-Cartesian trajectories

The current implementation of ANGIE employed a Cartesian trajectory due to simplicity and the trajectory's robustness to artifacts. However, the Cartesian trajectory is not optimal for scan efficiency: non-Cartesian trajectories have higher data acquisition efficiencies, which ANGIE could utilize to reduce scan time. Furthermore, acquisitions

employing Cartesian trajectory cannot undersample along the frequency encode direction, and therefore they cannot exploit correlations in the frequency encoding direction. However, acquisitions with non-Cartesian trajectories can undersample along both in-plane dimensions, thus exploiting correlations along the in-plane dimensions. Undersampling along all in-plane dimensions would provide a higher acceleration rate while further reducing the scan time.

5.2.2.b Image reconstruction exploiting navigator rejected data

ANGIE acquisition employs navigator-gating to avoid respiratory motion artifacts. The image reconstruction algorithms proposed in this dissertation make use only of the data that has navigator recording within the respiratory acceptance window. Entire lines of data whose navigator recordings are outside the respiratory acceptance window are completely discarded. However, the data discarded due to navigator rejection has relevant information of the object of interest, which could be used in a constraint-based image reconstruction algorithm. An image reconstruction algorithm that uses both the navigator accepted data and also the navigator rejected data(125) may improve the reconstruction image quality and provide more acceleration.

These improvements would yield a higher acceleration factor, which could be applied to improve one or more of the following parameters, depending on the requirements of the particular application: decreased scan time, decreased readout acquisition window, increased spatial resolution, increased spatial coverage, and increased T1 estimation precision. For example the left atrium has an extremely thin(119) myocardial wall as well as shorter quiescent period. Therefore, an increase in

spatial resolution and reduction in readout acquisition time – factors allowed by higher acceleration -- might be crucial for T1 mapping of the left atrial wall.

Chapter 6

References

1. Mewton N, Liu CY, Croisille P, Bluemke D, Lima JA. Assessment of myocardial fibrosis with cardiovascular magnetic resonance. Journal of the American College of Cardiology 2011;57:891-903.
2. Simonneau G, Gatzoulis MA, Adatia I et al. Updated clinical classification of pulmonary hypertension. Journal of the American College of Cardiology 2013;62.
3. McLaughlin VV, Archer SL, Badesch DB et al. ACCF/AHA 2009 Expert Consensus Document on Pulmonary HypertensionA Report of the American College of Cardiology Foundation Task Force on Expert Consensus Documents and the American Heart Association Developed in Collaboration With the American College of Chest Physicians; American Thoracic Society, Inc.; and the Pulmonary Hypertension Association. Journal of the American College of Cardiology 2009;53:1573-1619.
4. Antkowiak PF. Manganese-enhanced MRI of pancreatic beta cells in mouse models of type 1 diabetes. Ann Arbor: University of Virginia, 2011:145.
5. McCurdy S, Baicu CF, Heymans S, Bradshaw AD. Cardiac extracellular matrix remodeling: fibrillar collagens and Secreted Protein Acidic and Rich in Cysteine (SPARC). Journal of molecular and cellular cardiology 2010;48:544-549.

6. Assomull RG, Prasad SK, Lyne J et al. Cardiovascular magnetic resonance, fibrosis, and prognosis in dilated cardiomyopathy. Journal of the American College of Cardiology 2006;48:1977-1985.

7. Bello D, Shah DJ, Farah GM et al. Gadolinium cardiovascular magnetic resonance predicts reversible myocardial dysfunction and remodeling in patients with heart failure undergoing β-blocker therapy. Circulation 2003;108:1945-1953.

8. Kwong RY, Chan AK, Brown KA et al. Impact of unrecognized myocardial scar detected by cardiac magnetic resonance imaging on event-free survival in patients presenting with signs or symptoms of coronary artery disease. Circulation 2006;113:2733-2743.

9. Conrad CH, Brooks WW, Hayes JA, Sen S, Robinson KG, Bing OH. Myocardial fibrosis and stiffness with hypertrophy and heart failure in the spontaneously hypertensive rat. Circulation 1995;91:161-170.

10. Iles L, Pfluger H, Phrommintikul A et al. Evaluation of diffuse myocardial fibrosis in heart failure with cardiac magnetic resonance contrast-enhanced T1 mapping. Journal of the American College of Cardiology 2008;52:1574-1580.

11. Schwarz F, Mall G, Zebe H et al. Quantitative morphologic findings of the myocardium in idiopathic dilated cardiomyopathy. The American journal of cardiology 1983;51:501-506.

12. Boudina S, Abel ED. Diabetic cardiomyopathy revisited. Circulation 2007;115:3213-3223.

13. Factor SM, Bhan R, Minase T, Wolinsky H, Sonnenblick EH. Hypertensive-diabetic cardiomyopathy in the rat: an experimental model of human disease. The American journal of pathology 1981;102:219.

14. Konduracka E, Gackowski A, Rostoff P, Galicka-Latala D, Frasik W, Piwowarska W. Diabetes-specific cardiomyopathy in type 1 diabetes mellitus: no evidence for its occurrence in the era of intensive insulin therapy. European heart journal 2007;28:2465-2471.

15. Tanaka M, Fujiwara H, Onodera T, Wu D, Hamashima Y, Kawai C. Quantitative analysis of myocardial fibrosis in normals, hypertensive hearts, and hypertrophic cardiomyopathy. British heart journal 1986;55:575-581.

16. Weber K, Brilla CG. Pathological hypertrophy and cardiac interstitium. Fibrosis and renin-angiotensin-aldosterone system. Circulation 1991;83:1849-1865.

17. Weber K, Janicki J, Shroff S, Pick R, Chen R, Bashey R. Collagen remodeling of the pressure-overloaded, hypertrophied nonhuman primate myocardium. Circulation Research 1988;62:757-765.

18. Díez J, Querejeta R, López B, González A, Larman M, Ubago JLM. Losartan-dependent regression of myocardial fibrosis is associated with reduction of left ventricular chamber stiffness in hypertensive patients. Circulation 2002;105:2512-2517.

19. López B, González A, Beaumont J, Querejeta R, Larman M, Díez J. Identification of a potential cardiac antifibrotic mechanism of torasemide in patients with chronic heart failure. Journal of the American College of Cardiology 2007;50:859-867.

20. López B, Querejeta R, González A, Sánchez E, Larman M, Díez J. Effects of loop diuretics on myocardial fibrosis and collagen type I turnover in chronic heart failure. Journal of the American College of Cardiology 2004;43:2028-2035.

21. Shah KB, Inoue Y, Mehra MR. Amyloidosis and the heart: a comprehensive review. Archives of internal medicine 2006;166:1805-1813.

22. Zarate YA, Hopkin RJ. Fabry's disease. The Lancet 2008;372:1427-1435.

23. Bohl S, Wassmuth R, Abdel-Aty H et al. Delayed enhancement cardiac magnetic resonance imaging reveals typical patterns of myocardial injury in patients with various forms of non-ischemic heart disease. The international journal of cardiovascular imaging 2008;24:597-607.

24. Karamitsos TD, Francis JM, Myerson S, Selvanayagam JB, Neubauer S. The role of cardiovascular magnetic resonance imaging in heart failure. Journal of the American College of Cardiology 2009;54:1407-1424.

25. Mahrholdt H, Wagner A, Judd RM, Sechtem U, Kim RJ. Delayed enhancement cardiovascular magnetic resonance assessment of non-ischaemic cardiomyopathies. European heart journal 2005;26:1461-1474.

26. Martos R, Baugh J, Ledwidge M et al. Diastolic heart failure Evidence of increased myocardial collagen turnover linked to diastolic dysfunction. Circulation 2007;115:888-895.

27. Jerosch-Herold M, Sheridan DC, Kushner JD et al. Cardiac magnetic resonance imaging of myocardial contrast uptake and blood flow in patients affected with idiopathic or familial dilated cardiomyopathy. American Journal of Physiology-Heart and Circulatory Physiology 2008;295:H1234-H1242.

28. Michalak DJ, Xu S, Lowery TJ et al. Relaxivity of gadolinium complexes detected by atomic magnetometry. Magnetic Resonance in Medicine 2011;66:603-606.

29. Kiely DG, Elliot CA, Sabroe I, Condliffe R. Pulmonary hypertension: diagnosis and management. BMJ: British Medical Journal 2013;346.

30. McLaughlin VV, McGoon MD. Pulmonary arterial hypertension. Circulation 2006;114:1417-1431.

31. Humbert M, Sitbon O, Chaouat A et al. Pulmonary arterial hypertension in France: results from a national registry. American journal of respiratory and critical care medicine 2006;173:1023-1030.

32. Sitbon O, Humbert M, Nunes H et al. Long-term intravenous epoprostenol infusion in primary pulmonary hypertensionPrognostic factors and survival. Journal of the American College of Cardiology 2002;40:780-788.

33. Badano LP, Ginghina C, Easaw J et al. Right ventricle in pulmonary arterial hypertension: haemodynamics, structural changes, imaging, and proposal of a study protocol aimed to assess remodelling and treatment effects. European Journal of Echocardiography 2010;11:27-37.

34. Swift AJ, Rajaram S, Campbell MJ et al. Prognostic Value of Cardiovascular Magnetic Resonance Imaging Measurements Corrected for Age and Gender in Idiopathic Pulmonary Arterial Hypertension. Circulation: Cardiovascular Imaging 2013:CIRCIMAGING. 113.000338.

35. van Wolferen SA, Marcus JT, Boonstra A et al. Prognostic value of right ventricular mass, volume, and function in idiopathic pulmonary arterial hypertension. European Heart Journal 2007;28:1250-1257.

36. Franco V. Right Ventricular Remodeling in Pulmonary Hypertension. Heart Failure Clinics 2012;8:403-412.

37. Noordegraaf AV, Galie N. The role of the right ventricle in pulmonary arterial hypertension. European Respiratory Review 2011;20:243-253.

38. Howard L. Prognostic factors in pulmonary arterial hypertension: assessing the course of the disease. European Respiratory Review 2011;20:236-242.

39. Flett AS, Hayward MP, Ashworth MT et al. Equilibrium contrast cardiovascular magnetic resonance for the measurement of diffuse myocardial fibrosis preliminary validation in humans. Circulation 2010;122:138-144.

40. Kellman P, Wilson JR, Xue H et al. Extracellular volume fraction mapping in the myocardium, part 2: initial clinical experience. J Cardiovasc Magn Reson 2012;14:64.

41. Sparrow P, Messroghli DR, Reid S, Ridgway JP, Bainbridge G, Sivananthan MU. Myocardial T1 mapping for detection of left ventricular myocardial fibrosis in chronic aortic regurgitation: pilot study. American Journal of Roentgenology 2006;187:W630-W635.

42. Klein C, Schmal TR, Nekolla SG, Schnackenburg B, Fleck E, Nagel E. Mechanism of late gadolinium enhancement in patients with acute myocardial infarction. Journal of cardiovascular magnetic resonance 2007;9:653-658.

43. Messroghli DR, Walters K, Plein S et al. Myocardial T1 mapping: application to patients with acute and chronic myocardial infarction. Magnetic Resonance in Medicine 2007;58:34-40.

44. Ugander M, Oki AJ, Hsu L-Y et al. Extracellular volume imaging by magnetic resonance imaging provides insights into overt and sub-clinical myocardial pathology. European heart journal 2012;33:1268-1278.

45. Banypersad SM, Sado DM, Flett AS et al. Quantification of Myocardial Extracellular Volume Fraction in Systemic AL Amyloidosis An Equilibrium Contrast Cardiovascular Magnetic Resonance Study. Circulation: Cardiovascular Imaging 2013;6:34-39.

46. Brooks J, Kramer CM, Salerno M. Markedly increased volume of distribution of gadolinium in cardiac amyloidosis demonstrated by T1 mapping. Journal of Magnetic Resonance Imaging 2013.

47. Messroghli DR, Radjenovic A, Kozerke S, Higgins DM, Sivananthan MU, Ridgway JP. Modified Look-Locker inversion recovery (MOLLI) for high-resolution T1 mapping of the heart. Magnetic Resonance in Medicine 2004;52:141-146.

48. Piechnik S, Ferreira V, Dall'Armellina E et al. Shortened Modified Look-Locker Inversion recovery (ShMOLLI) for clinical myocardial T1-mapping at 1.5 and 3 T within a 9 heartbeat breathhold. Journal of Cardiovascular Magnetic Resonance 2010;12:69.

49. Freed BH, Gomberg-Maitland M, Chandra S et al. Late gadolinium enhancement cardiovascular magnetic resonance predicts clinical worsening in patients with pulmonary hypertension. Journal of Cardiovascular Magnetic Resonance 2012;14.

50. Shehata ML, Lossnitzer D, Skrok J et al. Myocardial delayed enhancement in pulmonary hypertension: pulmonary hemodynamics, right ventricular function, and remodeling. American Journal of Roentgenology 2011;196:87-94.

51. Tandri H, Saranathan M, Rodriguez ER et al. Noninvasive detection of myocardial fibrosis in arrhythmogenic right ventricular cardiomyopathy using delayed-enhancement magnetic resonance imaging. Journal of the American College of Cardiology 2005;45:98-103.

52. Beinart R, Khurram IM, Liu S et al. Cardiac Magnetic Resonance T1 Mapping of Left Atrial Myocardium. Heart Rhythm 2013.

53. van de Veerdonk MC, Kind T, Marcus JT et al. Progressive right ventricular dysfunction in patients with pulmonary arterial hypertension responding to therapy. Journal of the American College of Cardiology 2011;58:2511-2519.

54. Mehta BB, Chen X, Bilchick KC, Salerno M, Epstein FH. Accelerated and navigator-gated look-locker imaging for cardiac t1 estimation (ANGIE): Development and application to T1 mapping of the right ventricle. Magnetic Resonance in Medicine 2014.

55. Candès EJ, Romberg J, Tao T. Robust uncertainty principles: Exact signal reconstruction from highly incomplete frequency information. Information Theory, IEEE Transactions on 2006;52:489-509.

56. Donoho DL. Compressed sensing. Information Theory, IEEE Transactions on 2006;52:1289-1306.

57. Lustig M, Donoho D, Pauly JM. Sparse MRI: The application of compressed sensing for rapid MR imaging. Magnetic Resonance in Medicine 2007;58:1182-1195.

58. Pruessmann KP, Weiger M, Scheidegger MB, Boesiger P. SENSE: sensitivity encoding for fast MRI. Magnetic resonance in medicine 1999;42:952-962.

59. Barral J, Nishimura D. Compressed sensing for motion artifact reduction. Proceedings of the 17th Annual Meeting of ISMRM, Honolulu, Hawaii, 2009:4593.

60. Donoho DL, Elad M. Optimally sparse representation in general (nonorthogonal) dictionaries via ℓ1 minimization. Proceedings of the National Academy of Sciences 2003;100:2197-2202.

61. Jung H, Ye JC. Motion estimated and compensated compressed sensing dynamic magnetic resonance imaging: What we can learn from video compression techniques. International Journal of Imaging Systems and Technology 2010;20:81-98.

62. Karlsen OT, Verhagen R, Bovee WM. Parameter estimation from Rician-distributed data sets using a maximum likelihood estimator: application to T1 and perfusion measurements. Magnetic Resonance in Medicine 1999;41:614-623.

63. Zhang Y, Yeung HN, O'Donnell M, Carson PL. Determination of sample time for T1 measurement. Journal of Magnetic Resonance Imaging 1998;8:675-681.

64. Look DC, Locker DR. Time saving in measurement of NMR and EPR relaxation times. Review of Scientific Instruments 2003;41:250-251.

65. Taylor AM, Jhooti P, Wiesmann F, Keegan J, Firmin DN, Pennell DJ. MR navigator-echo monitoring of temporal changes in diaphragm position: Implications for MR coronary angiography. Journal of Magnetic Resonance Imaging 1997;7:629-636.

66. Le Roux P. Simplified model and stabilization of SSFP sequences. Journal of Magnetic Resonance 2003;163:23-37.

67. Lingala SG, Hu Y, DiBella E, Jacob M. Accelerated dynamic MRI exploiting sparsity and low-rank structure: k-t SLR. Medical Imaging, IEEE Transactions on 2011;30:1042-1054.

68. Walsh DO, Gmitro AF, Marcellin MW. Adaptive reconstruction of phased array MR imagery. Magnetic Resonance in Medicine 2000;43:682-690.

69. Kellman P, Arai AE, McVeigh ER, Aletras AH. Phase-sensitive inversion recovery for detecting myocardial infarction using gadolinium-delayed hyperenhancement. Magnetic Resonance in Medicine 2002;47:372-383.

70. Wang Z, Bovik AC, Sheikh HR, Simoncelli EP. Image quality assessment: from error visibility to structural similarity. Image Processing, IEEE Transactions on 2004;13:600-612.

71. Kato H, Kuroda M, Yoshimura K et al. Composition of MRI phantom equivalent to human tissues. Medical physics 2005;32:3199-3208.

72. Mitchell MD, Kundel HL, Axel L, Joseph PM. Agarose as a tissue equivalent phantom material for NMR imaging. Magnetic resonance imaging 1986;4:263-266.

73. Mertens LL, Friedberg MK. Imaging the right ventricle—current state of the art. Nature Reviews Cardiology 2010;7:551-563.

74. Grosse-Wortmann L, Macgowan CK, Vidarsson L, Yoo S-J. Late gadolinium enhancement of the right ventricular myocardium: is it really different from the left? Journal of cardiovascular magnetic resonance 2008;10:1-9.

75. Marziliano P, Dufaux F, Winkler S, Ebrahimi T. Perceptual blur and ringing metrics: application to JPEG2000. Signal Processing: Image Communication 2004;19:163-172.

76. McGraw KO, Wong SP. Forming inferences about some intraclass correlation coefficients. Psychological methods 1996;1:30.

77. Bland JM, Altman D. Statistical methods for assessing agreement between two methods of clinical measurement. The lancet 1986;327:307-310.

78. Barth M, Moser E. Proton NMR relaxation times of human blood samples at 1.5 T and implications for functional MRI. CELLULAR AND MOLECULAR BIOLOGY-PARIS-WEGMANN- 1997;43:783-792.

79. Flacke SJ, Fischer SE, Lorenz CH. Measurement of the Gadopentetate Dimeglumine Partition Coefficient in Human Myocardium in Vivo: Normal Distribution and Elevation in Acute and Chronic Infarction 1. Radiology 2001;218:703-710.

80. Spees WM, Yablonskiy DA, Oswood MC, Ackerman JJ. Water proton MR properties of human blood at 1.5 Tesla: Magnetic susceptibility, T1, T2, T* 2, and non-Lorentzian signal behavior. Magnetic resonance in medicine 2001;45:533-542.

81. Mehta BB, Chen X, Salerno M, Kramer CM, Epstein FH. Accelerated and navigator-gated look-locker imaging for cardiac T1 Estimation (ANGIE) with reduced motion artifact. Journal of Cardiovascular Magnetic Resonance 2012;14:1-2.

82. Chow K, Flewitt JA, Green JD, Pagano JJ, Friedrich MG, Thompson RB. Saturation recovery single-shot acquisition (SASHA) for myocardial T1 mapping. Magnetic Resonance in Medicine 2014;71:2082-2095.

83. Fitts M, Breton E, Kholmovski EG et al. Arrhythmia insensitive rapid cardiac T1 mapping pulse sequence. Magnetic Resonance in Medicine 2013;70:1274-1282.

84. Song T, Stainsby JA, Ho VB, Hood MN, Slavin GS. Flexible cardiac T1 mapping using a modified Look-Locker acquisition with saturation recovery. Magnetic Resonance in Medicine 2012;67:622-627.

85. Desai MY, Gupta S, Bomma C et al. The apparent inversion time for optimal delayed enhancement magnetic resonance imaging differs between the right and left ventricles. Journal of Cardiovascular Magnetic Resonance 2005;7:475-479.

86. Kim RJ, Shah DJ, Judd RM. How We Perform Delayed Enhancement Imaging. Journal of cardiovascular magnetic resonance 2003;5:505-514.

87. Vonk-Noordegraaf A, Haddad F, Chin KM et al. Right Heart Adaptation to Pulmonary Arterial HypertensionPhysiology and Pathobiology. Journal of the American College of Cardiology 2013;62.

88. Schiebler ML, Bhalla S, Runo J et al. Magnetic Resonance and Computed Tomography Imaging of the Structural and Functional Changes of Pulmonary Arterial Hypertension. Journal of thoracic imaging 2013;28:178-195.

89. Mehta BB, Chen X, Bilchick KC, Salerno M, Epstein FH. Accelerated and Navigator-Gated Look-Locker Imaging for Cardiac T1 Estimation (ANGIE): Development and Application to T1 mapping of the Right Ventricle . Magnetic Resonance in Medicine 2014.

90. Kellman P, Arai AE, Xue H. T1 and extracellular volume mapping in the heart: estimation of error maps and the influence of noise on precision. 2013.

91. Kellman P, Wilson JR, Xue H, Ugander M, Arai AE. Extracellular volume fraction mapping in the myocardium, part 1: evaluation of an automated method. J Cardiovasc Magn Reson 2012;14:63.

92. Kellman P, Arai AE, McVeigh ER, Aletras AH. Phase-sensitive inversion recovery for detecting myocardial infarction using gadolinium-delayed hyperenhancement†. Magnetic Resonance in Medicine 2002;47:372-383.

93. Deichmann R, Haase A. Quantification of T 1 values by SNAPSHOT-FLASH NMR imaging. Journal of Magnetic Resonance (1969) 1992;96:608-612.

94. Kehr E, Sono M, Chugh SS, Jerosch-Herold M. Gadolinium-enhanced magnetic resonance imaging for detection and quantification of fibrosis in human myocardium in vitro. The international journal of cardiovascular imaging 2008;24:61-68.

95. Salerno M, Janardhanan R, Jiji RS et al. Comparison of methods for determining the partition coefficient of gadolinium in the myocardium using T1 mapping. Journal of Magnetic Resonance Imaging 2012.

96. Rudski LG, Lai WW, Afilalo J et al. Guidelines for the Echocardiographic Assessment of the Right Heart in Adults: A Report from the American Society of

Echocardiography: Endorsed by the European Association of Echocardiography, a registered branch of the European Society of Cardiology, and the Canadian Society of Echocardiography. Journal of the American Society of Echocardiography 2010;23:685-713.

97. Yock PG, Popp RL. Noninvasive estimation of right ventricular systolic pressure by Doppler ultrasound in patients with tricuspid regurgitation. Circulation 1984;70:657-662.

98. Dabir D, Child N, Kalra A et al. Reference values for healthy human myocardium using a T1 mapping methodology: results from the International T1 Multicenter cardiovascular magnetic resonance study. Journal of Cardiovascular Magnetic Resonance 2014;16:69.

99. Bevington PR, Robinson DK. Data reduction and error analysis. McGraw–Hill, New York 2003.

100. Blyth KG, Groenning BA, Martin TN et al. Contrast enhanced-cardiovascular magnetic resonance imaging in patients with pulmonary hypertension. European heart journal 2005;26:1993-1999.

101. McCann GP, Gan C, Beek AM, Niessen HW, Noordegraaf AV, van Rossum AC. Extent of MRI delayed enhancement of myocardial mass is related to right ventricular dysfunction in pulmonary artery hypertension. American Journal of Roentgenology 2007;188:349-355.

102. Sanz J, Dellegrottaglie S, Kariisa M et al. Prevalence and Correlates of Septal Delayed Contrast Enhancement in Patients With Pulmonary Hypertension< sup>†</sup>. The American journal of cardiology 2007;100:731-735.

103. Moon JC, Messroghli DR, Kellman P et al. Myocardial T1 mapping and extracellular volume quantification: a Society for Cardiovascular Magnetic Resonance (SCMR) and CMR Working Group of the European Society of Cardiology consensus statement. J Cardiovasc Magn Reson 2013;15:92.

104. García-Álvarez A, García-Lunar I, Pereda D et al. Association of Myocardial T1-Mapping CMR with Hemodynamics and Right Ventricular Performance in Pulmonary Hypertension. JACC: Cardiovascular Imaging 2014.

105. Garcia-Lunar I, Pazos P, Pozo E et al. Myocardial fibrosis with T1 mapping and right ventricular performance in pulmonary hypertension. Journal of Cardiovascular Magnetic Resonance 2013;15:E102.

106. Pozo E, Garcia-Lunar I, Pazos P et al. Increased septal extracellular volume estimated by T1-mapping predicts right ventricular performance in pulmonary hypertension. Journal of the American College of Cardiology 2013;61.

107. Wong TC, Piehler K, Meier CG et al. Association between extracellular matrix expansion quantified by cardiovascular magnetic resonance and short term mortality. Circulation 2012:CIRCULATIONAHA. 111.089409.

108. Sado DM, White SK, Piechnik SK et al. Identification and assessment of Anderson-Fabry disease by cardiovascular magnetic resonance noncontrast myocardial T1 mapping. Circulation: Cardiovascular Imaging 2013;6:392-398.

109. Pedersen SF, Thrysøe SA, Robich MP et al. Assessment of intramyocardial hemorrhage by T1-weighted cardiovascular magnetic resonance in reperfused acute myocardial infarction. Journal of Cardiovascular Magnetic Resonance 2012;14:1-8.

110. Miller CA, Naish JH, Bishop P et al. Comprehensive validation of cardiovascular magnetic resonance techniques for the assessment of myocardial extracellular volume. Circulation: Cardiovascular Imaging 2013;6:373-383.

111. Clique H, Cheng HLM, Marie PY, Felblinger J, Beaumont M. 3D myocardial T1 mapping at 3T using variable flip angle method: Pilot study. Magnetic resonance in medicine 2014;71:823-829.

112. Weingärtner S, Akçakaya M, Roujol S et al. Free-breathing post-contrast three-dimensional T1 mapping: Volumetric assessment of myocardial T1 values. Magnetic Resonance in Medicine 2014.

113. Chen X, Salerno M, Yang Y, Epstein FH. Motion-compensated compressed sensing for dynamic contrast-enhanced MRI using regional spatiotemporal sparsity and region tracking: Block low-rank sparsity with motion-guidance (BLOSM). Magnetic Resonance in Medicine 2013.

114. Trzasko J, Manduca A, Borisch E. Local versus global low-rank promotion in dynamic MRI series reconstruction. Proc Int Symp Magn Reson Med, 2011:4371.

115. Zhang T, Alley M, Lustig M, Li X, Pauly J, Vasanawala S. Fast 3D DCE-MRI with sparsity and low-rank enhanced SPIRiT (SLR-SPIRiT). Proc 21st Annual Meeting ISMRM, Salt Lake City, 2013:2624.

116. Mehta BB, Chen X, Bilchick KC, Salerno M, Epstein FH. Accelerated and navigator-gated look-locker imaging for cardiac T1 estimation (ANGIE): Development and application to T1 mapping of the right ventricle. Magnetic Resonance in Medicine 2015;73:150-160.

117. Lustig M, Alley M, Vasanawala S, Donoho D, Pauly J. L1 SPIR-iT: autocalibrating parallel imaging compressed sensing. Proc Intl Soc Mag Reson Med, 2009:379.

118. Usman M, Batchelor PG. Optimized Sampling Patterns for Practical Compressed MRI. SAMPTA'09, International Conference on Sampling Theory and Applications, 2009.

119. Beinart R, Abbara S, Blum A et al. Left atrial wall thickness variability measured by CT scans in patients undergoing pulmonary vein isolation. Journal of cardiovascular electrophysiology 2011;22:1232-1236.

120. Schmidt A, Azevedo CF, Cheng A et al. Infarct tissue heterogeneity by magnetic resonance imaging identifies enhanced cardiac arrhythmia susceptibility in patients with left ventricular dysfunction. Circulation 2007;115:2006-2014.

121. Yan AT, Shayne AJ, Brown KA et al. Characterization of the peri-infarct zone by contrast-enhanced cardiac magnetic resonance imaging is a powerful predictor of post–myocardial infarction mortality. Circulation 2006;114:32-39.

122. Kellman P, Hansen MS. T1-mapping in the heart: accuracy and precision. J Cardiovasc Magn Reson 2014;16.

123. Kellman P, Xue H, Chow K, Spottiswoode BS, Arai AE, Thompson RB. Optimized saturation recovery protocols for T1-mapping in the heart: influence of sampling strategies on precision. Journal of Cardiovascular Magnetic Resonance 2014;16:55.

124. Smith DS, Gore JC, Yankeelov TE, Welch EB. Real-time compressive sensing MRI reconstruction using GPU computing and split Bregman methods. International journal of biomedical imaging 2012;2012.

125. Usman M, Atkinson D, Odille F et al. Motion corrected compressed sensing for free-breathing dynamic cardiac MRI. Magnetic Resonance in Medicine 2013;70:504-516.